DIPLOMARBEIT

Diagrammatic approach to the optical conductivity in strongly correlated systems

zur Erlangung des akademischen Grades

Diplom-Ingenieur

im Rahmen des Studiums

Technische Physik

eingereicht von

Paul Worm
Matrikelnummer 01431312

Ausgeführt am
Institut für Festkörperphysik
der Fakultät für Physik
der Technischen Universität Wien

unter der Anleitung von
Univ.Ass. Dr. Anna Kauch,
Projektass. Dipl.-Ing. Clemens Watzenböck
und
Univ.Prof. Dr. Karsten Held

Wien, December 16, 2019

Paul Worm	Karsten Held

Abstract

The interaction of a solid with an electromagnetic field, or from a quantum point of view with photons, gives rise to new quasi-particles coined polaritons. For semi-conductors the exciton is the generic polariton, whose characteristics are well investigated. Dominant polaritons in strongly correlated system however, might be of a very different nature. Using parquet equations, which are not biased in favour or against certain channels or physics, new polaritons in Hubbard-like systems can be observed: π-tons. These π-tons manifest themselves in vertex corrections to the optical conductivity that are dominated by the contributions in the particle-hole transversal channel. They consist of two particle-hole pairs glued together by anitferromagnetic or charge density wave fluctuations.

In order to investigate the π-ton contributions in detail and without the necessity of a cumbersome numeric analytic continuation we develop a simplified real frequency formalism that approximates the vertex function $F_{kk'q}$. That is, we include all two particle scattering processes by an effective vertex F_q which only depends on one frequency ω and one momentum vector $\mathbf{q}$. The formalism requires the self energy and effective vertex as input, hence granting us control over the diagrams included and thus physical processes investigated.

Motivated by the picture of π-tons feeding upon antiferromagnetic and charge density wave fluctuations we employ a particle-hole transversal ladder in the random phase approximation (RPA) as effective vertex. Indeed we are able to show that this RPA-ladder correctly reproduces the low-frequency behaviour, which comprises the majority of the vertex corrections to the optical conductivity. Hence the core features of these π-tons can be reproduced by an RPA-ladder in the particle-hole transversal channel, which supports our current picture of these novel quasi particles.

Furthermore we show that the low-frequency vertex corrections can be understood in terms of an additional broadening of the Drude peak in the optical conductivity, which exhibits a characteristic temperature dependence. This means that scattering rate determined from the optics deviates characteristically from the one-particle scattering rate as determined from the self-energy or from angular resoled photoemission spectroscopy (ARPES). With this we provide a first link to verifying π-tons experimentally.

Kurzfassung

Durch die Wechselwirkung eines Festkörpers mit einem elektromagnetischen Feld, oder aus quantenmechanischer Sicht mit Photonen, entstehen neue Quasiteilchen, genannt Polaritonen. Für Halbleiter ist das Exciton das generische Polariton, dessen Eigenschaften genau untersucht sind. Die dominanten Polaritonen in stark korrelierten Systemen könnten jedoch ganz anderer Natur sein. Durch Lösen der Parkett-Gleichungen, die weder spezielle Kanäle noch Physik bevorzugen, konnten in Hubbard-ähnlichen Systemen neue Polaritonen beobachtet werden: π-tonen. Diese π-tonen manifestieren sich in den Vertexkorrekturen zur optischen Leitfähigkeit, dievon Beiträgen im Teilchen-Loch transveralen Kanal dominiert werden. Sie bestehen aus zwei Teilchen-Loch Paaren, die durch antiferromagnetische Spinfluktuationen oder Fluktuationen von Ladungsdichtewellen zusammengehalten werden.

Um die Beiträge der π-tonen detailliert und ohne die Notwendigkeit einer mühsamen numerischen analytischen Fortsetzung zu untersuchen, leiten wir einen vereinfachten Formalismus in reellen Frequenzen her, der die Vertex-Funktion $F_{kk'q}$ approximiert. In unserer Näherung beschreiben wir alle Zweiteilchenstreuprozesse durch eine effektive Vertex-Funktion F_q, die nur von einer Frequenz ω und einem Impulsvektor $\mathbf{q}$ abhängt. Der Formalismus benötigt die Selbstenergie und den effektiven Vertex als Input, über die wir die enthaltenen Diagramme und damit die untersuchten physikalischen Prozesse kontrollieren können.

Motiviert durch das Bild, dass π-tonen durch antiferromagnetische Spinfluktuationen und Fluktuationen von Ladungsdichtewellen erzeugt werden, verwenden wir eine Teilchen-Loch transversale Leiter in der Random-Phase-Approximation (RPA) als effektiven Vertex. Damit können wir zeigen, dass diese RPA-Leiter das Niederfrequenzverhalten korrekt beschreibt, das den Großteil der Vertexkorrekturen der optischen Leitfähigkeit beinhaltet. Dadurch können die Kernmerkmale dieser π-tonen durch eine RPA-Leiter im Teilchen-Loch transversalen Kanal reproduziert werden, was unser aktuelles Bild dieser neuen Quasiteilchen bekräftigt.

Weiters zeigen wir, dass die niederfrequenten Vertexkorrekturen durch eine zusätzliche Verbreiterung des Drude-Peaks in der optischen Leitfähigkeit verstanden werden können, der eine charakteristische Temperaturabhängigkeit aufweist. Dies bedeutet, dass die, über optische Wege ermittelte Streurate charakteristisch von der Einteilchen-Streurate abweicht, die über die Selbstenergie oder durch winkelaufgelöste Photoemissionsspektroskopie (ARPES) bestimmt werden kann. Damit können wir einen ersten Versuch zum experimentellen Nachweis von π-tonen vorschlagen.

Contents

1. Introduction and motivation

Condensed matter physics is an exceptionally rich field which includes the study of remarkable phenomena such as superconductivity, quantum criticality or electronic correlations in general[1]. It contains not only fundamental research though, but also applications requiring materials with exceptional properties. Theoretical condensed matter physics develops methods and tools needed to describe the properties of (ideally) any solid imaginable and also uses those tools in combination with physical intuition to describe properties and features of novel materials. However, no all-in-one method suitable for every purpose exists as of yet - not even for crystals, i.e. solids that are constructed via repeating a unit-cell, which is one major focus of modern condensed matter physics. In the case of weak electronic correlations the Density Functional Theory (DFT) approach of Walter Kohn and Pierre Hohenberg[2] proved to be a powerful method[3]. This changes in the presence of strong electronic correlations, as DFT is no longer applicable. To cope with such systems different methods have been developed, one being the Dynamical Mean Field Theory (DMFT)[4,5]. Even tough DMFT handles local correlations non-perturbativly, it neglects all non-local correlations. One way to address this issue are so called diagrammatic extensions of DMFT[6]. In this thesis we will only be dealing with the Dynamical Vertex Approximation (DΓA) developed by Alessandro Toschi, Andrey Katanin and Karsten Held[7].
The methods above can be used not only to describe structural features like bands or density of states (DOS), but also to predict the response of a system to external perturbations. This thesis focuses on the optical conductivity (OC), the response to an external alternating electrical field. We describe the electronic system via non-relativistic many body quantum field theory (MB-QFT) and introduce coupling to the external field classically using the Perierl's substitution[8].
The arguably simplest interaction of light with any material is the photoelectric effect[9], where photons simply excite an electron over the band gap, thus creating an electron-hole pair. However, the interaction may also involve more complex bosonic polarized quasi-particles coined polaritons. One of these polaritons is the exciton[10,11], an excited electron-hole pair bound by the Coulomb interaction. Characteristics and features of excitons[10,11] have been studied to great extend and it is believed to be the dominant polariton contributing to the OC in semiconductors. A recent study[12] employs the parquet equations to investigate the OC in strongly correlated systems (like the Hubbard or Falikov-Kimball model). The observation of dominant vertex-corrections from the particle-hole transversal $\overline{ph}$ channel motivates new polaritons. Moreover, almost all of the corrections are from **k**-points in the vicinity of $(\pi, \pi, ...)$, thus the name π-ton has been proposed. A visual representation using Feynman diagrams is displayed in Fig. 1.1.
However, parquet calculations suffer from two major drawbacks: first the calculations (like most of such diagrammatic approaches) are performed using imaginary (Matsubara) frequencies, which evokes the need for a numerical analytic continuation - an ill posed problem for noisy data. The maximum entropy (MaxEnt) method tends to smear out features in the best case and create additional peaks in the worst case[13,14]. Second, parquet equations generate all possible diagrams with an approximation to the fully irreducible vertex Λ as a building block. With this being the major merit of the method, a later association of features with certain classes of diagrams is often not possible.
In order to address the issues mentioned above we develop in this thesis a simplified real time formulation for the $\overline{ph}$-ladder diagrams contributing to the OC and also a code to perform the necessary calculation. This code is capable of handling any $\overline{ph}$-channel one-frequency vertex as input granting us control over which diagrams and thus physical processes shall be investigated. Additionally via using a real frequency formalism, numeric analytic continuation is naturally avoided.

This thesis is organised as follows: In Chapter 2 we first give a short introduction to the used model Hamiltonian and a review of MB-QFT. The last section will also contain information regarding methods for analytic continuation. Those methods will be used in Chapter 3 to derive a simplified real frequency expression for the OC from linear response theory. In that context we will also briefly talk about the f-sum rule and Drude conductivity. Moving on, Chapter 4 introduces the used effective vertices and Green's functions. Results of our calculations and comparison to parquet DΓA[12] results are presented in Chapter 5. Concluding remarks are given at the end in Chapter 6.

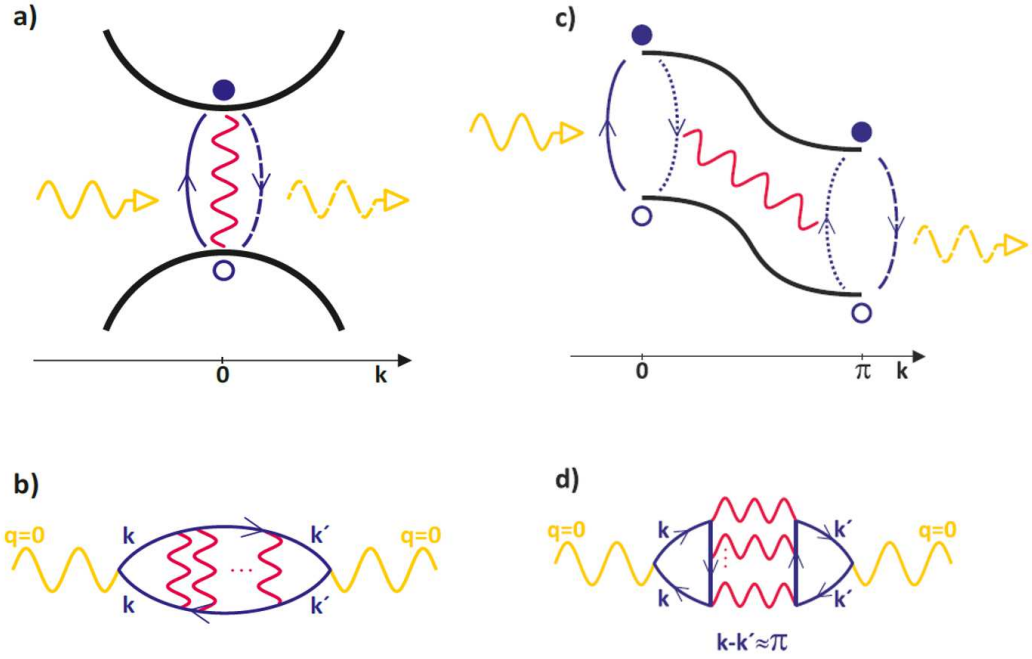

Figure 1.1.: Sketch of the physical processes (top) and Feynman diagrams (bottom) behind an exciton (left) and a π-ton (right). The yellow wiggled line symbolizes the incoming (and outgoing) photon which creates an electron-hole pair denoted by open and filled circles, respectively. The Coulomb interaction between the particles is symbolized by a red wiggled line; dashed line indicates the recombination of the particle and hole; the dotted line denotes the creation of a second particle-hole pair (right); black lines represents the underlying bandstructure (top panels). [Taken from Ref. 12]

2. Models and methods

The main approach of this work to study the optical conductivity is based on the Green's function (GF) method and the associated Feynman diagrams. Feynman diagrams are of particular use, as they allow one to better visualize the physical processes behind observations. As basis we will first talk about the solid state Hamiltonian in general and then move on to an approximation of it coined the Hubbard model. Then we introduce the one-particle Green's functions, from which the spectral function as well as all other one-particle observables can be calculated. A natural extension to two-particle observables are the two-particle Green's functions, which are connected to the physical response of the system to an external perturbation. Since we use a real frequency formulation to avoid the numerical analytic continuation, a technique to perform such transformations using pen, paper and contour integrals is discussed at the end.

2.1. Solid state Hamiltonian

In solid state physics one usually considers a system of ionic cores, which are aligned in a periodic crystal structure surrounded by electrons. For all practical purposes the whole system can be described by a Hamiltonian consisting of three terms[15]:

$$\mathcal{H}_s = \mathcal{H}_e + \mathcal{H}_i + \mathcal{H}_{ei}. \tag{2.1}$$

$\mathcal{H}_s$ is the full solid-state Hamiltonian, $\mathcal{H}_e$ is the contribution stemming from the electrons, $\mathcal{H}_i$ is the contribution from the ionic cores and $\mathcal{H}_{ei}$ is the interaction between the cores and the electrons. Even tough each of the contributions can be written down exactly, it is impossible to compute the true many-body wave-function of the system due to the sheer number of particles involved, usually of the order of 10^{23}.
The main problem which prohibits an exact solution are two-particle interactions [electron-electron (e-e) and electron-ionic core (e-ion)]. While e-ion interactions can, for many systems, be treated employing the Born-Oppenheimer approximation[16], a similar approach is not applicable for e-e correlations. To circumvent this problem two major approaches have been developed[17]: One can either use a so-called model Hamiltonian instead of Eq. (2.1) which greatly simplifies the Hamiltonian itself and then try to solve it, or one can use direct approximations to one of the terms in Eq. (2.1), which usually means approximations for the electronic correlations. DFT[2] is the most notable and widely employed technique within the second approach, but will not be discussed further in this theses. Instead, we focus on a model Hamiltonian, namely the Hubbard model.

2.2. Hubbard model

One of the simplest models to describe the competition between kinetic energy and electronic correlations is the Hubbard-model[18]:

$$\mathcal{H}_1 = \sum_{ij\sigma} t_{ij} c^\dagger_{j\sigma} c_{i\sigma} + \sum_i U \hat{n}_{i\uparrow} \hat{n}_{i\downarrow}. \tag{2.2}$$

Here U denotes the on-site Coulomb interaction and t_{ij} are hopping amplitudes from site i to site j. $c_{i\sigma}$ ($c^\dagger_{i\sigma}$) denote the fermionic annihilation(creation) operators at site i with spin σ. The Hubbard model is of particular interest as it is believed to be a sufficient model to describe high temperature superconductivity in cuprates and nicklates[19,20]. However, the study of the exact mechanism behind this form of high temperature superconductivity is still an active field of research[21] and not yet fully understood.

2.3. Many body quantum field theory

We use a Green's function approach to MB-QFT and employ Feynman diagrams to describe types of interactions effectively. At this point we want to emphasise that even tough Feynman diagrams emerge from a perturbation series it is possible to capture certain classes of diagrams non-perturbativly. We will mostly do this by constructing so called ladder-diagrams [one well known example would be the random-phase-approximation (RPA)], while a more sophisticated approach to do so would be DΓA[7].

2.3.1. Green's function methods

Since monitoring the movement and behaviour of roughly 10^{23} electrons in the system is a hopeless task and even if we could manage to do so, it would be equally difficult to extract useful information. Hence another approach to problem needs to be developed. This gives rise to the idea to instead monitor a single electron that is added to the system at time t and removed again at a later time t'. The object which does that is coined the causal (or sometimes time-ordered) Green's function:

$$G_C(\mathbf{r}', t'; \mathbf{r}, t) = -i\Theta(t' - t)\langle \psi(\mathbf{r}', t')\psi^\dagger(\mathbf{r}, t)\rangle \pm i\Theta(t - t')\langle \psi^\dagger(\mathbf{r}, t)\psi(\mathbf{r}', t')\rangle. \tag{2.3}$$

Where $\psi^\dagger(\mathbf{r}, t)$ ($\psi(\mathbf{r}, t)$) are field operators that create (annihilate) a particle at position $\mathbf{r}$ and time t. The plus (minus) corresponds to fermions (bosons) and is due to the required symmetry of the wave-function. Using the Wick time ordering operator $\mathcal{T}$ this can be written in a compact notation,

$$G_C(\mathbf{r}', t'; \mathbf{r}, t) = -i\langle \mathcal{T}\psi(\mathbf{r}', t')\psi^\dagger(\mathbf{r}, t)\rangle. \tag{2.4}$$

Here, the average $\langle\rangle$ denotes the thermal average over a grand-canonical ensemble

$$\langle X\rangle = \frac{1}{Z} \cdot Tr[e^{-\beta\cdot\mathcal{H}} X], \tag{2.5}$$

where Z is the grand-canonical partition sum

$$Z = Tr[e^{-\beta\cdot\mathcal{H}}], \tag{2.6}$$

β denotes the inverse temperature $\beta = \frac{1}{Tk_B}$ $\mathcal{H}$ is the Hamiltonian of the system and $Tr[]$ denotes the standard trace. When working on a lattice instead of a continuous space it is convenient to write

Eq. (2.4) not in terms of field operators but instead of creation and annihilation operators for lattice sites or orbitals i, j

$$G_C(j, t'; i, t) = -i\langle \mathcal{T} c(j, t') c^\dagger(i, t) \rangle. \tag{2.7}$$

The physical interpretation of Eq. (2.7) is as follows: in the case of $t' > t$ $G_C(j, t'; i, t)$ describes the amplitude of finding a particle at site j and time t' if a particle has been inserted at site i and time t . For $t' < t$ it describes the amplitude of finding a hole at site i and time t if a hole has been inserted at site j and time t'. In this context the insertion of a hole is equivalent to the removal of a particle. In the following chapter the connection to the spectral function will be discussed, which is one major reason why one-particle Green's functions are of interest.

2.3.2. Matsubara formalism

When working at finite temperature it is convenient not to work in real but imaginary time instead ,$t \to -i\tau$,[22]. This transformation is described by a Wick-rotation in the complex plane. The time evolution operator then reads $e^{-\tau \mathcal{H}}$ and Eq. (2.7) becomes

$$G_T(j, \tau'; i, \tau) = -\langle \mathcal{T} c(j, \tau') c^\dagger(i, \tau) \rangle \tag{2.8}$$

and is coined temperature Green's function. $\mathcal{T}$ now orders imaginary times τ the same way it ordered real times before. The advantage of this transformation becomes apparent when one looks at the time evolution of the creation and annihilation operators in combination with the thermal average. As illustrated in Fig. 2.1 both the Boltzmann factor as well as the imaginary time propagation lie now on the same axis.

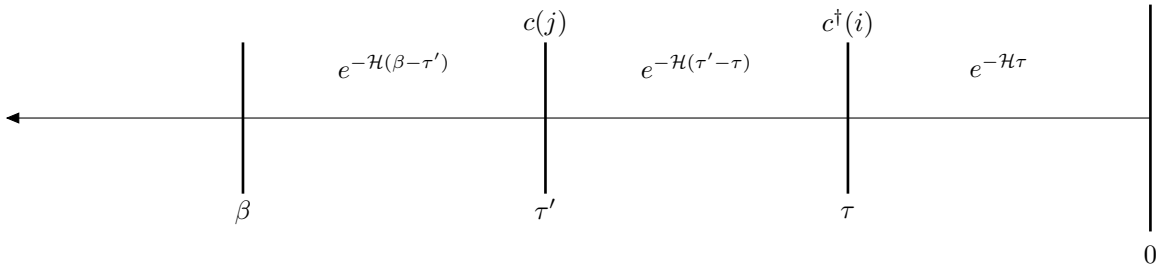

Figure 2.1.: Imaginary time propagation. The Boltzmann factor from the thermal average can here be interpreted as another propagation in (imaginary) time from τ' to β.

The temperature Green's function in Eq. (2.8) is only defined for $0 \leq \tau(\tau') < \beta$, as otherwise the propagators shown in Fig. 2.1 would diverge in the (general) case of a Hamiltonian with no upper bound. Under the condition that $\mathcal{H}$ does not explicitly depend on the time, one can show that Eq. (2.8) is homogeneous in time (i.e. it only depends on the time difference $\tau' - \tau \mathrel{\hat{=}} \tau$ and $-\beta < \tau < \beta$). Using the cyclic properties of the trace one can now further show that $G(\tau)$ is anti-periodic for fermions and periodic for bosons, i.e. $G(-\tau) = \pm G(\beta - \tau)$. Thus τ is restricted to the range,

$$0 \leq \tau < \beta. \tag{2.9}$$

Eq. (2.9) now gives rise to a very neat property when Fourier transforming to frequency space. Since the temperature Green's function is restricted in τ, the (imaginary) frequencies necessarily have to be discrete. Those discrete frequencies are the Matsubara frequencies:

$$w_n = \begin{cases} \frac{2n\pi}{\beta} & \text{(bosons)} \\ \frac{(2n+1)\pi}{\beta} & \text{(fermions).} \end{cases} \tag{2.10}$$

2.3.3. One-particle quantities

In Eq. (2.8) we already defined the one-particle Green's function in imaginary times. A non-interacting Hamiltonian for a crystal is given by

$$\mathcal{H}_0 = \sum_{\mathbf{k}} \epsilon_{\mathbf{k}} c^\dagger_{\mathbf{k}} c_{\mathbf{k}}, \tag{2.11}$$

where $c^\dagger_{\mathbf{k}}$ ($c_{\mathbf{k}}$) is the creation (annihilation) operator in k-space. They are defined via a discrete Fourier transform

$$\begin{aligned} c^\dagger_{\mathbf{k}} &= \frac{1}{\sqrt{N}} \sum_{\mathbf{x}_i} e^{-i\mathbf{k}\mathbf{x}_i} c^\dagger_i, \\ c_{\mathbf{k}} &= \frac{1}{\sqrt{N}} \sum_{\mathbf{x}_i} e^{i\mathbf{k}\mathbf{x}_i} c_i, \end{aligned} \tag{2.12}$$

with N being the number of lattice sites and $\mathbf{x}_i = i \cdot a$, where a is the lattice spacing and $i = (i_x,\ i_y,\ i_z)$ labels the lattice site. $i_{x/y/z}$ runs over all lattice sites in the corresponding direction. The Green's function can be calculated explicitly in momentum-space and is given in frequency representation as:

$$G_0(\mathbf{k}, iw_n) = \frac{1}{iw_n - \epsilon_{\mathbf{k}}}, \tag{2.13}$$

where $\epsilon_{\mathbf{k}}$ is the dispersion relation. However if the Hamiltonian has an interacting part,

$$\mathcal{H} = \mathcal{H}_0 + \mathcal{H}_1, \tag{2.14}$$

the Green's function can in general no longer be calculated analytically. Thus the problem is usually addressed in terms of a perturbation series in the interaction. In the following let us introduce the interaction picture[15] which represents the time evolution of operators in terms of the non-interacting Hamiltonian $\mathcal{H}_0$

$$c_{\mathbf{k}}(\tau) = e^{\mathcal{H}_0 \tau} c_{\mathbf{k}} e^{-\mathcal{H}_0 \tau}. \tag{2.15}$$

Requiring that expectation values of operators are identical in all pictures (Schrödinger, Heisenberg, Interaction), yields the expression for the time evolution operator

$$S(\tau) = e^{\mathcal{H}_0 \tau} e^{-\mathcal{H}\tau}. \tag{2.16}$$

Using Eqs. (2.15) and (2.16), as well as the cyclic properties of the trace, one can rewrite Eq. (2.8) (after going to momentum space)

$$G_T(\mathbf{k},\tau) = -\frac{Tr[e^{-\beta\mathcal{H}_0}\mathcal{T}c_{\mathbf{k}}(\tau)c^{\dagger}_{\mathbf{k}}S(\beta)]}{Tr[e^{-\beta\mathcal{H}_0}S(\beta)]}. \tag{2.17}$$

All operators in Eq. (2.17) are to be understood in terms of the interaction picture as in Eq. (2.15). Any trace where the Boltzmann factor contains $\mathcal{H}_0$, like in Eq. (2.17), will be denoted as $\langle\rangle_0$. Using the equation of motion for the time propagation operator $S(\tau)$, a formal solution can be obtained

$$S(\tau) = 1 - \int_0^{\tau} d\tau' \mathcal{H}_{\mathrm{I}}(\tau') + \int_0^{\tau} d\tau_1 \int_0^{\tau_1} d\tau_2 \mathcal{H}_{\mathrm{I}}(\tau_1)\mathcal{H}_{\mathrm{I}}(\tau_2) - ... \tag{2.18}$$

which is usually denoted as

$$S(\tau) = \mathcal{T}e^{-\int_0^{\tau} d\tau' \mathcal{H}_{\mathrm{I}}(\tau')}. \tag{2.19}$$

Let now consider the interaction part of the Hamiltonian to be a generic two-particle interaction term

$$\mathcal{H}_{\mathrm{I}} = \sum_{\mathbf{k}\mathbf{k}'\mathbf{q}\sigma\sigma'} c^{\dagger}_{\mathbf{k}+\mathbf{q},\sigma}c^{\dagger}_{\mathbf{k}'-\mathbf{q},\sigma'}\frac{V(\mathbf{q})}{2}c_{\mathbf{k}',\sigma'}c_{\mathbf{k},\sigma}. \tag{2.20}$$

Here, $V(\mathbf{q})$ denotes an arbitrary (possibly momentum dependent) interaction and σ denotes the spin index. Inserting the Taylor expansion of Eq. (2.18) into Eq. (2.17) and using the expression of Eq. (2.20) for $\mathcal{H}_i$ gives a series of *non*-interacting expectation values of products of creation and annihilation operators:

$$G_T(\mathbf{k},\tau) = -\frac{1}{\langle S(\beta)\rangle_0}\cdot\sum_{n=0}^{\infty}\frac{(-1)^n}{n!}\int_0^{\beta}d\tau_1\int_0^{\beta}d\tau_2...\int_0^{\beta}d\tau_n\left\langle\mathcal{T}c_{\mathbf{k}}(\tau)c^{\dagger}_{\mathbf{k}}\mathcal{H}_{\mathrm{I}}(\tau_1)...\mathcal{H}_{\mathrm{I}}(\tau_n)\right\rangle_0. \tag{2.21}$$

According to Wick's theorem[23] a *non*-interacting expectation value $\langle\rangle_0$ of n creation and annihilation operators is equivalent to all possible contractions of pairs of operators. Since the average is with respect to the non-interacting Hamiltonian, all pairs which contain an unequal number of creation than annihilation operators vanish. This is a direct consequence of particle number conservation in $\mathcal{H}_0$. Also, in the non-interacting case k is a good quantum number. This means that $\langle c^{\dagger}_{\mathbf{k}}c_{\mathbf{k}'}\rangle_0 = \delta_{\mathbf{k},\mathbf{k}'}\langle c^{\dagger}_{\mathbf{k}}c_{\mathbf{k}}\rangle_0$. To provide a better insight into the perturbation expansion and subsequent translation to diagrams, we illustrate this by performing the first order expansion explicitly. Time arguments are only explicitly listed if a contraction contains two operators with different time arguments.

$$\left\langle \mathcal{T} c_k(\tau) c_k^\dagger c_{k'+q}^\dagger(\tau_1) c_{k''-q}^\dagger(\tau_1) \frac{V(q)}{2} c_{k''}(\tau_1) c_{k'}(\tau_1) \right\rangle_0 = \frac{V(q)}{2} \Big[$$

$$\left\langle \mathcal{T} \overbrace{c_k(\tau) c_k^\dagger} \overbrace{c_{k'+q}^\dagger(\tau_1) c_{k''-q}^\dagger(\tau_1) \frac{V(q)}{2} c_{k''}(\tau_1) c_{k'}(\tau_1)} \right\rangle_0 \hat{=} \left\langle \mathcal{T} c_k(\tau) c_k^\dagger \right\rangle_0 \left\langle c_{k'+q}^\dagger c_{k'} \right\rangle_0 \left\langle c_{k''-q}^\dagger c_{k''} \right\rangle_0 +$$

$$\left\langle \mathcal{T} \overbrace{c_k(\tau) c_k^\dagger} \overbrace{c_{k'+q}^\dagger(\tau_1) c_{k''-q}^\dagger(\tau_1) \frac{V(q)}{2} c_{k''}(\tau_1) c_{k'}(\tau_1)} \right\rangle_0 \hat{=} \left\langle \mathcal{T} c_k(\tau) c_k^\dagger \right\rangle_0 \left\langle c_{k'+q}^\dagger c_{k''} \right\rangle_0 \left\langle c_{k''-q}^\dagger c_{k'} \right\rangle_0 +$$

$$\left\langle \mathcal{T} \overbrace{c_k(\tau) c_k^\dagger} \overbrace{c_{k'+q}^\dagger(\tau_1) c_{k''-q}^\dagger(\tau_1) \frac{V(q)}{2} c_{k''}(\tau_1) c_{k'}(\tau_1)} \right\rangle_0 \hat{=} \left\langle \mathcal{T} c_k(\tau) c_{k''-q}^\dagger(\tau_1) \right\rangle_0 \left\langle \mathcal{T} c_k^\dagger c_{k''}(\tau_1) \right\rangle_0 \left\langle c_{k'+q}^\dagger c_{k'} \right\rangle_0 +$$

$$\left\langle \mathcal{T} \overbrace{c_k(\tau) c_k^\dagger} \overbrace{c_{k'+q}^\dagger(\tau_1) c_{k''-q}^\dagger(\tau_1) \frac{V(q)}{2} c_{k''}(\tau_1) c_{k'}(\tau_1)} \right\rangle_0 \hat{=} \left\langle \mathcal{T} c_k(\tau) c_{k'+q}^\dagger(\tau_1) \right\rangle_0 \left\langle \mathcal{T} c_k^\dagger c_{k'}(\tau_1) \right\rangle_0 \left\langle c_{k''-q}^\dagger c_{k''} \right\rangle_0 +$$

$$\left\langle \mathcal{T} \overbrace{c_k(\tau) c_k^\dagger} \overbrace{c_{k'+q}^\dagger(\tau_1) c_{k''-q}^\dagger(\tau_1) \frac{V(q)}{2} c_{k''}(\tau_1) c_{k'}(\tau_1)} \right\rangle_0 \hat{=} \left\langle \mathcal{T} c_k(\tau) c_{k''-q}^\dagger(\tau_1) \right\rangle_0 \left\langle \mathcal{T} c_k^\dagger c_{k'}(\tau_1) \right\rangle_0 \left\langle c_{k'+q}^\dagger c_{k''} \right\rangle_0 +$$

$$\left\langle \mathcal{T} \overbrace{c_k(\tau) c_k^\dagger} \overbrace{c_{k'+q}^\dagger(\tau_1) c_{k''-q}^\dagger(\tau_1) \frac{V(q)}{2} c_{k''}(\tau_1) c_{k'}(\tau_1)} \right\rangle_0 \hat{=} \left\langle \mathcal{T} c_k(\tau) c_{k'+q}^\dagger(\tau_1) \right\rangle_0 \left\langle \mathcal{T} c_k^\dagger c_{k''}(\tau_1) \right\rangle_0 \left\langle c_{k''-q}^\dagger c_{k'} \right\rangle_0 \Big] \tag{2.22}$$

Since it is rather tedious to write all these contractions in the general case, a diagrammatic representation is usually used. In this work we will be using Feynman diagrams which are constructed from *non*-interacting Green's functions ⟶ ($\hat{=} G_0$) and interactions ∿∿∿ ($\hat{=} V(\mathbf{q})$). Using those elements, Eq. (2.22) can be expressed in four distinct diagrams:

$$\left\langle \mathcal{T} c_k(\tau) c_k^\dagger c_{k'+q}^\dagger(\tau_1) c_{k''-q}^\dagger(\tau_1) \frac{V(q)}{2} c_{k''}(\tau_1) c_{k'}(\tau_1) \right\rangle_0 = \tag{2.23}$$

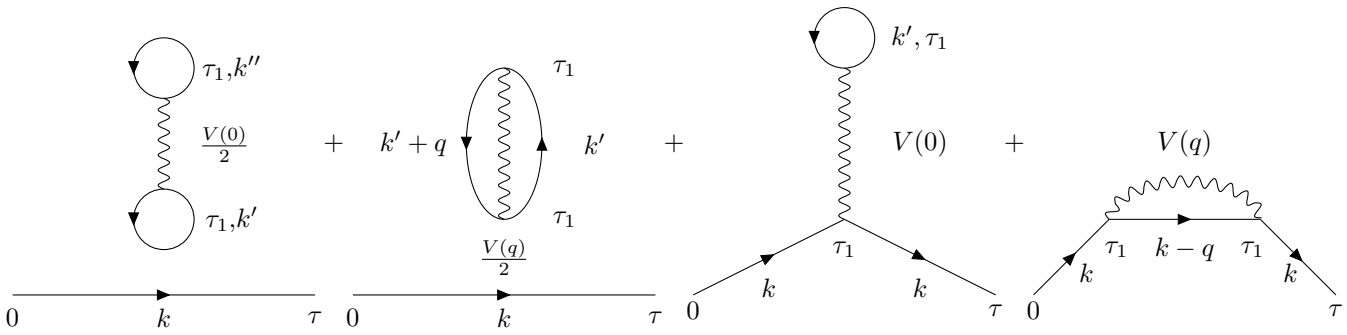

In Eq. (2.23) the first two terms are called disconnected diagrams, since not all Green's functions are connected by either fermionic or interaction lines. The third term is called Hartree-term and represents interaction with the "background" electron density, which is represented by the bubble $\{\mathbf{k}', \tau_1\}$. The fourth term is called Fock-term and can be interpreted as the interaction of a particle with itself at a later time. It can be shown, that all disconnected diagrams are cancelled by the partition sum $\langle S(\beta) \rangle_0$ in the denominator, which is called "linked cluster theorem".

After having introduced the tools to compute the one-particle Green's functions we can now discuss the connection to the spectral function $A(\omega, \mathbf{k})$. The relation is given by,

$$A(\omega, \mathbf{k}) = -\frac{1}{\pi}\Im\big(G^R(\omega, \mathbf{k})\big). \tag{2.24}$$

In the interacting case it encodes all interactions on the single particle level, i.e. the expectation value of any single particle operator $\hat{O} = \sum_{\alpha,\beta} O_{\alpha,\beta} c^\dagger_\alpha c_\beta$ can be calculated directly from the spectral function. The sum over $\mathbf{k}$ yields the local spectral function

$$A(\omega) = -\frac{1}{\pi}\Im\Big(\sum_{\mathbf{k}} G^R(\omega, \mathbf{k})\Big), \tag{2.25}$$

which is in absence of two-particle interactions identical to the common *non*-interacting DOS.

2.3.4. Two-particle quantities

While one-particle quantities yield important information about the one-particle spectrum, the response of the system to external perturbation is given by two-particle quantities.
In the following we analyse the linear response to a perturbation. Let $\mathcal{H}_0$ be a time-independent Hamiltonian of the system and V_t a time-dependent part originating from a external perturbation. V_t couples to the operator $\hat{A}$ via

$$V_t = -\hat{A}a(t), \tag{2.26}$$

where $a(t)$ is any function of t, which has to hold $|a(t)| \ll \frac{|\langle\hat{\mathcal{H}}_0\rangle|}{|\langle\hat{A}\rangle|}$ in order to apply linear response theory. The response of the system is expressed by a change of the expectation value of an operator of interest $\hat{B}$. To express the relation between the change of $\langle\hat{B}\rangle$ and $a(t)$, the susceptibility χ_{BA} is introduced,

$$\langle\hat{B}\rangle_V(t) - \langle\hat{B}\rangle_{V=0} = \int_{-\infty}^{\infty} dt'\ \chi_{BA}(t-t')\ a(t') + \mathscr{O}(a(t)^2). \tag{2.27}$$

Please note that the time dependence of $\langle\hat{B}\rangle_V(t)$ originates from the time-dependent perturbation V_t. From Eq. (2.27) the well known Kubo-Nakano equation can be derived[15]

$$\chi_{BA}(t-t') = \frac{-1}{i\hbar}\Theta(t-t')\langle\big[\hat{B}(t), \hat{A}(t')\big]\rangle_{V=0}. \tag{2.28}$$

$\hat{B}(t)$ and $\hat{A}(t')$ are now to be understood in the interaction picture. Eq. (2.28) has two important properties. First χ_{BA} does not depend on the perturbation function $a(t)$, but only on the operator $\hat{A}$, which the perturbation couples to. Second, if $\hat{B}$ and $\hat{A}$ are one-particle operators, i.e. given by $\sum_{\alpha,\beta} c^\dagger_\alpha(\tau_1)c_\beta(\tau_2)$, we can introduce a generalized susceptibility $\chi^{\nu\nu'\omega}_{\mathbf{kk'q}\sigma\sigma'}$ which is connected to the two-particle Green's function

$$G^{(2)}_{i_1 i_2 i_3 i_4} = \langle\mathcal{T}_\tau[c_{i_1}(\tau_1)c_{i_2}(\tau_2)c^\dagger_{i_3}(\tau_3)c^\dagger_{i_4}(\tau_4)]\rangle. \tag{2.29}$$

This connection is displayed using Matsubara frequencies as[6]

$$\begin{aligned}\chi^{\nu\nu'\omega}_{\mathbf{kk'q}\sigma\sigma'} &= G^{(2),\nu\nu'\omega}_{\mathbf{kk'q}\sigma\sigma'} - \beta G_{\mathbf{k}\nu} G_{\mathbf{k'}\nu'} \delta_{\omega 0}\delta_{\mathbf{q}0} \\ &= \chi^{\nu\nu'\omega}_{0,\mathbf{kk'q}} - G_{\mathbf{k}\nu} G_{(\mathbf{k}+\mathbf{q})(\nu+\omega)} F^{\nu\nu'\omega}_{\mathbf{kk'q}\sigma\sigma'} G_{\mathbf{k'}\nu'} G_{(\mathbf{k'}+\mathbf{q})(\nu'+\omega)}.\end{aligned} \tag{2.30}$$

In Eq. (2.30) the label (2) denotes that it is a two-particle Green's function. χ_0 is the bare susceptibility and F is called the vertex function which encodes all two-particle interaction diagrams. This representation is applicable for most practical purposes like, spin, magnetic or charge susceptibility and can also be represented diagrammatically. This depicted in Fig. 2.2 employing the "4-notation" in which each k also implicitly includes the corresponding frequency ν, thus $k := \{\mathbf{k}, \nu\}$.

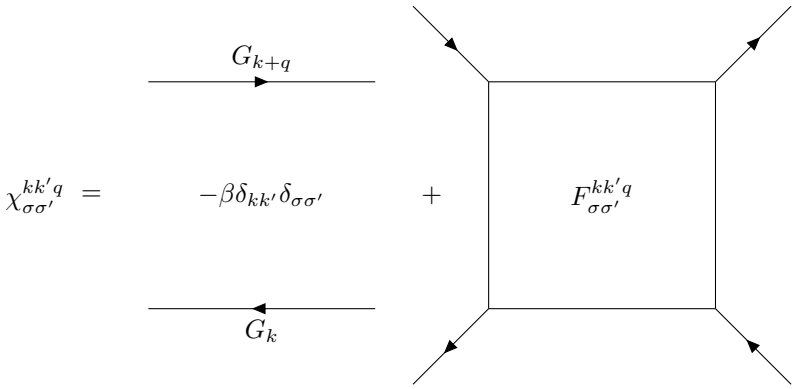

Figure 2.2.: Diagrammatic representation of the generalized suszeptibility. The first term on the right hand side represents the bare susceptibility χ_0 and the second term illustrates the vertex corrections. [recreation after Ref. 6]

The vertex function F can be decomposed in so-called channels: fully irreducible Λ, particle-hole Φ_{ph}, particle-hole transversal $\Phi_{\overline{ph}}$ and particle-particle Φ_{pp}. Each diagram that is not fully irreducible is two-particle reducible in exactly one of the other three channels, i.e. it can be split into two parts by cutting two fermionic lines. This decomposition is illustrated in Fig. 2.3.

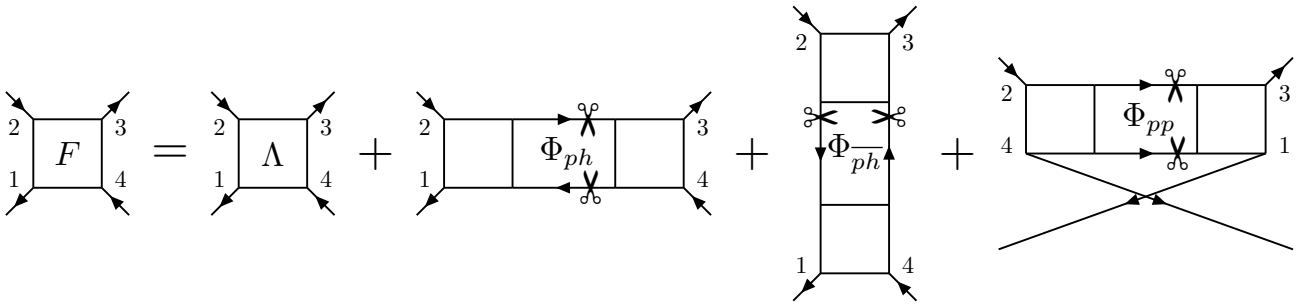

Figure 2.3.: Decomposition of the vertex function F in the 4 channels. From left to right: fully irreducible Λ, particle-hole Φ_{ph}, particle-hole transversal $\Phi_{\overline{ph}}$ and particle-particle Φ_{pp}. The scissors indicate cutting lines to separate diagrams. [Recreation after Ref. 24]

2.3.5. Analytic continuation to real frequencies

As mentioned before the Matsubara formalism provides a convenient way of dealing with Green's functions. However, imaginary frequencies or times have two obvious drawbacks: First, their physical interpretation is difficult, and second, direct comparison with any experiment is impossible. Thus, the so-called analytic continuation is unavoidable. Analytic continuation is the extension of an analytic function to whole region where it is analytic, i.e. infinitely many times differentiable.
For an object which depends on one frequency only, the relation between Matsubara and real frequency is given by a simple substitution of the Matsubara frequency $i\omega_n \to z$. However, one needs to be careful since three distinct Green's function exist in real space (retarded, advanced, causal), while there is only one (temperature) in Matsubara space. Each Green's function corresponds to a different contour and thus requires a different substitution of $i\omega_n$, i.e

$$i\omega_n \to \begin{cases} \omega + i0^+ & ; \text{ retarded} \\ \omega - i0^+ & ; \text{ advanced} \\ \omega + \mathrm{sgn}(\omega) i0^+ & ; \text{ causal} \end{cases} \tag{2.31}$$

The definitions for Green's functions in real and imaginary times was introduced in Eqs. (2.7) and (2.8), however can easily be extended to the general case. Using this definition for real and imaginary times $\chi^R(\omega)$ can be obtained by two ways: either via Fourier transforming the $\chi^R(t-t')$ Eq. (2.32)(i), o via Fourier transform of $\chi(\tau)$ and subsequent substitution $i\omega_n \to w + i0^+$ Eq. (2.32)(ii)

$$\chi^R_{BA}(\omega) = \begin{cases} +i \int_0^{+\infty} dt\ e^{i(\omega+i0^+)t} \langle [\hat{B}(t), \hat{A}(0)] \rangle_{V=0} & ; \text{ real time (i)} \\ \\ \int_0^{\beta} d\tau\ e^{\omega+i0^+\tau} \langle \mathcal{T}_\tau \hat{B}(\tau)\ \hat{A}(0) \rangle_{V=0} & ; \text{ imaginary time (ii).} \end{cases} \tag{2.32}$$

The consistency of the two definitions in Eq. (2.32) can be proven via means of contour integration, which is graphically displayed in Fig. 2.4. The upper (lower) contour connects the retarded (advanced) function to the imaginary time function. The integral along the path has to be zero, as the function is analytic within. The path labelled (1a/b) corresponds to the imaginary time representation (ii) in Eq. (2.32), while the paths (2a/b & 4a/b) create the two parts of the commutator for (i). Only remaining is the path (3a/b), which corresponds to $\Im(\tau) \equiv t = \pm\infty$ and vanishes due to the exponential suppression of the term $e^{\mp 0^+ t}$. Hence, we could show the equivalence of the two formal definitions (i) and (ii) in Eq. (2.32).

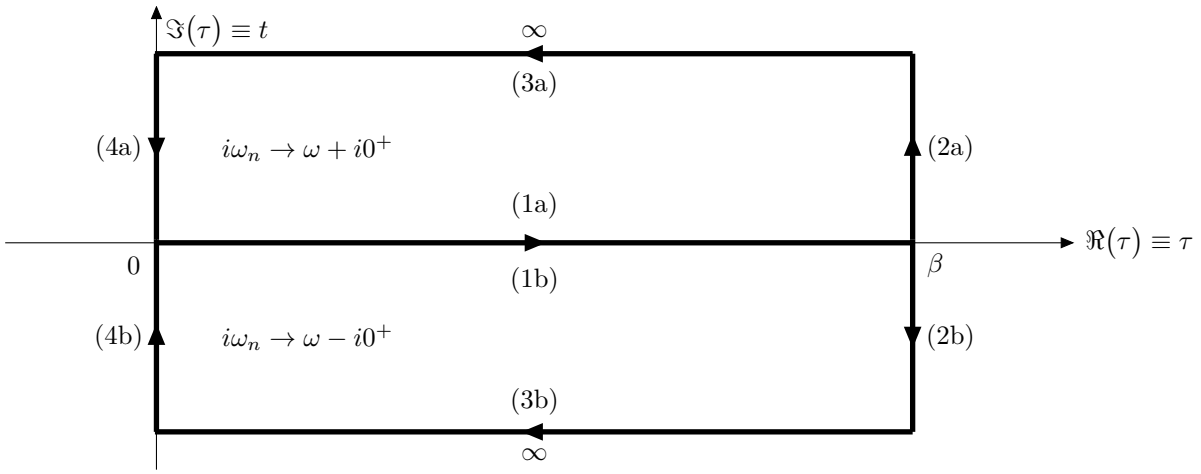

Figure 2.4.: Path in the complex plane to show the identity of the two formal definitions (i) and (ii) for Eq. (2.32). For a detailed explanation see text.

2.3.6. Evaluation of Matsubara sums

While the substitution presented in Eq. (2.31) is perfectly adequate for one-frequency objects, for many practical applications it is not. First for many-frequency objects one has to be very careful in which order the limits $\lim_{0^+\to 0}$ are performed. In that case, terms with $0_1^+ - 0_2^+$ may arise and it is challenging to correctly deal with such expressions. Second for numerical data the scheme presented above is inherently not applicable. To deal with numerical data, numerical analytical continuation algorithms are used, like MaxEnt[14] or Padé-interpolation[25] . And third, many equations (like the parquet equations or the Schwinger-Dyson equation) have been derived in Matsubara frequencies. Instead of performing the same derivation in real time it is often more practical to use the analytic continuation. However, in such equations, sums over Matsubara frequencies appear frequently. A procedure to replace those sums over imaginary frequencies by an integrations over real frequencies is presented below. A pedagogical introduction to analytic continuation can also be found in Ref. 1.
Let us consider a generic function $f \in C^\infty(D_- \cup D_+)$ with $D_\pm = \{z \in \mathbb{C} : \Im(z) \gtrless 0\}$, i.e. the function is analytic in the upper(lower) complex plane. Let us now consider the Matsubara sum over this function $\sum_n f(i\nu_n)$. We can use the residue theorem

$$\oint_C f(z)dz = 2\pi i \sum_{k=1}^{N} Res(f(z), a_k), \tag{2.33}$$

to replace a sum of residuals by an contour integration around the poles. N is the number of poles of the function $f(z)$ within the contour C. The residue of a simple pole at a_k is defined via Eq. (2.34).

$$Res(f(z), a_k) = \lim_{z\to a_k} \big((z - a_k)f(z)\big) \tag{2.34}$$

Since the Fermi (Bose) function η_F (η_B) has poles at the fermionic (bosonic) Matsubara frequencies we use the residue theorem in "reverse" to write a Matsubara sum as:

$$\frac{1}{\beta}\sum_{\nu_n} f(i\nu_n) = \frac{-1}{2\pi i}\oint_C dz\ \eta_F(z)f(z). \tag{2.35}$$

The contour consists of circles just around the poles. Further deformation of this contour is shown in Fig. 2.5.

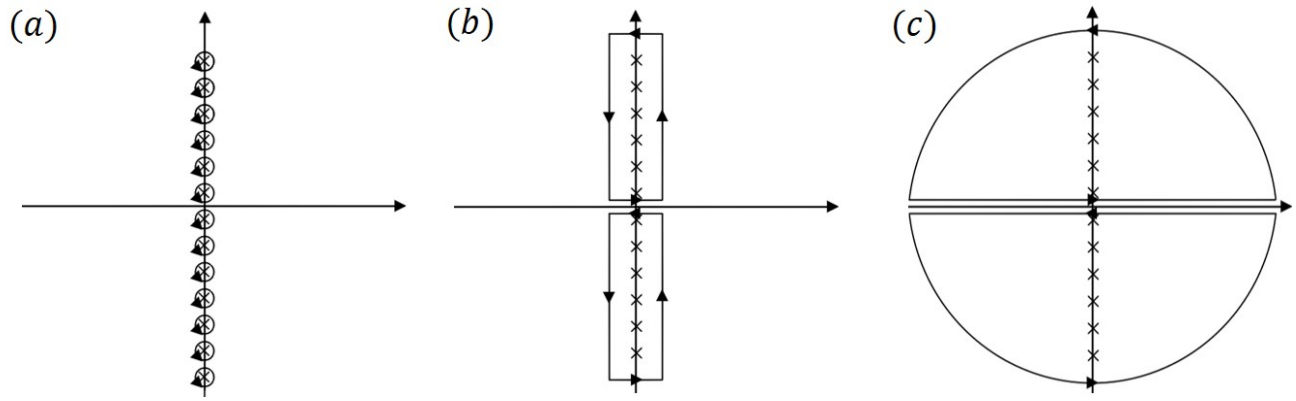

Figure 2.5.: Contour in the complex plane to rewrite a Matsubara sum as an integral. (a) The x-marks label the discrete Matsubara frequencies. Those points are also the poles of the Fermi function η_F. First the contour is chosen to enclose only the poles. (b) Circles are stretched and deformed into rectangles and paths between the poles cancel pairwise. (c) The final contour is made of two closed half-circles in the upper and lower complex plane, which is obtained by simply stretching the rectangles of (b)

In Fig. 2.5(c) the half-circles can be suppressed by introducing a regulator $e^{\pm iz0^+}$, leaving only the integration lines from $-\infty \to \infty$. Hence we can write:

$$\begin{aligned}\frac{1}{\beta}\sum_n f(i\nu_n) &= \frac{-1}{2\pi i}\left(\int_{-\infty}^{\infty} d\nu\ \eta_F(\nu+i0^+)f(\nu+i0^+) + \int_{+\infty}^{-\infty} d\nu\ \eta_F(\nu-i0^+)f(\nu-i0^+)\right) \\ &= \frac{-1}{2\pi i}\int_{-\infty}^{\infty} d\nu\ \eta_F(\nu)\big(f^R(\nu)-f^A(\nu)\big).\end{aligned} \tag{2.36}$$

In Eq. (2.36) we used for the last equality the naming convention from Eq. (2.31). However, it is important to note that the function $f(z)$ may have branch-cut along the real axis and hence the contour may not cross it. When dealing with more complex objects several such branch-cuts may appear in which case the integral has to be split in as many sections accordingly.

3. Optical conductivity

In this chapter we will present a short derivation of the current-current correlator, from which the optical conductivity can be calculated. We will first derive a general expression and then assume the vertex function F to depend only on one bosonic frequency. This will allow us to derive a real-frequency expression for the current-current correlator. At the end of this chapter there will be a short remark on the f-sum rule and Drude conductivity.

3.1. Expression for the optical conductivity

The optical conductivity σ is defined as the coefficient relating the current J to an external field E oscillating with frequency ω

$$J(\omega) = \sigma(\omega)E(\omega). \tag{3.1}$$

Through the use of the Kubo-Nakano equation Eq. (2.28) an explicit expression for σ can be obtained[26]:

$$\langle J(\omega)\rangle_E = \underbrace{\frac{\chi_{jj,q} - \frac{q^2 n_q}{m}}{i[\omega + i0^+]}}_{\sigma(\omega)} E(\omega). \tag{3.2}$$

$\chi_{jj,q}$ is the current-current correlation function, n_q is the electron density, m the electron mass and 0^+ stems from the analytical continuation to real frequencies. Since we are talking about response functions the contour is chosen to yield a retarded quantity (Eq. (2.31)). Since we are only interested in the real part of $\sigma(\omega)$, we use Plemelj's formula, $\frac{1}{x+i0^+} = \frac{\mathcal{P}}{x} - i\pi\delta(x)$ to find

$$\Re\big(\sigma(\omega)\big) = \mathcal{P}\frac{\Im(\chi_{jj,q})}{\omega} - \pi\delta(\omega)\left[\Re(\chi_{jj,q}) - \frac{q^2 n_q}{m}\right]. \tag{3.3}$$

In Eq. (3.3) the second term is usually called "diamagnetic term" and only contributes to $\sigma(\omega = 0)$ and will be neglected further on. Moving on we will write $\sigma(\omega)$ as a substitute for $\Re\big(\sigma(\omega)\big)$, as the imaginary is not considered in this thesis.

3.2. Current-current correlator from linear response

The first term in Eq. (3.3) is called the paramagnetic contribution and is directly linked to the paramagnetic current-current correlator, which is given by Eq. (2.28) with $\hat{B} = j_{\mathbf{r},t}$ and $\hat{A} = j_{\mathbf{r'},t'}$. In frequency and momentum space it is given by

$$\chi_{jj,q} = \int_0^\beta e^{i\omega_n \tau} \langle j_{\mathbf{q}}(\tau) j_{\text{-}\mathbf{q}} \rangle_{J=0}. \tag{3.4}$$

The current $j_{\mathbf{r}}$ is given by the usual expression

$$j_{\mathbf{r}} = \frac{-iq}{2m} \psi^\dagger(\mathbf{r}) \big(\overrightarrow{\nabla} - \overleftarrow{\nabla} \big) \psi(\mathbf{r}), \tag{3.5}$$

where ψ and $\psi^\dagger$ are field operators. For square lattice systems Eq. (3.5) is given in momentum representation by[26]

$$j_{\mathbf{q}} = it \sum_{\sigma \mathbf{k}} \left[e^{-i(\mathbf{k}+\mathbf{q})\mathbf{a}_\alpha} - e^{i\mathbf{k}\mathbf{a}_\alpha} \right] c^\dagger_{\mathbf{k}\sigma} c_{\mathbf{k}\sigma} \overset{\mathbf{q}=0}{=} 2\ \mathrm{t} \sum_{\sigma \mathbf{k}} \sin(\mathbf{k}\mathbf{a}_\alpha) c^\dagger_{\mathbf{k}\sigma} c_{\mathbf{k}\sigma}, \tag{3.6}$$

where $c^\dagger(c)$ are creation (annihilation) operators in momentum space defined in Eq. (2.12). t is the hopping amplitude and $\mathbf{a}_\alpha$ is the direction of the electric field. $2\ \mathrm{t} \sin(\mathbf{k}\mathbf{a}_\alpha)$ can conveniently be written as $\frac{\partial \epsilon_{\mathbf{k}}}{\partial \mathbf{k}_\alpha}$, where $\epsilon_{\mathbf{k}}$ is the dispersion relation for a tight binding square lattice model as given in Eq. (3.7).

$$\epsilon_{\mathbf{k}} = -2\ \mathrm{t}\ \big(\cos(\mathbf{k}_x \mathbf{a}) + \cos(\mathbf{k}_y \mathbf{a}) \big). \tag{3.7}$$

Using Eqs. (3.4) and (3.7) together with Eq. (2.30) one can arrive at the final expression for the current-current correlator[26].

$$\chi(\omega, \mathbf{q}) = -\frac{2}{\beta} \sum_k \left[\gamma^{\mathbf{k}}_\alpha \right]^2 G_{k+q} G_k - \frac{2}{\beta} \sum_{kk'} \gamma^{\mathbf{k}}_\alpha \gamma^{\mathbf{k}'}_\alpha G_k G_{k+q} F_{kk'q} G_{k'} G_{k'+q}, \tag{3.8}$$

where $\gamma^{\mathbf{k}}_\alpha = \frac{\partial \epsilon_{\mathbf{k}}}{\partial \mathbf{k}_\alpha}$ and we used the compact "4-vector" notation $k = \{\mathbf{k}, i\nu_n\}$. If the electric field is varying slowly on the scale of the lattice it is sufficient to restrict to $\mathbf{q} = 0$. Moving on we will always consider $\chi(\omega, \mathbf{q} = 0)$ if no explicit $\mathbf{q}$ dependence is stated. The Feynman diagram for Eq. (3.8) is depicted in Fig. 4.1.

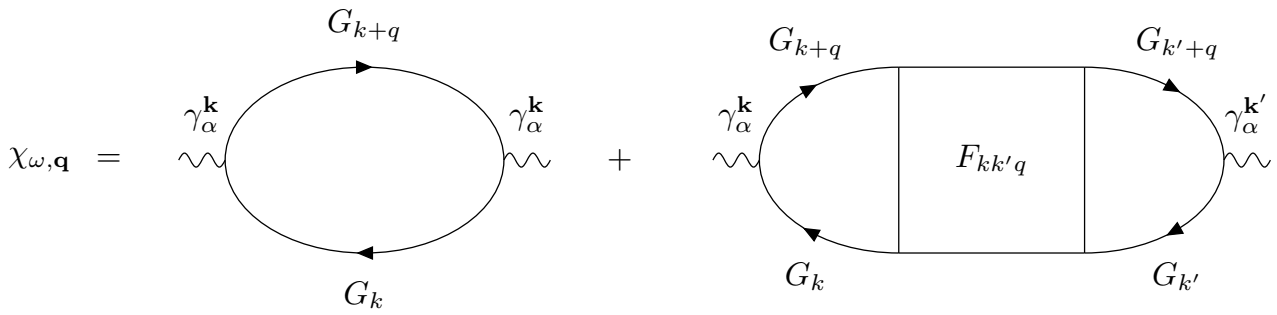

Figure 3.1.: Feynman diagram for Eq. (3.8). Straight lines denote the Green's functions and the wiggly lines are the operators corresponding to the electric field. The left diagram corresponds to the bubble contribution χ_{bub} and the right one to the vertex corrections χ_{vert}. α denotes the direction of the electric field.

3.3. Analytical continuation of a simplified current-current correlator

In this section we will consider a simplified version for the current-current correlator Eq. (3.8), where we assume that the full vertex $F_{kk'q}$ can be approximated by a one-frequency object $F^{\mathbf{k}-\mathbf{k}'}_{i\nu_n - i\nu_{n'}}$. This is motivated by the $\overline{\text{ph}}$ diagrams, which have been identified to be responsible for the majority of the vertex-corrections[12]. In the $\overline{\text{ph}}$ channel it is presumed, that dominant diagrams are ladder diagrams which are of reduced frequency dependence and can be written as a one-frequency object. At this point we want to stress, that our real-frequency formalism allows for direct calculation of the vertex-corrections and thus a higher resolution. Approaches using Matsubara frequencies, as in Ref. 12, have to continue the result to real frequencies. This, however, cannot be done for the vertex corrections alone, but only for σ_{bub} and σ, i.e. only the bubble only or bubble plus corrections. Hence, to obtain the vertex corrections two quantities, which have been analytically continued, have to be subtracted: $\sigma_{\text{vert}} = \sigma - \sigma_{\text{bub}}$. Since both σ and σ_{bub} are prone to errors due to the analytic continuation, results are not as reliable.

3.3.1. Bubble contribution

In Eq. (3.8) the first part is the contribution of the bubble $\chi_{bub}(\omega)$

$$\chi_{\text{bub}}(i\omega_n, \mathbf{q}) = -\frac{2}{\beta}\sum_{k}\left[\gamma^{\mathbf{k}}_{\alpha}\right]^2 G_{k+q}G_k. \tag{3.9}$$

The branch-cuts in Eq. (3.9) are at

$$z = \begin{cases} \nu, \\ \nu - i\omega_n. \end{cases} \tag{3.10}$$

Using the expression from Eq. (2.36) we can rewrite Eq. (3.9) as,

$$\begin{aligned}\chi_{\text{bub}}(i\omega_n, \mathbf{q}) = -2\sum_{\mathbf{k}}\left[\gamma^{\mathbf{k}}_{\alpha}\right]^2 \frac{-1}{2\pi i}\int_{-\infty}^{+\infty} d\nu\ \eta_F(\nu)\Big[G^{\mathbf{k}+\mathbf{q}}_{\nu+i\omega_n}\left(G^{\mathbf{k}}_{\nu+i0^+} - G^{\mathbf{k}}_{\nu-i0^+}\right) + \\ G^{\mathbf{k}}_{\nu-i\omega_n}\left(G^{\mathbf{k}+\mathbf{q}}_{\nu+i0^+} - G^{\mathbf{k}+\mathbf{q}}_{\nu-i0^+}\right)\Big].\end{aligned} \tag{3.11}$$

Where $G_{\nu+i0^+}(G_{\nu-i0^+})$ is the retarded(advanced) Green's function Eq. (2.31). Eq. (2.25) can be used to rewrite $G^{\text{R},\mathbf{k}}_{\nu} - G^{\text{A},\mathbf{k}}_{\nu} = (-2\pi i)A^{\mathbf{k}}_{\nu}$. Additionally using $\mathbf{q} = 0$ and $i\omega_n = \omega + i0^+$ we arrive at a final expression

$$\chi^{\text{R}}_{\text{bub}}(\omega, \mathbf{q} = 0) = -2\sum_{\mathbf{k}}\left[\gamma^{\mathbf{k}}_{\alpha}\right]^2 \int_{-\infty}^{+\infty} d\nu\ \eta_F(\nu)A^{\mathbf{k}}_{\nu}\left[G^{\text{R},\mathbf{k}}_{\nu+\omega} + G^{\text{A},\mathbf{k}}_{\nu-\omega}\right]. \tag{3.12}$$

Eq. (3.12) is the real-frequency representation for the bubble contribution to the optical conductivity. We want to stress that in order to obtain this expression no simplifications or assumptions have been made. Any simplification are for the vertex-corrections only.

3.3.2. Vertex corrections

The second part in Eq. (3.8) is coined vertex correction and reads with the one-frequency vertex

$$\chi_{\text{vert}}(i\omega_n, \mathbf{q}) = -\frac{2}{\beta^2} \sum_{kk'} \gamma_\alpha^k \gamma_\alpha^{k'} G_k G_{k+q} F_{k-k'} G_{k'} G_{k'+q}. \tag{3.13}$$

Analytic continuation of Eq. (3.13) is algebraically more involved, but follows the same scheme and procedure as for the bubble contribution. Thus some steps will be omitted in the derivation. First let us consider the evaluation of the $i\nu_{n'}$ Matsubara sum. Since branch-cuts appear in both the Green's function G and the one-frequency vertex F, when the imaginary part of the frequency argument vanishes, three will arise which are at:

$$z = \begin{cases} \nu' + i\nu_n, & \text{(i)} \\ \nu', & \text{(ii)} \\ \nu' - i\omega_n & \text{(iii)}. \end{cases} \tag{3.14}$$

The first one in Eq. (3.14) originates from the vertex $F_{i\nu_n - z}^{\mathbf{k}-\mathbf{k}'} \overset{z \to \nu' + i\nu_n}{=} F_{-\nu'}^{\mathbf{k}-\mathbf{k}'}$ in Eq. (3.13). Branch-cuts Eq. (3.14) (i) and Eq. (3.14) (ii) are from the two Green's functions $G_z^{\mathbf{k}'}$ and $G_{z+i\omega_n}^{\mathbf{k}'+\mathbf{q}}$, respectively. However, special care has to be taken since the first branch-cut in Eq. (3.14) is on top of a pole. Thus the point $i\nu_n = i\nu_{n'}$ has to be explicitly excluded from the Matsubara sum and treated differently. This is graphically visualized in Fig. 3.2.

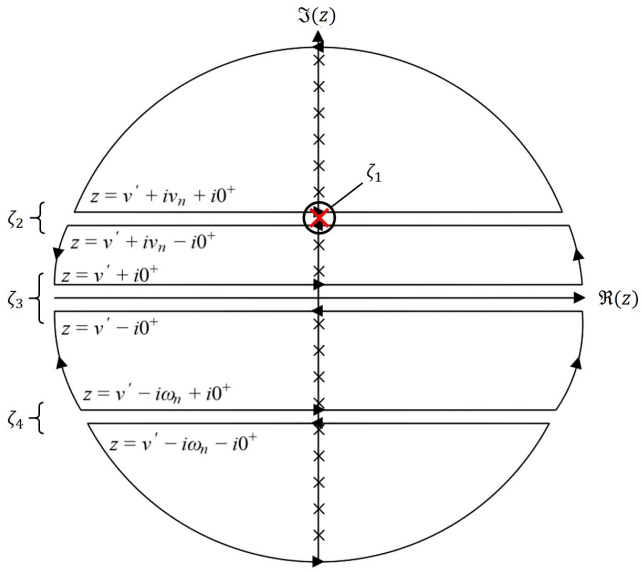

Figure 3.2.: The three branch-cuts for the analytical continuation ($i\nu_n' \to z$) of the first Matsubara sum of Eq. (3.13). The red cross marks the Matsubara frequency $i\nu_n = i\nu_{n'}$ which has to be excluded from the sum and treated separately. The ζ mark their respective integration contours (or in case of ζ_1 the single Matsubara frequency).

We remove the Matsubara frequency $i\nu_n = i\nu'_n$, denoted by the red cross in Fig. 3.2, from the sum to write Eq. (3.13) as,

$$\chi_{\text{vert}}(i\omega_n, \mathbf{q}) = -\frac{2}{\beta^2}\sum_{\mathbf{k}\mathbf{k}'}\gamma^k_\alpha\gamma^{k'}_\alpha\Bigg[F_0^{\mathbf{k}-\mathbf{k}'}\sum_{i\nu_n}G^{\mathbf{k}}_{i\nu_n}G^{\mathbf{k}+\mathbf{q}}_{i\nu_n+i\omega_n}G^{\mathbf{k}'}_{i\nu_n}G^{\mathbf{k}'+\mathbf{q}}_{i\nu_n+i\omega_n} + \sum_{i\nu_n}\sum_{i\nu_{n'}\neq i\nu_n}G^{\mathbf{k}}_{i\nu_n}G^{\mathbf{k}+\mathbf{q}}_{i\nu_n+i\omega_n}F^{\mathbf{k}-\mathbf{k}'}_{i\nu_n-i\nu_{n'}}G^{\mathbf{k}'}_{i\nu_{n'}}G^{\mathbf{k}'+\mathbf{q}}_{i\nu_{n'}+i\omega_n}\Bigg]. \tag{3.15}$$

After replacing the $i\nu'_n$ Matsubara sum by the contours displayed in Fig. 3.2, Eq. (3.14) can be written as

$$\chi_{|vert}(i\omega_n, \mathbf{q}) = -\frac{2}{\beta}\sum_{\mathbf{k}\mathbf{k}'}\gamma^k_\alpha\gamma^{k'}_\alpha\sum_{i\nu_n}\Bigg[\overbrace{\frac{F_0^{\mathbf{k}-\mathbf{k}'}}{\beta}G^{\mathbf{k}}_{i\nu_n}G^{\mathbf{k}+\mathbf{q}}_{i\nu_n+i\omega_n}G^{\mathbf{k}'}_{i\nu_n}G^{\mathbf{k}'+\mathbf{q}}_{i\nu_n+i\omega_n}}^{\zeta_1} + \frac{i}{2\pi}\int_{-\infty}^{+\infty}d\nu'\Big[\overbrace{\eta_B(\nu')G^{\mathbf{k}}_{i\nu_n}G^{\mathbf{k}+\mathbf{q}}_{i\nu_n+i\omega_n}G^{\mathbf{k}'}_{\nu'+i\nu_n}G^{\mathbf{k}'+\mathbf{q}}_{\nu'+i\nu_n+i\omega_n}\big(F^{R,\mathbf{k}-\mathbf{k}'}_{-\nu'} - F^{A,\mathbf{k}-\mathbf{k}'}_{-\nu'}\big)}^{\zeta_2} + \overbrace{\cdot(-2\pi i)\eta_F(\nu')\big(A^{\mathbf{k}'}_{\nu'}G^{\mathbf{k}}_{i\nu_n}G^{\mathbf{k}+\mathbf{q}}_{i\nu_n+i\omega_n}G^{\mathbf{k}'+\mathbf{q}}_{\nu'+i\omega_n}F^{\mathbf{k}-\mathbf{k}'}_{i\nu_n-\nu'} + A^{\mathbf{k}'+\mathbf{q}}_{\nu'}G^{\mathbf{k}}_{i\nu_n}G^{\mathbf{k}+\mathbf{q}}_{i\nu_n+i\omega_n}G^{\mathbf{k}'}_{\nu'-i\omega_n}F^{\mathbf{k}-\mathbf{k}'}_{i\nu_n+i\omega_n-\nu'}\big)}^{\zeta_{3p4}}\Big]\Bigg]. \tag{3.16}$$

The contributions from the different branch-cuts and the excluded Matsubara frequency have been put in brackets and will be referred to as ζ_1, ζ_2 and ζ_{3p4} moving on. Note that ζ_3 and ζ_4 from Fig. 3.2 has been combined to ζ_{3p4}. Conveniently, the two branch-cuts for the analytic continuation of the $i\nu_n$ sum, originate from $G^{\mathbf{k}}_z$(i) and $G^{\mathbf{k}+\mathbf{q}}_{z+i\omega_n}$(ii), which appear in all three contributions. Hence, the branch-cuts are identical for all contribution at:

$$z = \begin{cases}\nu, \\ \nu - i\omega_n.\end{cases} \tag{3.17}$$

Following the same procedure as for the $i\nu'_n$ Matsubara sum we replace the $i\nu$ sum by the contour integration lines at $z = \nu \pm i0^+$ and $z = \nu - i\omega_n \pm i0^+$. Since the response of the system to an external perturbation is a retarded quantity, we perform the analytic continuation of the last frequency ω by the simple substitution $i\omega_n = \omega + i0^+$. The vertex corrections to the susceptibility at $\mathbf{q} = 0$ can then be written as

$$\chi^{\text{R}}_{\text{vert}}(\omega, \mathbf{q}=0) = -2\sum_{\mathbf{k}\mathbf{k}'}\gamma^k_\alpha\gamma^{k'}_\alpha\int_{-\infty}^{+\infty}d\nu\big[\zeta_1^{\mathbf{k}\mathbf{k}'}(\omega) + \zeta_2^{\mathbf{k}\mathbf{k}'}(\omega) + \zeta_{3p4}^{\mathbf{k}\mathbf{k}'}(\omega)\big]. \tag{3.18}$$

The three contributions ζ_1, ζ_2 and ζ_{3p4} evaluate to:

$$\zeta_1(\omega)^{\mathbf{k}\mathbf{k}'} = \frac{i}{2\pi}\frac{F_0^{\mathbf{k}-\mathbf{k}'}}{\beta}\left[G^{\mathrm{R},\mathbf{k}}_{\nu+\omega}G^{\mathrm{R},\mathbf{k}'}_{\nu+\omega} + G^{\mathrm{A},\mathbf{k}}_{\nu-\omega}G^{\mathrm{A},\mathbf{k}'}_{\nu-\omega}\right]\left[G^{\mathrm{R},\mathbf{k}}_{\nu}G^{\mathrm{R},\mathbf{k}'}_{\nu} - G^{\mathrm{A},\mathbf{k}}_{\nu}G^{\mathrm{A},\mathbf{k}'}_{\nu}\right], \tag{3.19a}$$

$$\zeta_2(\omega)^{\mathbf{k}\mathbf{k}'} = \frac{-1}{4\pi}\int_{-\infty}^{+\infty} d\nu'\eta_B(\nu')\left[F^{\mathrm{R},\mathbf{k}-\mathbf{k}'}_{-\nu} - F^{\mathrm{A},\mathbf{k}-\mathbf{k}'}_{-\nu}\right]\left[G^{\mathrm{R},\mathbf{k}}_{\nu+\omega}G^{\mathrm{R},\mathbf{k}'}_{\nu+\nu'+\omega} + G^{\mathrm{A},\mathbf{k}}_{\nu-\omega}G^{\mathrm{A},\mathbf{k}'}_{\nu+\nu'-\omega}\right] \tag{3.19b}$$
$$\left[G^{\mathrm{R},\mathbf{k}}_{\nu}G^{\mathrm{R},\mathbf{k}'}_{\nu} - G^{\mathrm{A},\mathbf{k}}_{\nu}G^{\mathrm{A},\mathbf{k}'}_{\nu}\right],$$

$$\zeta_{3p4}(\omega)^{\mathbf{k}\mathbf{k}'} = \frac{i}{2\pi}\int_{-\infty}^{+\infty} d\nu'\eta_F(\nu')A^{\mathbf{k}'}_{\nu'}\Big[\left[G^{\mathrm{R},\mathbf{k}}_{\nu+\omega}G^{\mathrm{R},\mathbf{k}'}_{\nu'+\omega} + G^{\mathrm{A},\mathbf{k}}_{\nu-\omega}G^{\mathrm{A},\mathbf{k}'}_{\nu'-\omega}\right]\left[G^{\mathrm{R},\mathbf{k}}_{\nu}F^{\mathrm{R},\mathbf{k}-\mathbf{k}'}_{\nu-\nu'} - G^{\mathrm{A},\mathbf{k}}_{\nu}F^{\mathrm{A},\mathbf{k}-\mathbf{k}'}_{\nu-\nu'}\right] + \tag{3.19c}$$
$$(-2\pi i)A^{\mathbf{k}}_{\nu}\left[G^{\mathrm{R},\mathbf{k}'}_{\nu'+\omega}G^{\mathrm{A},\mathbf{k}}_{\nu-\omega}F^{\mathrm{A},\mathbf{k}-\mathbf{k}'}_{\nu-\nu'-\omega} + G^{\mathrm{A},\mathbf{k}'}_{\nu'-\omega}G^{\mathrm{R},\mathbf{k}}_{\nu+\omega}F^{\mathrm{R},\mathbf{k}-\mathbf{k}'}_{\nu-\nu'+\omega}\right]\Big].$$

In Eq. (3.19b) the divergence of $\eta_B(\nu')$ at $\nu' = 0$ is cancelled by $\left[F^{\mathrm{R},\mathbf{k}-\mathbf{k}'}_{-\nu} - F^{\mathrm{A},\mathbf{k}-\mathbf{k}'}_{-\nu}\right]$ which is 0 for $\nu' = 0$. Eq. (3.12) and Eqs. (3.18) and (3.19) are the main equations used in the following chapters. At this point we want to stress that *any* one-frequency vertex-function can be used, not just an RPA-ladder approximation as will mostly be discussed later on.

3.4. *f*-sum rule

Using the Kramers-Kronig relations

$$\chi^{\mathrm{R}}(\omega) = \frac{1}{i\pi}\mathcal{P}\int_{-\infty}^{+\infty}\frac{\chi^{\mathrm{R}}(\omega')}{\omega'-\omega}d\omega', \tag{3.20}$$

where $\chi^{\mathrm{R}}(\omega)$ is retarded function, the optical conductivity $\sigma(\omega)$ can be directly linked to the zeroth Matsubara frequency ($\omega_0 = 0$) current-current correlation function

$$\int\frac{d\omega}{\pi}\sigma_q = \int\frac{d\omega}{\pi}\frac{\Im(\chi_q)}{\omega} = \int\frac{d\omega}{\pi}\frac{\Im(\chi_q)}{\omega - i\omega_0} = \chi_{\mathbf{q},\omega_0}. \tag{3.21}$$

Eq. (3.21) can for $\mathbf{q} = 0$ be further rewritten and for next-nearest-neighbour hopping (nnh) be connected to the kinetic energy of the system[20],

$$\int\frac{d\omega}{\pi}\sigma_{q=0} = \frac{1}{\beta}\sum_k\frac{\partial^2\epsilon_{\mathbf{k}}}{\partial k_\alpha^2}G_k \overset{nnh}{=} \frac{-1}{2\beta}\sum_k\epsilon_{\mathbf{k}}G_k = \frac{-E_{kin}}{2}. \tag{3.22}$$

In the following we will show, that if the self energy is purely local, i.e. $\frac{\partial\Sigma(\omega,\mathbf{k})}{\partial k_i} = 0 \;\; \forall i \in \{x,y,z\}$, and the operator γ_α is the derivative of the dispersion relation $\frac{\partial\epsilon_{\mathbf{k}}}{\partial k_\alpha}$, the full optical weight is given by the bubble contribution. Hence, *vertex corrections may only shift weight but not add any.* This allows one to benchmark the code for such self-energies and gives valuable feedback about the simplifications one has made with respect to the vertex-corrections.
In order to show the aforementioned statement, we perform analytical continuation for the bubble term of the current-current correlator Eq. (3.23),

$$\chi_{\text{bub}}(\mathbf{q}, i\omega_n) = -\frac{2}{\beta}\sum_k \left[\gamma_\alpha^{\mathbf{k}}\right]^2 G_{k+q}G_k \overset{q=0,i\omega_n=i\omega_0=0}{=} -\frac{2}{\beta}\sum_k \left[\gamma_\alpha^{\mathbf{k}}\right]^2 G_k G_k. \tag{3.23}$$

Recalling Eq. (3.12), Eq. (3.23) can after some algebraic rearrangements be written as,

$$\chi_{\text{bub}}(\mathbf{q}=0, i\omega_n=0) = -\frac{i}{2\pi}\sum_{\mathbf{k}} \left[\gamma_\alpha^{\mathbf{k}}\right]^2 \int_{-\infty}^{+\infty} d\nu\ \eta_F(\nu)\left[G_\nu^{\mathrm{R},\mathbf{k}}G_\nu^{\mathrm{R},\mathbf{k}} - G_\nu^{\mathrm{A},\mathbf{k}}G_\nu^{\mathrm{A},\mathbf{k}}\right]. \tag{3.24}$$

In the case of a purely local self-energy we can write the derivative of the Green's function with respect to k_α as

$$\frac{\partial G_\nu^{\mathrm{R/A},\mathbf{k}}}{\partial k_\alpha} = \frac{\partial G_\nu^{\mathrm{R/A},\mathbf{k}}}{\partial \epsilon_{\mathbf{k}}}\frac{\partial \epsilon_{\mathbf{k}}}{\partial k_\alpha} = \frac{\partial \epsilon_{\mathbf{k}}}{\partial k_\alpha}\frac{\partial}{\partial \epsilon_{\mathbf{k}}}\left(\frac{1}{\nu - \epsilon_{\mathbf{k}} + \Sigma^{\mathrm{R/A}}(\omega)}\right) = \frac{\partial \epsilon_{\mathbf{k}}}{\partial k_\alpha}\left(G_\nu^{\mathrm{R/A},\mathbf{k}}\right)^2. \tag{3.25}$$

With Eq. (3.25) we can rewrite Eq. (3.24),

$$\chi_{\text{bub}}(q=0, i\omega_n=0) = -\frac{i}{2\pi}\sum_{\mathbf{k}} \frac{\partial \epsilon_{\mathbf{k}}}{\partial k_\alpha}\int_{-\infty}^{+\infty} d\nu\ \eta_F(\nu)\frac{\partial}{\partial k_\alpha}\left[G_\nu^{\mathrm{R},\mathbf{k}} - G_\nu^{\mathrm{A},\mathbf{k}}\right]. \tag{3.26}$$

Assuming, that the k-sum is sufficiently dense, a transition to an integral is justified $\frac{1}{N}\sum_{\mathbf{k}} \to \frac{1}{(2\pi)^d}\int d\mathbf{k}$, and using the common relation $G_\nu^{\mathrm{R},\mathbf{k}} - G_\nu^{\mathrm{A},\mathbf{k}} = -2\pi i\ A_\nu^{\mathbf{k}}$, we can use partial integration to move the partial derivative from A to ϵ.

$$\chi_{\text{bub}}(q=0, i\omega_n=0) = -\int d\{\mathbf{k}\neq k_\alpha\}\frac{\partial \epsilon_{\mathbf{k}}}{\partial k_\alpha}\int_{-\infty}^{+\infty} d\nu\ \eta_F(\nu)A_\nu^{\mathbf{k}}\Big|_0^{2\pi} + \int d\mathbf{k}\frac{\partial^2 \epsilon_{\mathbf{k}}}{\partial k_\alpha^2}\int_{-\infty}^{+\infty} d\nu\ \eta_F(\nu)A_\nu^{\mathbf{k}}. \tag{3.27}$$

Here $d\{\mathbf{k}\neq k_\alpha\}$ denotes the integration over all components of $\mathbf{k}$ except k_α which has been eliminated by the partial integration. For the square lattice tight binding model $\frac{\partial \epsilon_{\mathbf{k}}}{\partial k_{x/y}} = 2\mathrm{t}\,\sin(k_{x/y})$ which vanishes at the boundaries $\{0, 2\pi\}$. Hence, we can write the final expression to be,

$$\chi_{\text{bub}}(\mathbf{q}=0, i\omega_n=0) = +\int d\mathbf{k}\frac{\partial^2 \epsilon_{\mathbf{k}}}{\partial k_\alpha^2}\int_{-\infty}^{+\infty} \eta_F(\nu)A_\nu^{\mathbf{k}} = \int \frac{d\omega}{\pi}\sigma_{q=0}. \tag{3.28}$$

In the last equality of Eq. (3.28) we used the fist equality of Eq. (3.22). Thus for a local self-energy the full optical weight is given by the bubble contribution alone and (consistent) vertex corrections may only shift the weight.
The code used for all results concerning the real-frequency calculations has been benchmarked with respect to this sum-rule. Within the numerical error the sum rule is fulfilled with the bubble contribution alone.

3.5. Drude conductivity for the disordered electron gas

Even tough the Drude conductivity Eq. (3.29) is a classical theory, Drude peaks are often used to fit the low ω behaviour of optical conductivity spectra[27],

$$\sigma(\omega) = \frac{ne^2}{m}\frac{1}{i\omega - 1/\tau}, \tag{3.29}$$

where τ is the lifetime of the scattering particles, n the electron density and m the electron mass. Moreover, this behaviour can also be recovered by means of quantum field theory. See for instance Altland-Simons[1] chapter 7.4.1 *'Longitudinal conductivity of the disordered electron gas'*. In the following we will give a short outline of the approximations, but redirect the reader to the book[1] for a more in-depth view.
The derivation starts from Eq. (3.8) and neglects the vertex-corrections. The aforementioned self-energy is chosen to be $\Sigma = \frac{i}{2\tau}$, i.e. just a constant imaginary part describing a finite lifetime of the states. After analytical continuation, Eq. (3.12) is obtained which can be rewritten using frequency shifts and using the approximation $\sin(k) = k$ to yield

$$\sigma_\omega = \frac{1}{\pi}\int_{-\infty}^{+\infty} d\nu \frac{\eta_F(\nu) - \eta_F(\nu+\omega)}{\omega} \sum_{\mathbf{k}} k_i^2 G_\nu^{A,\mathbf{k}} G_{\nu+\omega}^{R,\mathbf{k}}. \tag{3.30}$$

Eq. (3.30) can be further simplified, by assuming the k-grid is sufficiently dense, so that $\frac{1}{N}\sum_{\mathbf{k}} \to \frac{1}{(2\pi)^d}\int d\mathbf{k}$ is justified. This integral can then be changed into an integral over the dispersion relation $\epsilon_{\mathbf{k}}$, assuming that $f(\epsilon_{\mathbf{k}})$ is only a function of the dispersion relations $\epsilon_{\mathbf{k}}$ and does not explicitly depend on the momenta k_x, k_y, k_z,

$$\int dk\, f(\epsilon_{\mathbf{k}}) = \int d\epsilon\, \mathcal{N}(\epsilon) f(\epsilon), \tag{3.31}$$

where $\mathcal{N}(\epsilon)$ is the density of states (DOS) of the system and $f(\epsilon)$ is any function. With Eq. (3.31) we can write

$$\sum_{\mathbf{k}} k_i^2 G_\nu^{A,\mathbf{k}} G_{\nu+\omega}^{R,\mathbf{k}} = \int d\epsilon (\epsilon+\mu)\mathcal{N}(\epsilon) G_\nu^{A,\epsilon} G_{\nu+\omega}^{R,\epsilon}. \tag{3.32}$$

Here, μ has been absorbed into ϵ. Eq. (3.32) can be evaluated under the following assumptions:

1. The Green's function $G_\nu^{\mathrm{R/A},\epsilon} = \frac{1}{\nu - \epsilon \pm \frac{i}{2\tau}}$ is strongly peaked around ϵ, i.e. $\tau^{-1} \ll \mu$. Hence, $(\epsilon+\mu) \simeq \mu$ and the energy variation of $\mathcal{N}(\epsilon)$ on the effective interval is negligible. Thus $\mathcal{N}(\epsilon)$ can be approximated by $\mathcal{N}(\epsilon) \simeq \mathcal{N}(\epsilon = \mu)$.
2. At low temperatures $\eta_F(\nu) - \eta_F(\nu+\omega)$ will be very compact. Since $G = \frac{1}{\nu - \epsilon + \frac{i}{2\tau}}$ and the ν integration has an effective compact support, ν can be absorbed into ϵ in Eq. (3.30) and the ν integration simplifies to $\int d\nu\, \frac{\eta_F(\nu) - \eta_F(\nu+\omega)}{\omega} \simeq 1$.
3. For completeness we also state the approximation $\sin(k) \simeq k$ that has been used before and yields the factor k_i^2.

Using the approximations listed above, Eq. (3.30) can be evaluated and yields the known Drude conductivity in Eq. (3.29).

One practical application of this result is the ability to benchmark codes for low temperatures. The τ in the Drude peak of the conductivity has to be (almost) identical to the τ used as a constant imaginary part of the self energy.
In the following chapter we will discuss the used one-frequency vertices and self-energies and why we believe those approximations to be justified. Chapter 5 will then use the methods developed in this chapter to obtain the optical conductivity for strongly correlated metals.

4. Simplified vertices for vertex corrections

In Section 3.3.2 analytical continuation has been performed using an effective one-frequency vertex function as in Eq. (3.18). This chapter will provide an overview and discussion of the used one-frequency vertices and Green's functions.

4.1. RPA-ladder

Since parquet DΓA calculations[12] indicate, that the major contribution stems from the $\overline{ph}$ channel it seems natural to test diagram classes in this channel. A simple, yet often used, approximation is the random phase approximation (RPA), which is the infinite sum of all ladder diagrams. Fig. 4.1 (top) depicts the corresponding diagrams and it is easy to see that those diagrams are two-particle reducible in the $\overline{ph}$ channel when compared to the definition in Fig. 2.3.

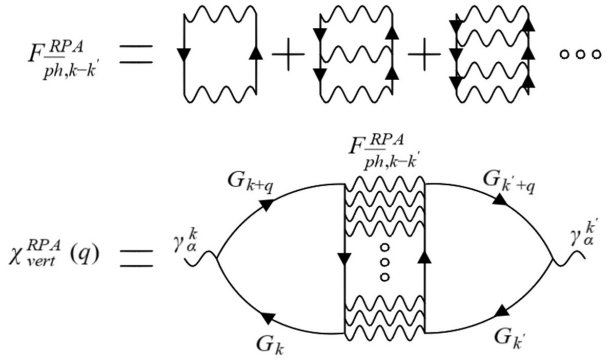

Figure 4.1.: (top) Series of Feynman diagrams that create the $\overline{ph}$-RPA ladder series. (bottom) Feynman diagram with the $\overline{ph}$-RPA ladder as effective one-frequency vertex.

The first order diagram of Fig. 4.1 is given by

$$F^{\mathrm{RPA},(1)}_{\overline{ph},k-k'} = U^2 \chi^0_{k-k'}, \tag{4.1}$$

where $\chi^0_{k-k'}$ is the bubble Eq. (4.2).

$$\chi^0_{k-k'} = -\frac{1}{\beta} \sum_{k_1} G_{k_1} G_{k_1+(k-k')} \tag{4.2}$$

Since each term after the first one just yields an additional $U\chi^0_{k-k'}$, the RPA series gives the well known geometric series which can be evaluated analytically:

$$F^{\mathrm{RPA}}_{\overline{ph},k-k'} \left(\widehat{=} U^2 \chi^{\mathrm{RPA}}_{\mathbf{q}} \right) = U^2 \chi^0_{k-k'} \sum_{n=0}^{\infty} \left(U\ \chi^0_{k-k'} \right)^n = \frac{U^2 \chi^0_{k-k'}}{1 - U\ \chi^0_{k-k'}}. \tag{4.3}$$

A typical example of the structure of the RPA-vertex function of Eq. (4.3) is displayed in Fig. 4.2(a/c). Fig. 4.2(b/d) displays the Ornstein-Zernike (OZ) correlation function (Eq. (4.4)) which will be introduced in the next section.

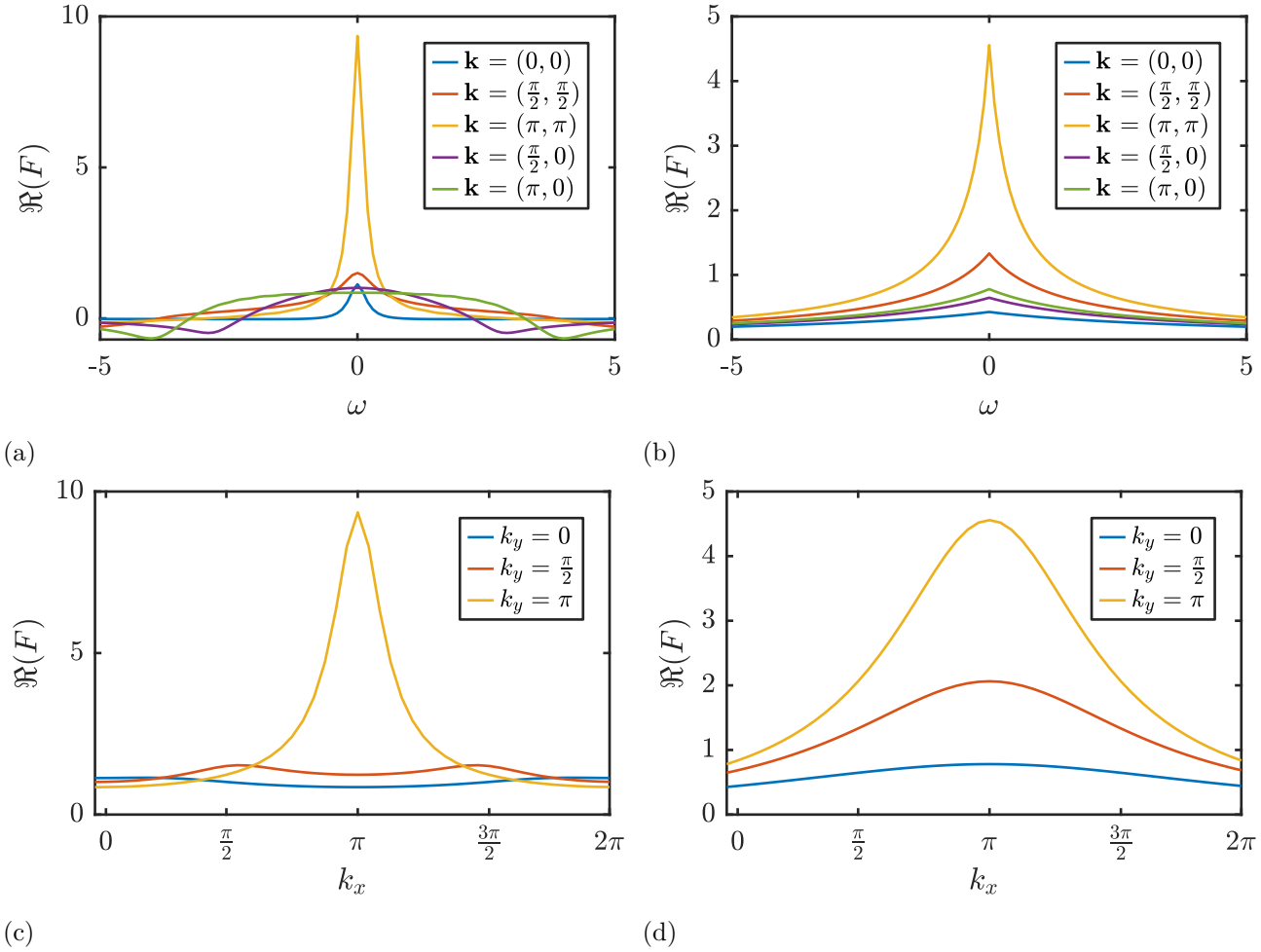

Figure 4.2.: RPA (Eq. (4.3)) and OZ vertex function (Eq. (4.4)). (a) RPA vertex for different k-points vs. ω. (b) OZ vertex for different k-points vs. ω. (c) RPA vertex for $\omega = 0$ different k_y vs. k_x. (d) OZ vertex for $\omega = 0$ different k_y vs. k_x.
Parameters: RPA-$\{T = 0.1,\ U = 1.8,\ \Delta = 0.18\}$; OZ- $\{T = 0.1,\ A = 9.3,\ \xi = 0.7,\ \lambda = 5,\ \Delta = 0.18\}$

4.2. Ornstein-Zernike correlation function

The Ornstein-Zernike function (OZ) in Eq. (4.4) is often used as a fit for the vertex function in order to extract a correlation length ξ[28]. In order for this correlation function to be valid, the material has to be isotropic and the anomalous critical exponent has to be close to zero. Furthermore, the function is constructed for q - points near (π, π), small ω and parameters for which the system is near the anti-ferromagnetic phase transition[29,30,31,32]. The OZ susceptibility reads:

$$F_q^{\mathrm{OZ}} \left(\widehat{=} U^2 \chi_{\mathbf{q}}^{\mathrm{OZ}} \right) = \frac{A}{\xi^{-2} + (\mathbf{q} - \pi)^2 + \lambda|\omega|}, \tag{4.4}$$

where A is a parameter which (linearly) scales the magnitude of the vertex corrections and ξ is the correlation length. The additional parameter λ affects the relative importance of ω compared to $\mathbf{q}$. A large λ can also be used in combination with a large A to suppress the $\mathbf{q}$ dependence. Eq. (4.4) is displayed in Fig. 4.2(b/d).

Since the Ornstein-Zernike function if mainly used to extract parameters, like the correlation length ξ a typical fit of the OZ to the RPA-ladder is shown in Fig. 4.3. The fitting procedure is first carried out for ξ and A, by fitting at $\omega = 0$. After ξ and A are determined, λ is extracted by fitting to the full ω-dependent vertex.

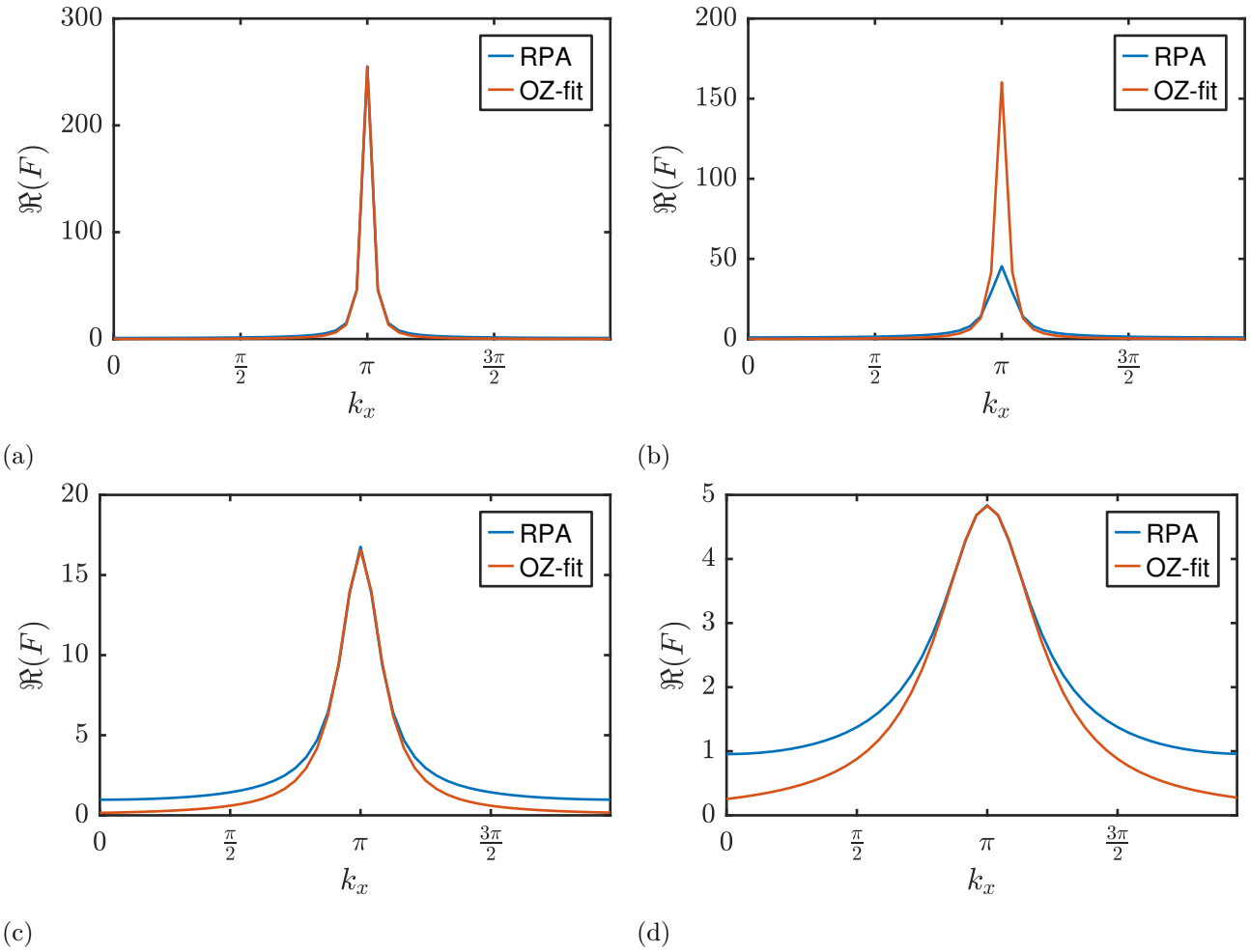

Figure 4.3.: Fit of the OZ to the RPA-ladder vertex. (a) $T = 0.0556$ and $k_y = \pi$ (b) $T = 0.0556$ and $k_y = \frac{25\pi}{24}$. (c) $T = 0.1$ and $k_y = \pi$. (d) $T = 0.2$ and $k_y = \pi$. Note that (a) is near the phase transition and hence the function is peaked around $\mathbf{k} = (\pi, \pi)$ and is fitted well by the OZ. For higher temperatures like in (d), further away from the phase transition, larger deviations can be observed. Also note that (b) is away from (π, π) and thus larger deviations can be observed.
Parameters: $U = 1.9$, $\Delta_{\text{one-particle}} = 0.16$

Fig. 4.3(a) shows, that near the phase-transition, which is between $0.05 < T < 0.0556$ for $\Delta_{\text{one-particle}} = c + a\,T^2$; $\{c = 1.6368, a = 0.1547\}$, the OZ agrees very good with the RPA-ladder for $\mathbf{k} = (\pi, \pi)$. For k-points deviating from (π, π) quite substantial deviations can be observed Fig. 4.3(b), here the example is for $k_y = \frac{25\pi}{24}$.

4.3. Green's function of the disordered electron gas

The simplest form of a self-energy is given by a constant imaginary part $\Sigma^{\mathrm{R}}(\omega, \mathbf{k}) = i\Delta$, where Δ corresponds to the broadening of the spectral function, or the inverse lifetime and thus encodes a finite lifetime of the states. Using this simple self energy the retarded (advanced) Green's function is of the form,

$$G_\nu^{\mathrm{R/A},\mathbf{k}} = \frac{1}{\nu - \epsilon_{\mathbf{k}} \pm i\Delta}. \tag{4.5}$$

Such a typical form of the self-energy can for example be obtained via an approximation for the so-called disordered electron gas, which describes quasi-free electrons scattering at static impurities. For a detailed derivation and display of made assumptions see chapter 6.5 from Ref. 1. The spectral function corresponding to Eq. (4.5) is given by a lorentzian,

$$A_\nu^{\mathbf{k}} = \frac{1}{\pi} \frac{\Delta}{(\nu - \epsilon_{\mathbf{k}})^2 + \Delta^2}, \tag{4.6}$$

where Δ is simply the width of the curve, which denotes the inverse life-time. Eq. (4.6) is graphically visualized in Fig. 4.4 (dashed yellow).

4.4. DΓA self-energy

Although, Eq. (4.5) provides a useful basic tool to understand the characteristics of π-tons, the corresponding spectral function $A(\omega)$ of the 2D square lattice tight-binding model is quite featureless. In order to truly understand the importance of $\overline{ph}$ ladder diagrams, we also used the self-energy obtained by the DΓA[33] calculations in Ref. 12. Thus we can separate the contributions of the $\overline{ph}$ diagrams from all other diagrams and study their characteristics. However, the DΓA self energy is given in Matsubara frequencies. Hence numerical analytical continuation has to be performed. This was done using the python library *ana-cont*[34,35]. However, as the self-energy from Ref. 12 is only known on a 6x6 k-grid, but we know the analytic expression of the dispersion relation, we use the commonly used practice of coarse graining[36]. This procedure simple interpolates the self-energy, for which we used nearest-neighbour interpolation as Ref. 12, which allows for more direct comparison of the results. The spectral function for this DΓA self-energy is displayed in Fig. 4.4 (solid lines).

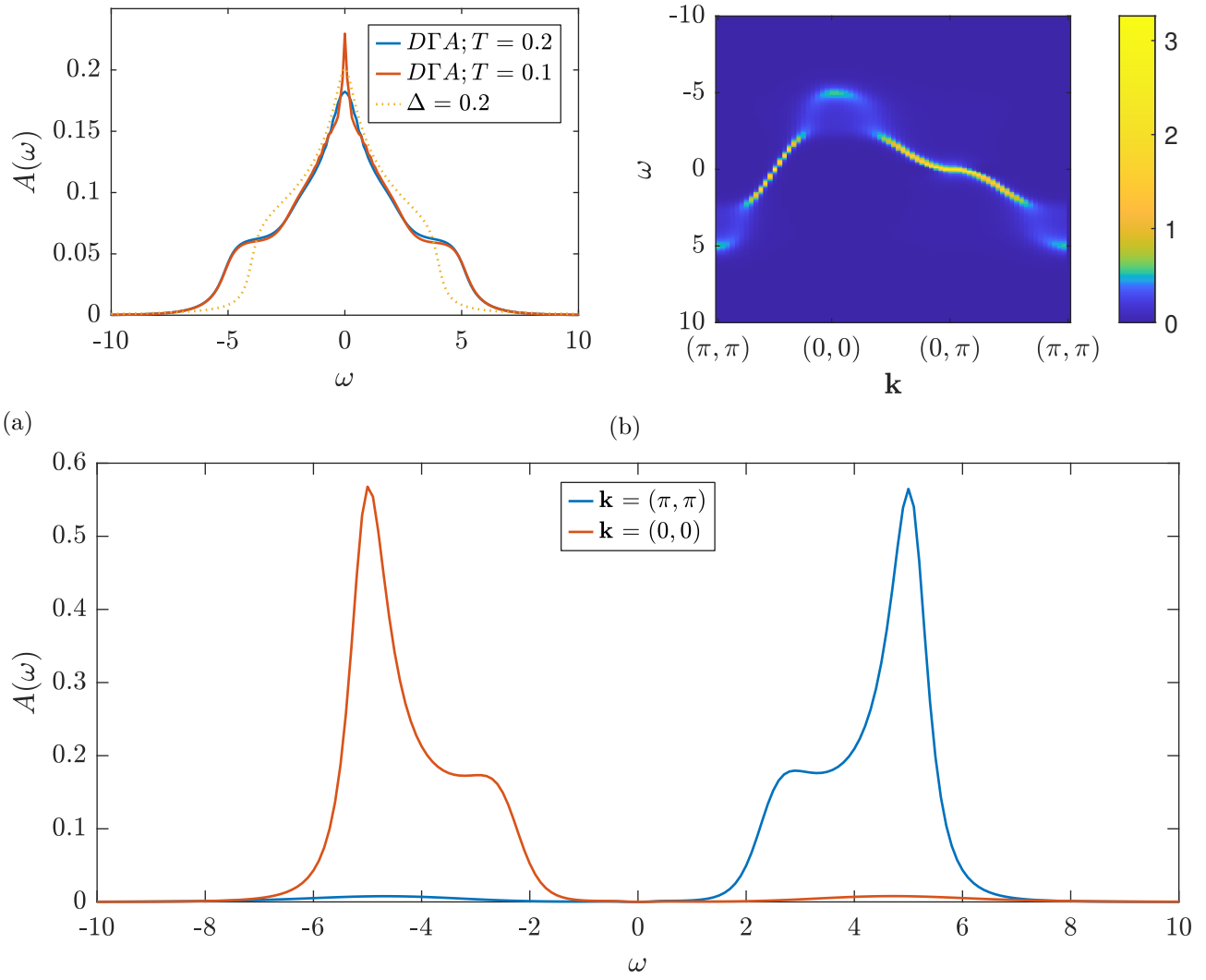

Figure 4.4.: (a) Spectral function. DΓA self-energy at $T = 0.2$ as input (blue), DΓA self-energy at $T = 0.1$ as input (red) and $\Sigma = i\Delta$; $\Delta = 0.2$) at $T = 0.1$ (dotted orange). All spectral functions are for the square lattice Hubbard model at $U = 4$. (b) Spectral function $\mathbf{k}$ resolved along a path in the Brillouin zone for $D\Gamma A$ self energy and $T = 0.1$. (c) $A(\omega, \mathbf{k})$ for $\mathbf{k} = (\pi, \pi)$(blue) and $\mathbf{k} = (0, 0)$ (red) for $T = 0.1$. In (a) Hubbard bands are clearly visible around $\omega \simeq 4$ for DΓA.

5. Characteristics of $\overline{ph}$ vertex corrections for strongly correlated materials

In this section we present the results using Eq. (3.12) and Eq. (3.18) in order to describe vertex corrections to the optical conductivity in a real-frequency formalism. Implementation of the code is in the programming language C. Vector-matrix operations are performed using the intel MKL library. This chapter is organised as follows: in section Section 5.1 the general characteristics of the vertex corrections are displayed, as well as their dependence on interaction strength U and inverse temperature β. Section 5.2 treats the same dependencies for the parameters of the Ornstein-Zernike correlation function namely A, ξ and λ. In Section 5.3 characteristics of the vertex corrections from RPA are compared to DΓA. This has been done using the same self-energy in RPA as for DΓA and thus we can separate the exact contribution from the ladder diagrams from all other vertex corrections. At this point we also want to note that all numeric values for parameters are given in units of the hopping parameter t, which is set to $t \equiv 1$.

5.1. Characteristics and parameter dependence of vertex corrections using the RPA-ladder

We first study the parameter dependence of the optical conductivity using a Green's function with a simple broadening Eq. (4.5) and an RPA-ladder as effective vertex Eq. (4.3). This allows us to get an intuition of how $\sigma(\omega)$ behaves. Fig. 5.1 and Fig. 5.2 depicts the full OC $\sigma(\omega)$, the part from the bubble only $\sigma_0(\omega)$ and the part from the vertex corrections $\sigma_{\text{vert}}(\omega)$ for a range of U and β using a temperature dependent scattering rate ($\Delta = c + aT^2; \{c = 1.6368, a = 0.1547\}$). This scattering rate has been obtained via fitting a Drude peak (Eq. (3.29)) to $\sigma_0(\omega)$ from Ref. 12. In Fig. 5.1(a) one can notice that the peak structure of the OC is indeed very close to a Drude peak as predicted in chapter Section 3.5. Fig. 5.1(b) shows a rather interesting temperature dependence of the vertex corrections. At low frequencies they are increasing for temperature up to $T \sim 0.17$, they decrease again afterwards. This is even more evident in Fig. 5.3 and Fig. 5.5 when extracting the Drude broadening. Dependence on U in Fig. 5.2 is rather straight forward, as is expected since the RPA-ladder scales roughly with U^2.

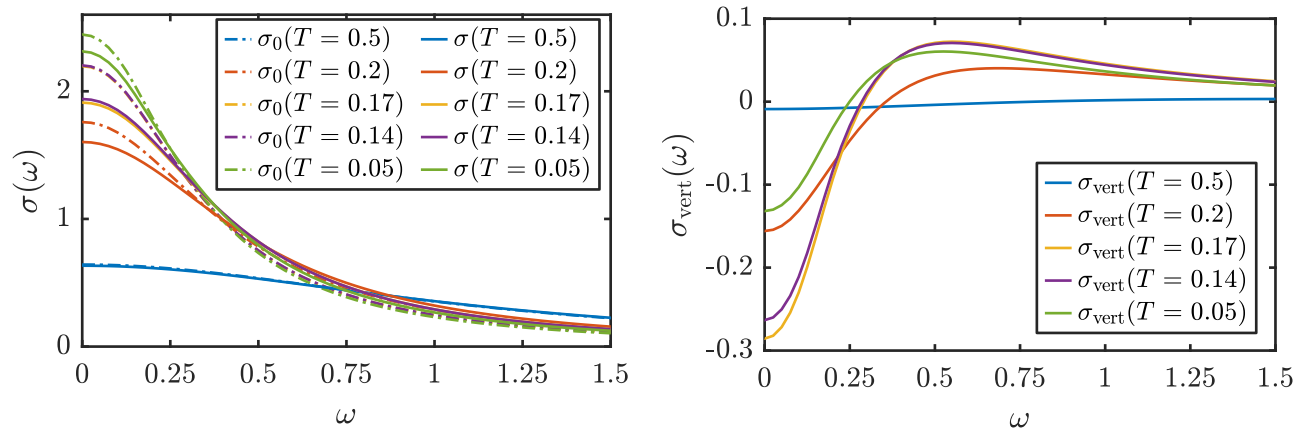

(a) (b)

Figure 5.1.: (a) Optical conductivity with and without vertex corrections. $\sigma(\omega)$ and $\sigma_0(\omega)$, as a function of ω for a selected range of T. (b) Vertex contribution to the optical conductivity $\sigma_{\text{vert}}(\omega)$ as a function of ω for a selected range of T. Note how in (b) at the low frequencies the vertex corrections decrease again for low T.
Parameters: $U = 1.8$ and $\Delta = c + aT^2; \{c = 1.6368, a = 0.1547\}$ for both plots.

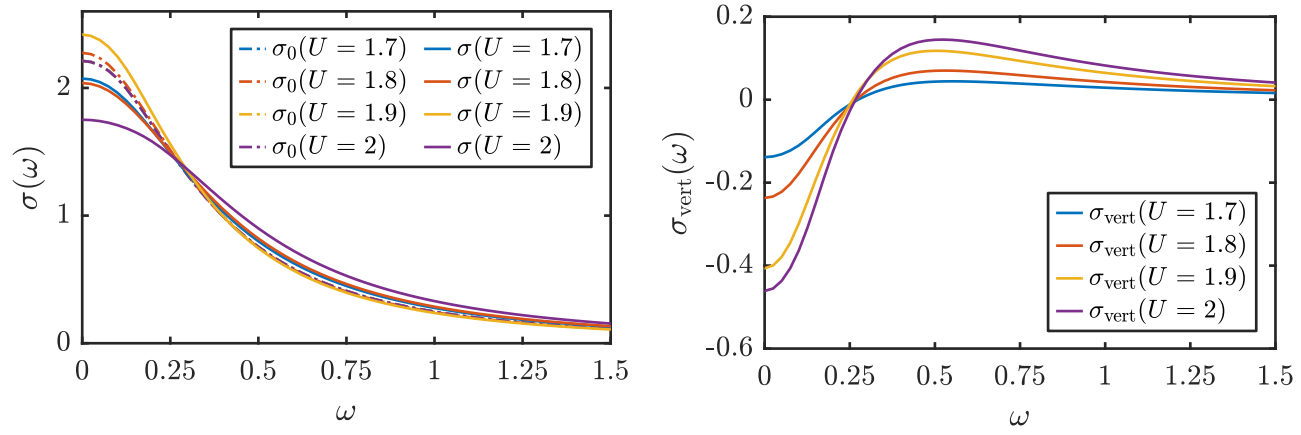

(a) (b)

Figure 5.2.: (a) $\sigma(\omega)$ and $\sigma_0(\omega)$ as a function of ω for a selected range of U. (b) $\sigma_{\text{vert}}(\omega)$ as a function of ω for a selected range of U.
Parameters: $T = 0.1$ and $\Delta = 0.18$ for both plots.

The characteristic of the vertex corrections in Fig. 5.1(b) and Fig. 5.2(b) can simply be understood as a suppression of the OC at low frequencies and an enhancement at higher frequencies. This effectively behaves like an additional artificial broadening and surprisingly does not change the Drude characteristic of the peak. Hence, $\sigma(\omega)$ and $\sigma_0(\omega)$, the former with an additional artificial broadening ,seem to be almost indistinguishable. To measure the "strength" of the vertex correction we therefore use two features. First the width $\Delta_{\text{Drude}} = \frac{1}{2\tau}$ of a Drude-fit (Eq. (3.29)), which is identical to the one one-particle scattering rate $\Delta_{\text{one-particle}}$ for the bubble, but differs when vertex corrections are present. Second, we use the magnitude of $\sigma_{\text{vert}}(\omega = 0)$. Δ_{Drude} is displayed in Fig. 5.3 as a function of T^2 and in Fig. 5.4 as a function of $\Delta_{\text{one-particle}}$ (which itself is also just a function of T^2).

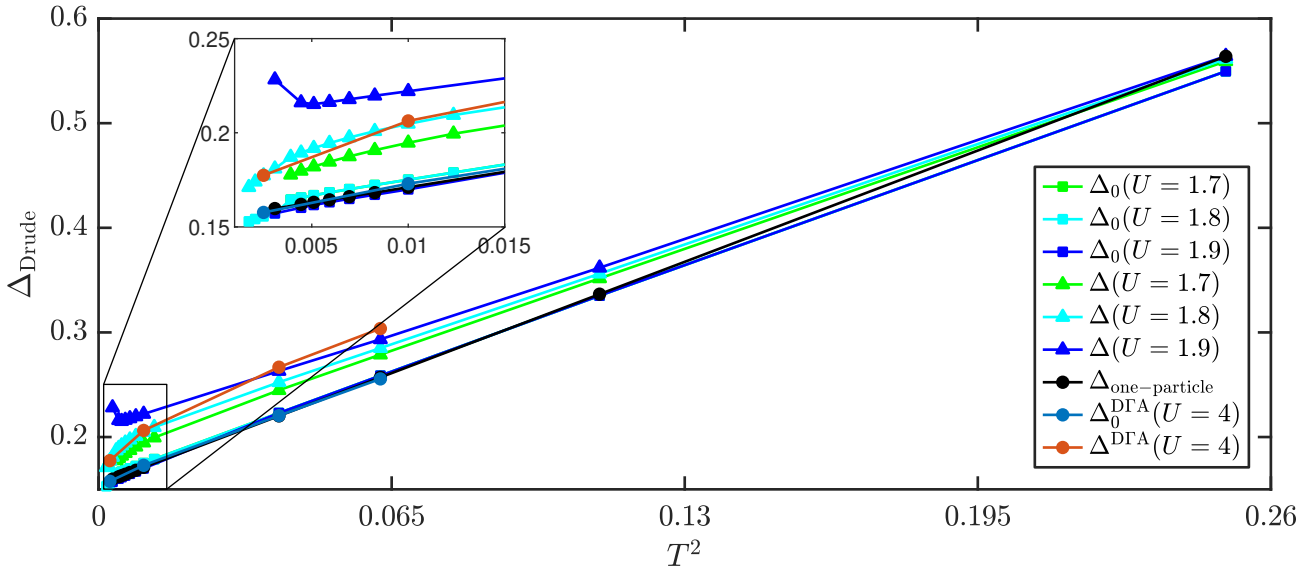

Figure 5.3.: Width of the Drude peak Δ_{Drude} vs. T^2. Note that for the bubble contribution Δ_0 is almost identical to $\Delta_{\text{one-particle}}$. When vertex corrections are added (Δ), a temperature dependent additional broadening appears. Note the qualitative difference between $U = 1.9$, which has an anti-ferromagnetic phase transition at low temperatures and $U = 1.8$, for which this phase transition does not exist. The bubble and vertex corrected broadening of DΓA are denoted by $\Delta_0^{\text{D}\Gamma\text{A}}$ and $\Delta^{\text{D}\Gamma\text{A}}$, respectively.

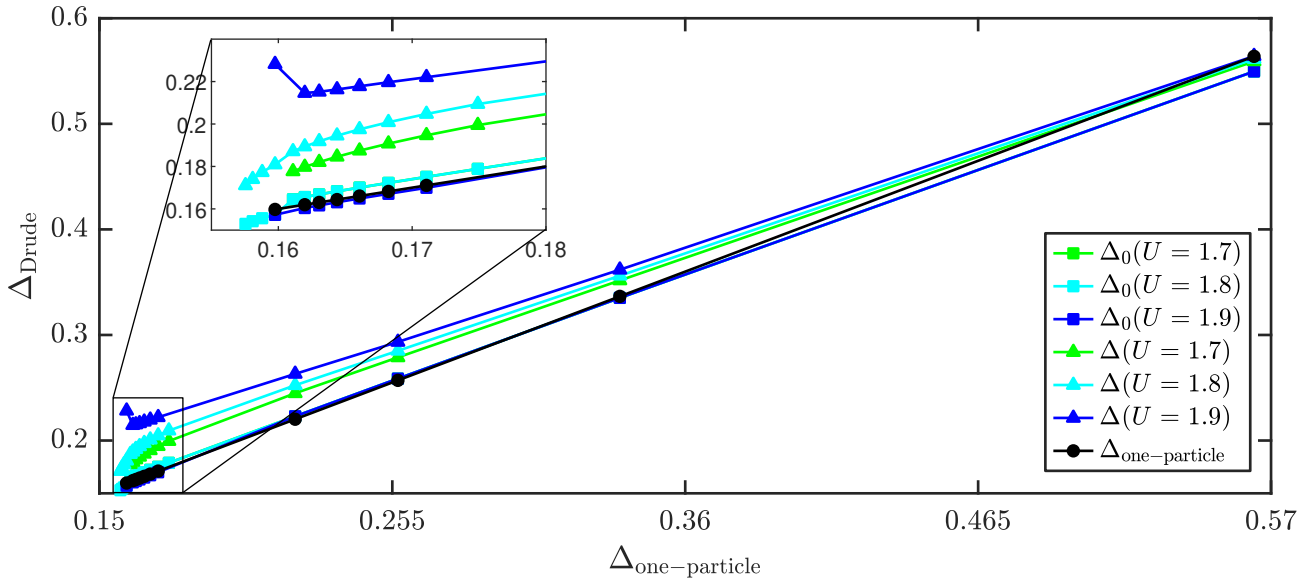

Figure 5.4.: Width of the Drude peak Δ_{Drude} vs. $\Delta_{\text{one-particle}}$. Note that for the bubble contribution Δ_0 is almost identical to $\Delta_{\text{one-particle}}$. When vertex corrections are added (Δ), a temperature dependent additional broadening appears. Note again the qualitative difference between $U = 1.9$, which has an anti-ferromagnetic phase transition at low temperatures and $U = 1.8$, for which this phase transition does not exist.

One can clearly see, that for the bubble contribution, Δ_{Drude} is nearly identical to $\Delta_{\text{one-particle}}$, which was shown in chapter Section 3.5 to hold for $\Delta_{\text{one-particle}} \to 0$ and also served as a benchmark for the code. When adding vertex corrections however, an additional temperature dependent broadening

appears. The contribution from the vertex corrections is almost 0 at high temperature which is expected. However, at very low temperatures ($T < 0.01$) and moderate $U = (1.7, 1.8)$ a decrease can be observed. Note how this behaviour is also present in the DΓA calculations. However, for $U = 1.9$ a totally different behaviour can be observed. Not only do the vertex corrections remain strong at very low temperatures, they even increase and hint at a divergence. Indeed for $U = 1.9$ the Stoner criterion $(1 - U\chi_0\ )$ for the anti-ferromagnetic phase transition of the RPA-ladder is met at a temperature between $0.05 < T < 0.0556$. We also show in Section 5.2, that for $U = 1.9$ the correlation length diverges roughly with T^{-2} near the anti-ferromagnetic phase transition. However, at this point it should be mentioned, that the anti-ferromagnetic phase transition (at least at finite temperatures) is due to the mean-field character of the RPA.

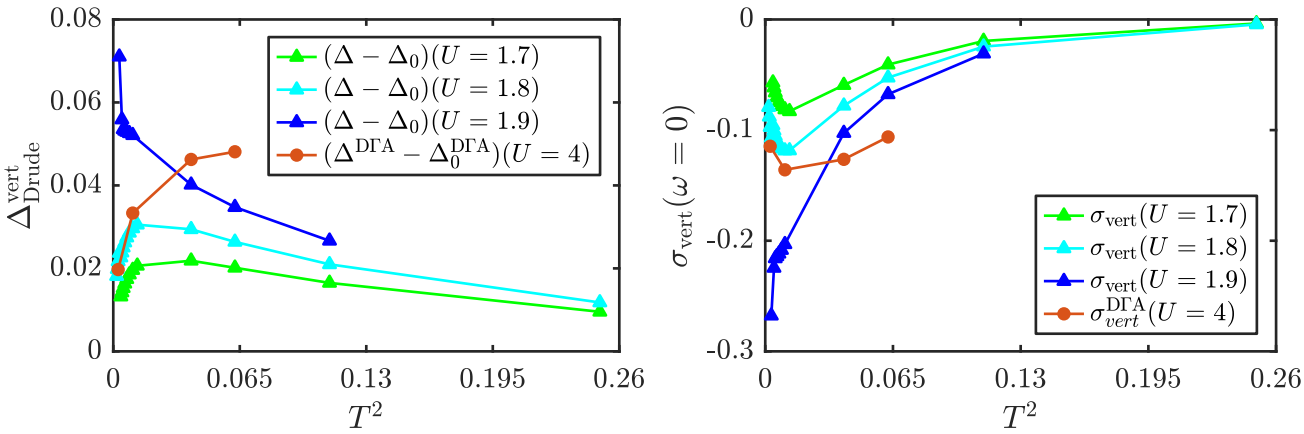

(a) (b)

Figure 5.5.: (a) Additional broadening of $\sigma(\omega)$ due to vertex corrections. (b) Vertex corrections at $\omega = 0$, $\sigma_{\text{vert}}(\omega = 0)$, i.e. the suppression of the DC conductivity. Both features share the same tendencies. Note also the qualitative agreement of the RPA-ladder ($U = 1.8$) with the DΓA calculations. $U = 1.9$, which has an anti-ferromagnetic phase transition at low temperatures, however displays a completely different behaviour.

When going to low temperatures two effects concerning the vertex corrections compete. One is indirect, as $\Delta_{\text{one-particle}}$ decreases as temperature decreases, which causes the vertex F to be more sharply peaked, see Fig. 5.6(d). All other things kept constant this increases the additional broadening created by the vertex corrections, as displayed in Fig. 5.6(b). By contrast, when keeping $\Delta_{\text{one-particle}}$ fixed, the additional broadening of the vertex corrections decreases rapidly towards low temperatures, see Fig. 5.6(a). This however cannot be linked to F directly, as its behaviour in Fig. 5.6(c) mirrors that in Fig. 5.6(d), whereas the behaviour of the broadening in Fig. 5.6(a) has the opposite trend of Fig. 5.6(b). As external Green's functions (in real frequency formulation, as in Eq. (3.19)), are not temperature dependent for a fixed $\Delta_{\text{one-particle}}$ themselves, the only other temperature dependence originates from the Fermi/Bose function. These factors effectively decide on which frequency part the Green's functions contribute.

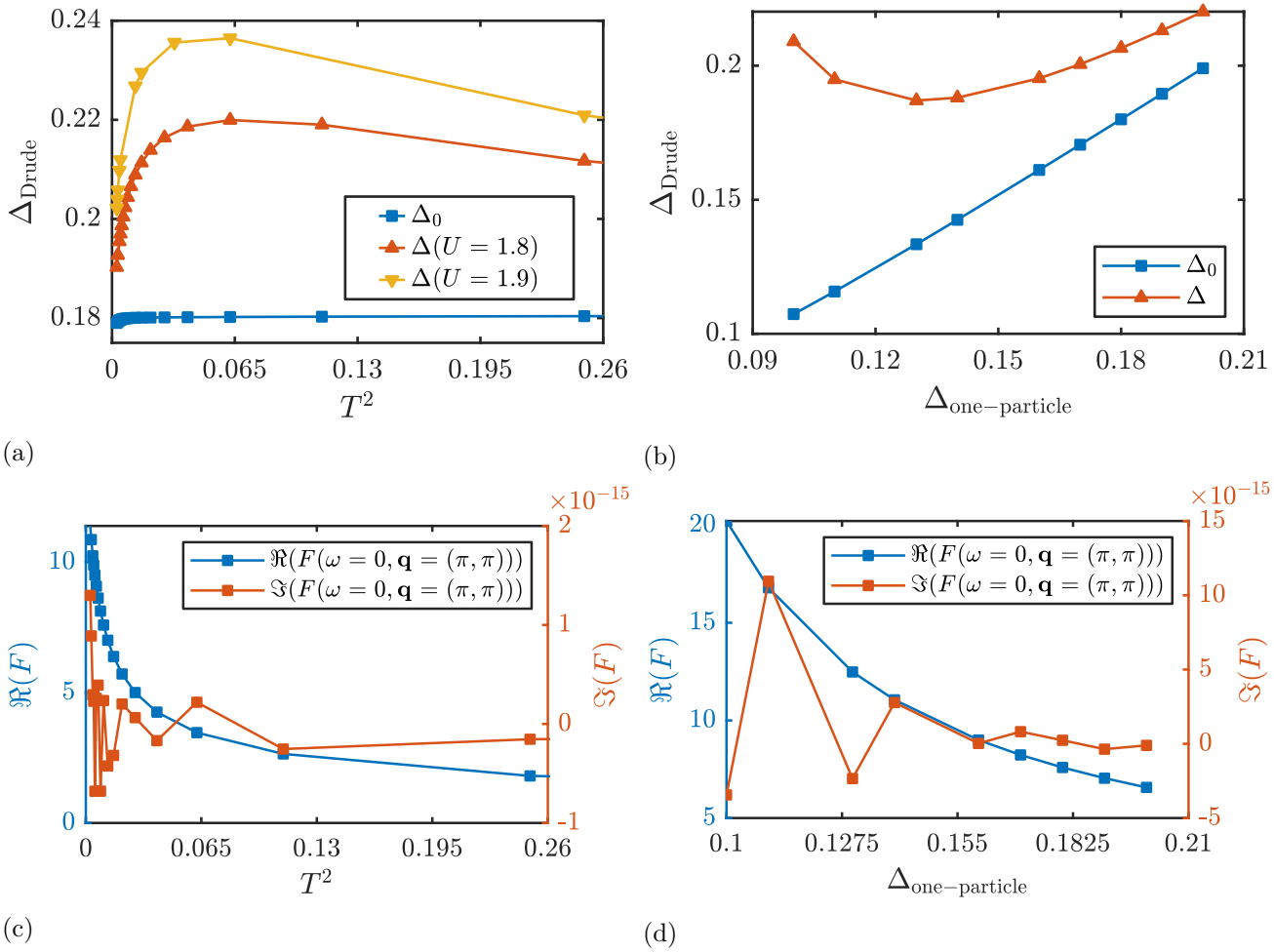

Figure 5.6.: (a) Δ_{Drude} vs. T^2 for a fixed $\Delta_{\text{one-particle}} = 0.18$. (b) Δ_{Drude} vs. $\Delta_{\text{one-particle}}$ for constant temperature ($T = 0.1$). (c) F_{RPA} vs. T^2 at $\omega = 0$ and $\mathbf{q} = (\pi, \pi)$. (d) F_{RPA} vs. $\Delta_{\text{one-particle}}$ at $\omega = 0$ and $\mathbf{q} = (\pi, \pi)$. Note the different scale for the imaginary part (red). If not explicitly noted otherwise we use $U = 1.8$.

5.2. Parameter dependence of vertex corrections using the Ornstein-Zernike correlation function

In the previous chapter we studied the basic parameter dependencies of an $\overline{ph}$ RPA-ladder to the vertex corrections of the optical conductivity. To understand the behaviour close to the anti-ferromagnetic phase-transition we fitted an Ornstein-Zernike correlation function (Eq. (4.4)) to the RPA vertex. We can next study the dependence of A, ξ and λ on β and U. The merit of this procedure is a much easier interpretation of the OZ parameters as exact dependencies are known. Fig. 5.7 displays all three parameters of the OZ as a function of β (a,b,d) and ξ also as a function of U (b). Since it is known that ξ has to diverge proportional to T^{-2} near the phase transition for an RPA-ladder, we can conclude that for $U = 1.9$ we are already quite near a phase transition, in contrast to $U = 1.8$. $U = 2$ is already past the phase transition for low T and has thus not been used. Fig. 5.7(c,d) show a large increase of both A and λ at high temperatures. This effectively suppresses the $\mathbf{q}$ dependence of the OZ function, which is to be expected since the RPA will become flat at higher temperatures. Note that in Fig. 5.7(a) ξ is shown as a function $\beta = T^{-1}$ to better emphasise the difference between $U = 1.9$ and $U = 1.8$.

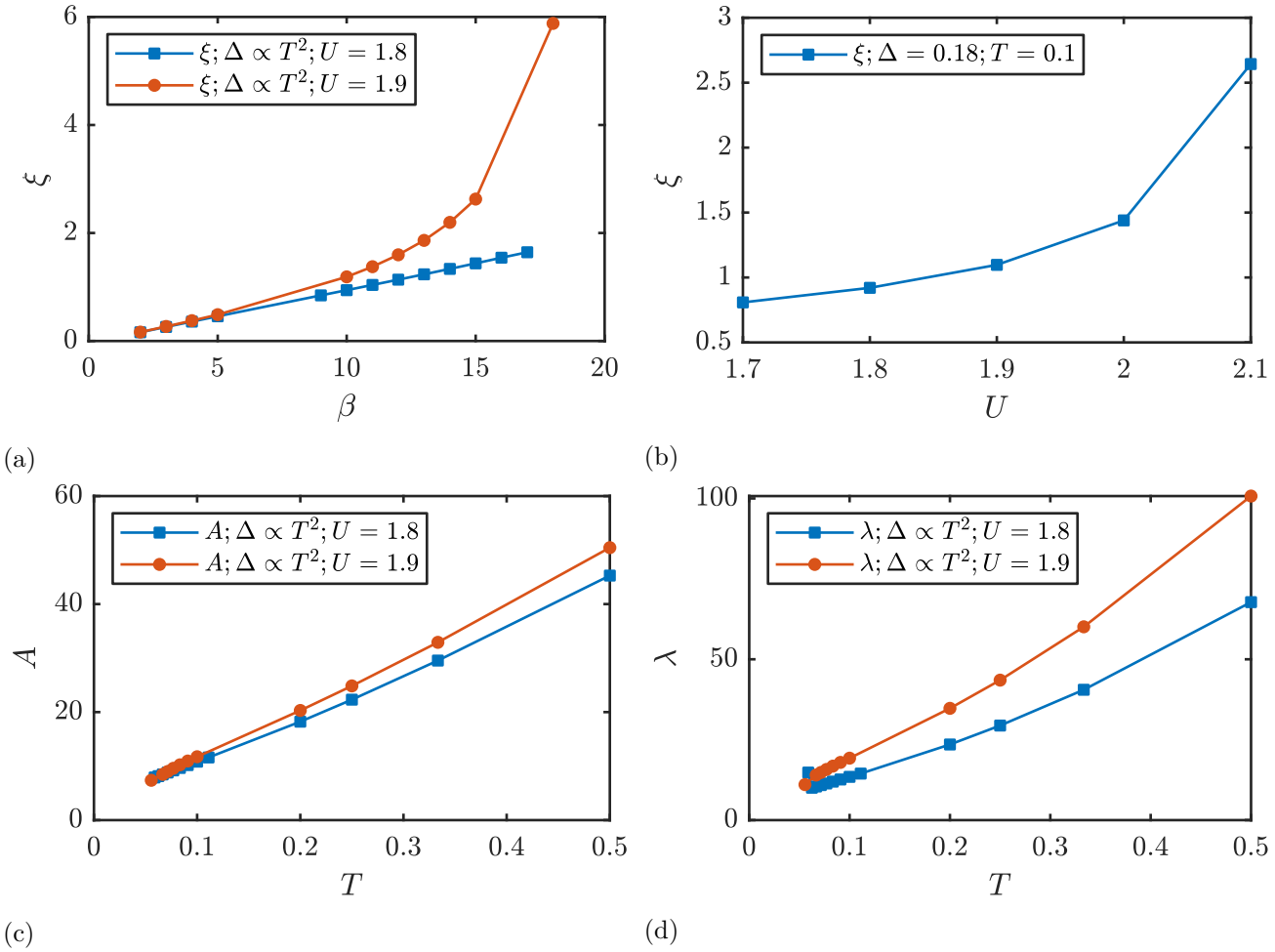

Figure 5.7.: Dependence of the OZ parameter when fitted to an RPA-ladder. (a) ξ vs. β. (b) ξ va. U. (c) A vs. T. (d) λ vs. T. For all plots $\Delta_{\text{one-particle}} = c + aT^2; \{c = 1.6368, a = 0.1547\}$.

We also investigated the vertex corrections, when using an OZ function directly as vertex. Even tough the OZ function is rather featureless (Fig. 4.2) the vertex corrections in Fig. 5.8 show very similar characteristics as for the RPA-ladder with constant self energy in Figs. 5.1 and 5.2. Fig. 5.8(a) shows the strong dependence of the vertex corrections with the correlation length ξ which is expected. The parameter λ however appears to have little impact if all other parameters are kept constant Fig. 5.8(b).

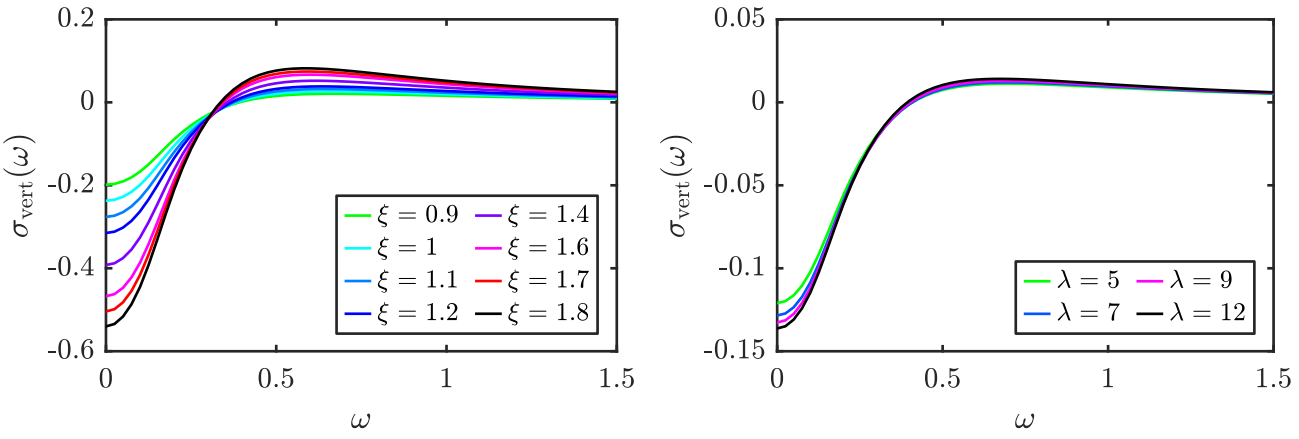

(a) (b)

Figure 5.8.: Structure of the vertex corrections to the optical conductivity $\sigma(\omega)$ using an Ornstein-Zernike correlation function as effective vertex. (a) $\sigma_{\text{vert}}(\omega)$ for a range of correlation lengths ξ at $\lambda = 5.7$. (b) $\sigma_{\text{vert}}(\omega)$ for a range of λ at $\xi = 0.7$. For both plots $T = 0.1$, $A = 9.3$ and $\Delta_{\text{one-particle}} = 0.18$

The parameter dependence observed in Fig. 5.8 is mirrored in the additional broadening of the Drude peak, which is displayed in Fig. 5.9. We can observe a linear rise of Δ_{Drude} with ξ^2, which is expected from the form of the OZ function (Eq. (4.4)).

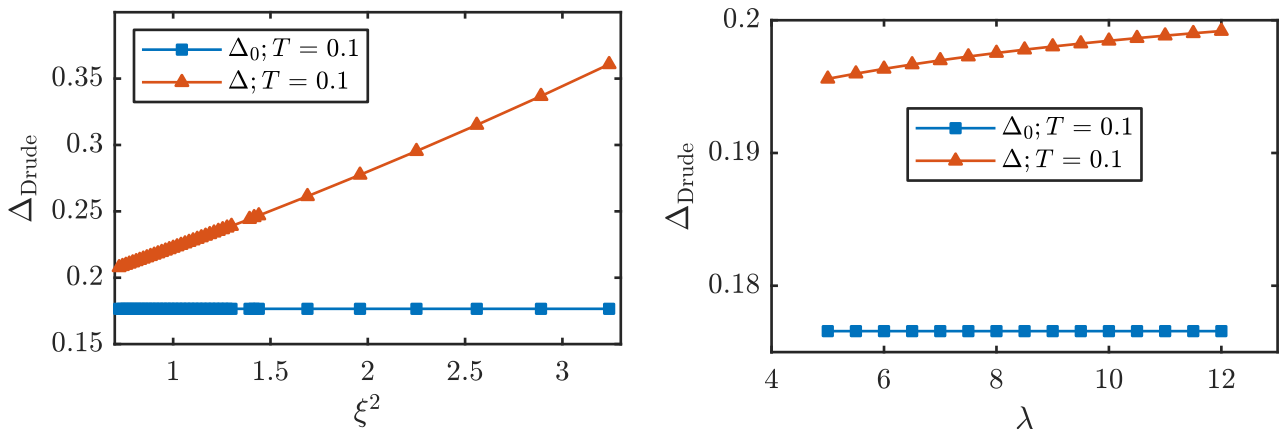

(a) (b)

Figure 5.9.: Width of the Drude peak Δ_{Drude} for the bubble contribution Δ_0 and the full optical conductivity Δ as a function of (a) ξ^2 and (b) λ. In both plots $T = 0.1$, $A = 9.3$ and $\Delta_{\text{one-particle}} = 0.18$

5.3. Direct comparison of RPA-ladder and DΓA

Up until now we studied effective characteristics, like the additional Drude peak broadening from the vertex corrections. In this section we will determine which part of the $\overline{ph}$ vertex corrections of the DΓA calculations can be understood in terms of a simple RPA-ladder. To this end we use a constant self-energy (which is extracted from the DΓA data via fitting a Drude peak to σ_{bub}) on the one hand and the self-energy directly from the DΓA calculations on the other hand. Via choosing a self energy

for a given temperature leaves the interaction strength U as only free parameter left in our calculations. The presented DΓA results all were obtained for $U = 4$, which is however not applicable for our RPA-ladder. This stems from neglecting screening in case of the RPA-ladder, which would already be past the antiferromagnetic phase-transition for for such interaction strengths. We thus always show the RPA vertex corrections for three different values of U.

Constant self-energy

Fig. 5.10 (a) displays the bubble contribution to the optical conductivity σ_{bub}, and Fig. 5.10 (b) to the current-current correlator $\Im(\chi_{\text{bub}})$ for $T = 0.1$, both for DΓA and RPA approaches. While the low-frequency regime is rather similar, the additional structure from the Hubbard-bands (Fig. 4.4) is absent for the RPA with $\Sigma = i\Delta_{\text{one-particle}}$. The one-particle broadening Δ for the RPA has been obtained via fitting a Drude peak to the DΓA data. Vertex corrections are displayed in Fig. 5.11.

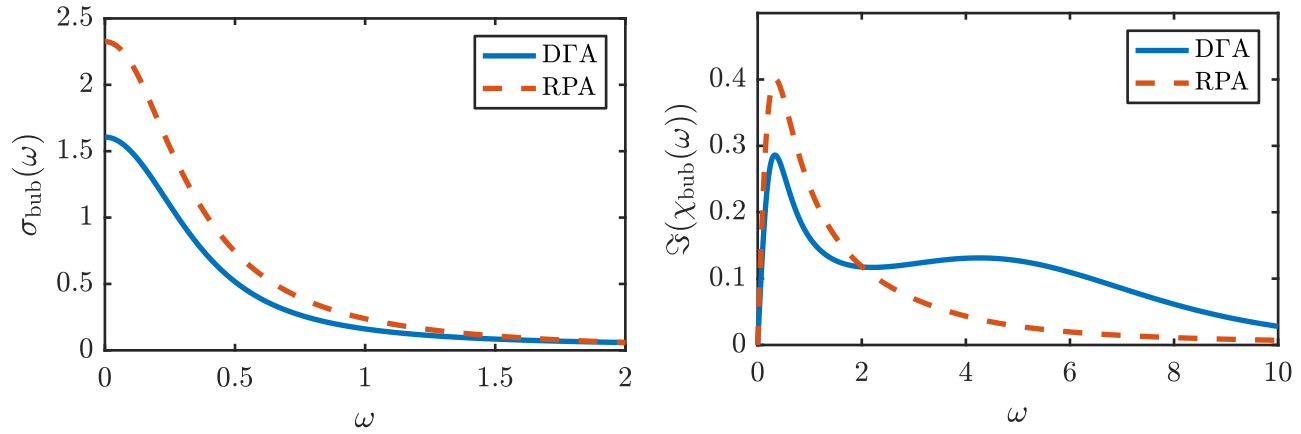

(a) (b)

Figure 5.10.: Bubble contribution to the optical conductivity σ_{bub} (a) and to the current-current correlator $\Im(\chi_{\text{bub}})$ (b) at $T = 0.1$ and $U = 4$. For the RPA $\Sigma = i\Delta$ and we set $\Delta_{\text{one-particle}} = 0.17$.

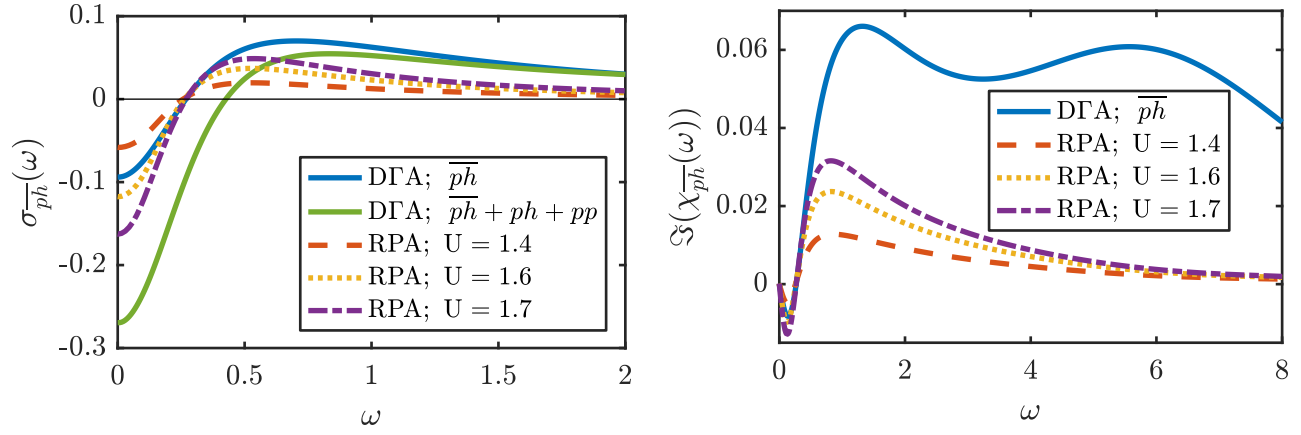

(a) (b)

Figure 5.11.: Vertex corrections (a) to the optical conductivity $\sigma_{\overline{ph}}$ and (b) the current-current correlator $\Im(\chi_{\overline{ph}})$ at $T = 0.1$. For the RPA $\Sigma = i\Delta$ and we set $\Delta_{\text{one-particle}} = 0.17$. The DΓA calculations were at $U = 4$.

Even tough for RPA and DΓA the characteristics of the vertex corrects are similar and comparable

in the low-frequency regime, this is not true for the high-frequency regime. A result, which is not surprising, since the high-frequency structure is missing in the constant self-energy and consequently in the spectral function. One peculiar feature is the vanishing of the $\overline{ph}$ vertex corrections for $\omega \simeq 0.28$, which is commonly referred to as isobestic points[37]. Not only is this feature for RPA independent of U, as already shown in Fig. 5.2, or ξ in the case of using an OZ correlation function (Fig. 5.8), it is also present for the full DΓA $\overline{ph}$ vertex correction. Only when adding contributions from the pp and ph channel, a finite value for $\sigma_{\text{vert}}(\omega \simeq 0.28)$ is observed. This independence of the vertex function suggests, that the external legs for the vertex corrections in Fig. 4.1 are responsible for this behaviour. One should expect, however, that a spectral-function which is vastly different from the tight-binding one in as in Fig. 4.4 (the DΓA self-energy only adds the comparatively high-frequency Hubbard-bands) will change this behaviour.

Self-energy from DΓA

In this section we will use the self-energy from the DΓA calculations, thus constructing the RPA-ladder with the same Green's functions as in DΓA. This enables us to separate the RPA-ladder diagrams from all other ones in the $\overline{ph}$ channel, which are computed in DΓA. Fig. 5.12 displays σ_{bub} from the real-frequency code with the same self-energy as Ref. 12. One can clearly see the similarity of the results from both codes, however σ_{bub} should be identical as the bubble diagram is the same. The discrepancy is mainly due to the error and smearing out from MaxEnt analytic continuation. This also concerns the real-frequency code, as the self-energy in DΓA calculations is in Matsubara frequencies and has thus first to be analytically continued to real frequencies. In contrast, in this work we have analytically continued the self-energy and consequent calculations were performed directly in real frequencies. The stability of the results with respect to the allowed error for the MaxEnt routine is discussed in detail in Appendix A.6.

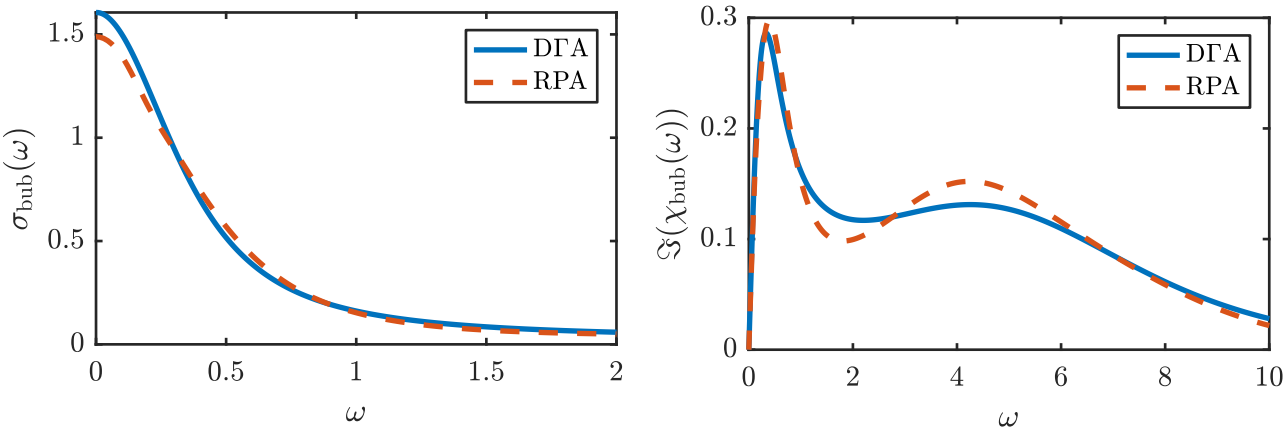

(a) (b)

Figure 5.12.: Bubble contribution to the optical conductivity σ_{bub} (a) and to the current-current correlator $\Im(\chi_{\text{bub}})$ (b) at $T = 0.1$ and $U = 4$. For the RPA-ladder the same self-energy as for DΓA has been used (Fig. A.2). Since RPA and DΓA only use different approximations for the vertex function, but not for the bubble, any difference has to be due to numerical insufficiencies. Most of the discrepancy stems from the MaxEnt routine, which tends to smear out features as discussed in detail in Appendix A.6.

Fig. 5.13 shows the RPA-ladder contribution to the vertex corrections, which did not change much compared to using only a constant imaginary part for the self-energy as in Fig. 5.11 at a temperature $T = 0.1$. Two small differences can be noticed: first, a small frequency component compared to $\Sigma = i\Delta$

appears, which is still much smaller than for the $\overline{ph}$ contributions of parquet DΓA. Second, to generate the same magnitude for the vertex corrections a higher interaction strength U has to be used. This is also expected since screening is now included in the self-energy. The same quantities are displayed in Fig. 5.14 for $T = 0.2$ and show similar characteristics.

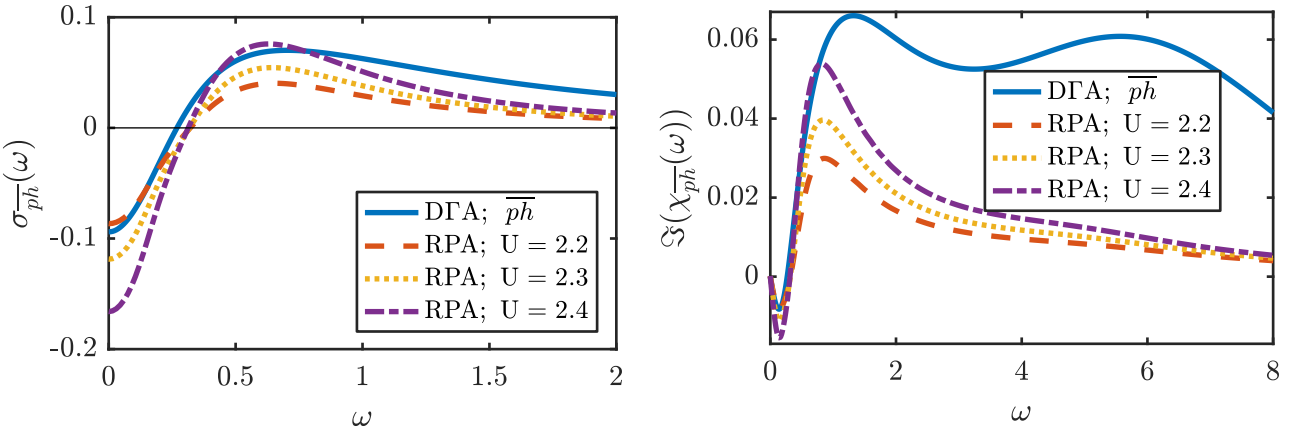

(a) (b)

Figure 5.13.: Vertex corrections to the optical conductivity $\sigma_{\overline{ph}}$ (a) and to the current-current correlator $\Im(\chi_{\overline{ph}})$(b) at $T = 0.1$. For the RPA-ladder the same self-energy as for DΓA (at $U = 4$) was used (Fig. A.2). Note how the the RPA-ladder reproduces the low-frequency regime, but fails to explain the high-frequency behaviour.

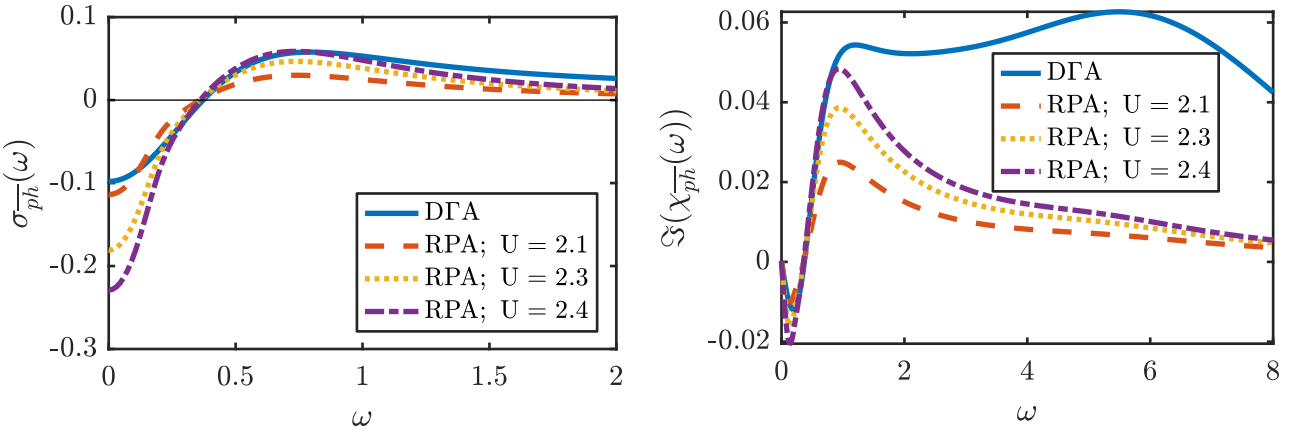

(a) (b)

Figure 5.14.: Vertex corrections to the optical conductivity $\sigma_{\overline{ph}}$ and to the current-current correlator $\Im(\chi_{\overline{ph}})$ (b) at $T = 0.2$. For the RPA-ladder the same self-energy as for DΓA (at $U = 4$) was used (Fig. A.2). Note how the the RPA-ladder reproduces the low-frequency regime, but fails to explain the high-frequency behaviour.

While, with the DΓA self-energy as an input, we now observe additional features in the bubble contribution to the optical conductivity in Fig. 5.12, we still cannot describe vertex corrections at large frequencies.

6. Conclusion and outlook

In this thesis, vertex corrections to the optical conductivity in the 2D square lattice Hubbard model have been analysed. Therefore, a real-frequency expression for the current-current correlator has been derived as in Eq. (3.18). Therefore two simplifications have been made: first, we only consider the vertex corrections in the $\overline{ph}$ channel. Second, we assume that the vertex function $F_{kk'q}$ can be approximated by an effective vertex F_q, which only depends on one frequency ω and one momentum vector $\mathbf{q}$. As this simplified vertex we used a $\overline{ph}$ RPA-ladder and the Ornstein-Zernike[30,31,32] correlation function (cf. Eqs. (4.3) and (4.4)).

Using a constant as the imaginary part of the self energy, we analysed the characteristics of these "π-ton" vertex corrections and showed that the main features are a suppression of the optical conductivity at $\omega = 0$ on the one hand and an increase at high frequencies on the other hand, which combined acts effectively as an additional broadening of the Drude peak. A direct comparison between the $\overline{ph}$ RPA-ladder and the $\overline{ph}$ contribution from DΓA calculations showed this feature is present in both approaches. Indeed we confirmed, that the $\overline{ph}$ RPA-ladder is dominating in the low frequency regime and reproduces the $\overline{ph}$ contribution of the full parquet DΓA. However, in the high frequency regime further contributions that are beyond RPA but still in the $\overline{ph}$ channel of DΓA become important. That is, the high frequency physics cannot be correctly described by the RPA-ladder alone. Since the bulk of the vertex corrections is, however, in the low-frequency regime, we thus provided further evidence that supports the picture of π-tons as dominant polaritons in strongly correlated metals, as suggested in Ref. 12.

Another major focus of this thesis was the temperature dependence of the vertex corrections. The detailed analysis of the additional broadening of the Drude peak demonstrated that for temperatures down to $T \simeq 0.1$ this additional broadening increases for all interaction strengths U investigated. However, at $T < 0.1$ a qualitative difference can be observed depending on how close the system is to the anti-ferromagnetic phase transition. Close to the phase transition the vertex corrections diverge, as does the correlation length ξ. Otherwise the vertex corrections decrease again.

The temperature dependence of the additional broadening of the Drude peak now presents a quantity that is accessible to experiments. To verify π-tons experimentally we thus suggest the combined measurement of the Drude peak Δ_{Drude} via optical spectroscopy, as well as the inverse life time $\Delta_{\text{one-particle}}$ with angular resolved photo-emission spectroscopy (ARPES). The difference $\Delta_{\text{Drude}} - \Delta_{\text{one-particle}}$ can then be compared directly to our predicitons.

One natural next step for us will be to use the approach developed in this thesis also for the other metals studied in Ref. 12. Doing so we can confirm or contradict the universal importance of the $\overline{ph}$ RPA-ladder diagrams to the vertex corrections in the case of strongly correlated systems. Another step will be to use ladder-DΓA[38] to separate all ladder diagrams from the parquet contributions. Thus in combination with the work of this thesis, the contributions can then be broken down in (i) bare-ladder (RPA), (ii) ladder-DΓA and (iii) parquet-DΓA. This way a more in-depth analysis of features and characteristics of the novel quasi-particles π-tons will be possible, with the goal of proposing additional experiments to identify π-tons and their characteristics in real materials.

A. Additionals on code benchmarks and implementations

A.1. Analytic continuation of the DΓA self-energy

Analytic continuation of the self-energy (from DΓA calculations at $U = 4$ for all temperatures T) in Section 4.4 has been performed using the ana_cont library from Ref. 35. The library uses the maximum entropy method (MaxEnt)[13] to perform the analytic continuation. Fig. A.1 shows the self-energy in Matsubara frequencies (black) and the back transformation after MaxEnt (colour). Figs. A.2 and A.3 display the self-energy after analytic continuation as a function of real frequencies for selected k-points and for two different errors (ϵ) in the MaxEnt routine. A detailed analysis of the impact of ϵ on the results is presented in Appendix A.6.

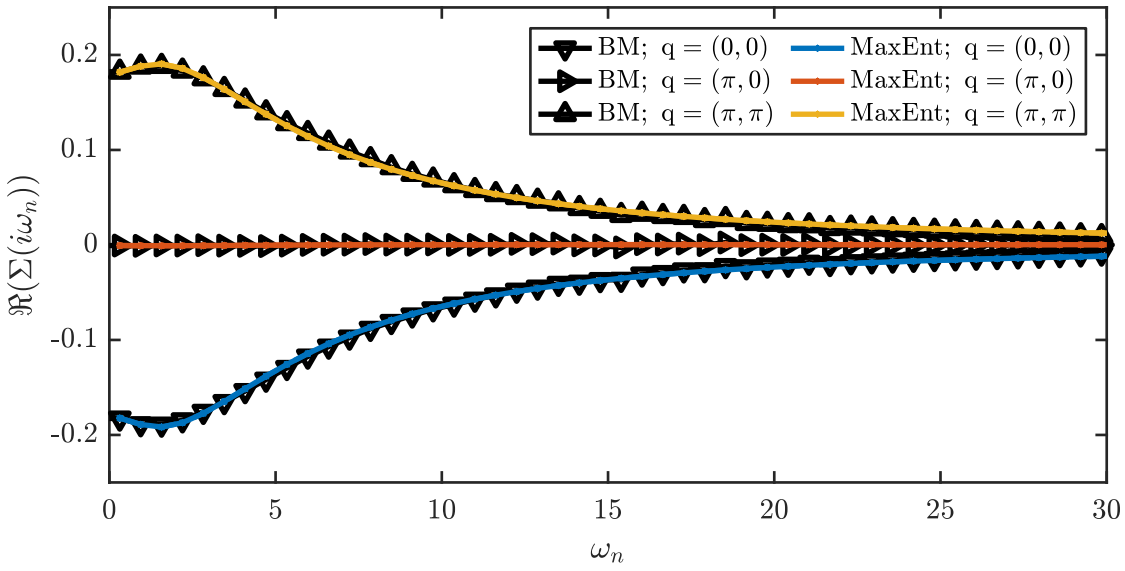

(a)

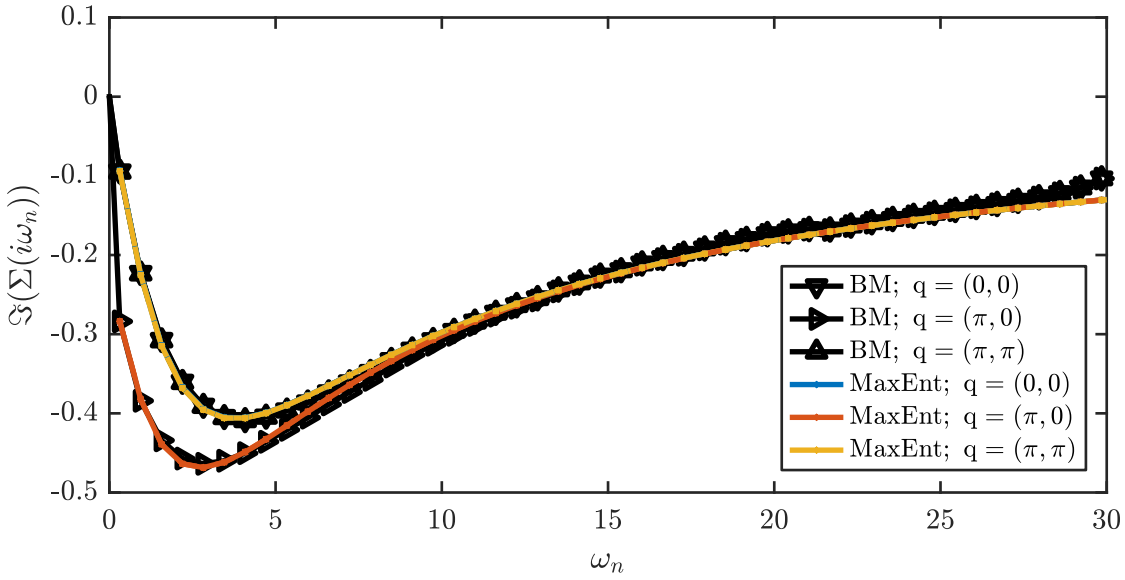

(b)

Figure A.1.: Inspection of analytic continuation for the self-energy $\Sigma(i\omega_n, \mathbf{q})$ at $T = 0.1$ and $U = 4$. Black with markers represents the benchmark (BM) data from DΓA and colour the fit from MaxEnt. Only the first 30 Matsubara frequencies have been used for analytic continuation. (a) Real part of the self energy. (b) Imaginary part of the self energy. Note that in (b) the curves for $\mathbf{q} = (0, 0)$ and $\mathbf{q} = (\pi, \pi)$ lie on top of each other.

To obtain the self-energy on a finer grid we use coarse-graining, i.e. we interpolate the self-energy. This procedure is often used, if the dispersion relation is known analytically[36]. We check our implementation of the coarse graining against the known k-points. This is shown in Fig. A.2.

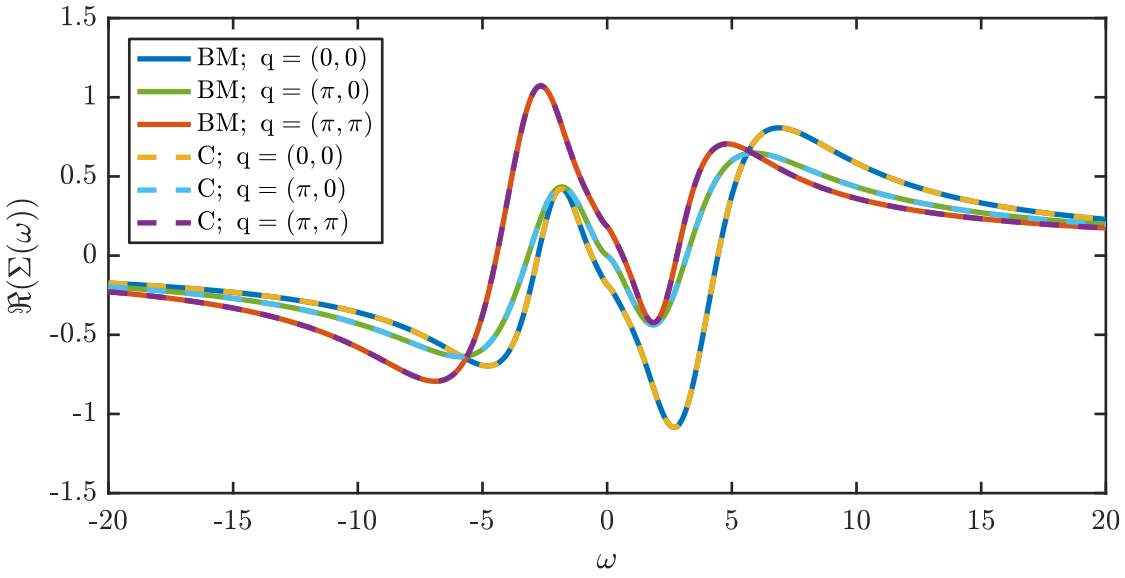

(a)

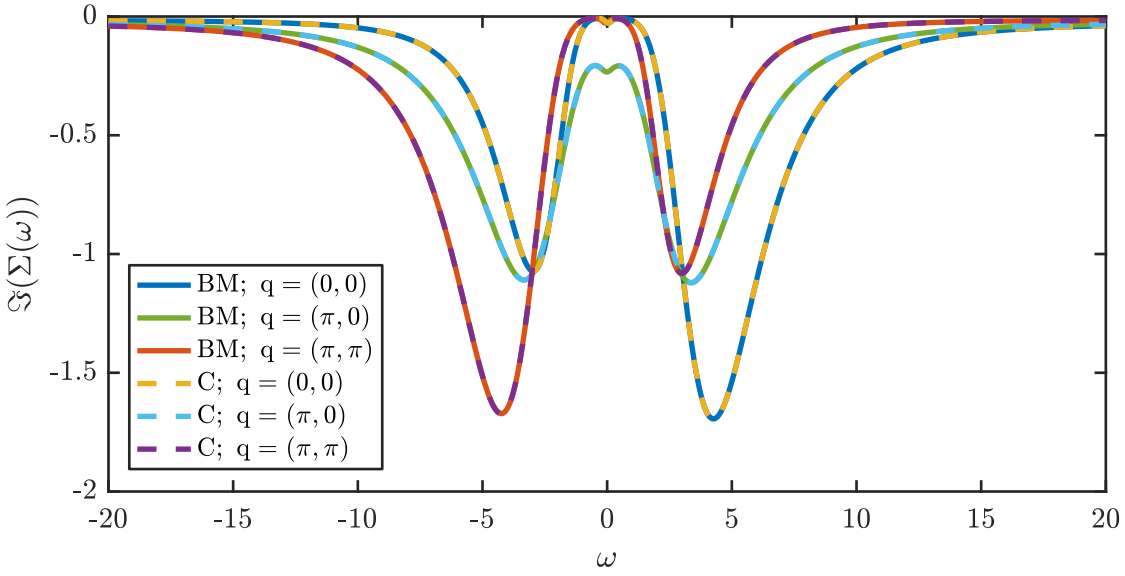

(b)

Figure A.2.: Inspection of coarse graining of the self-energy $\Sigma(\omega, \mathbf{q})$ for $T = 0.1$, $U = 4$ and $\epsilon = 0.05$. Solid lines mark the known function and dashed lines the coarse grained, which trivially have to lie on top of each other if the code works correctly. Only the first 30 Matsubara frequencies have been used for analytic continuation. (a) Real part of the self energy. (b) Imaginary part of the self energy.

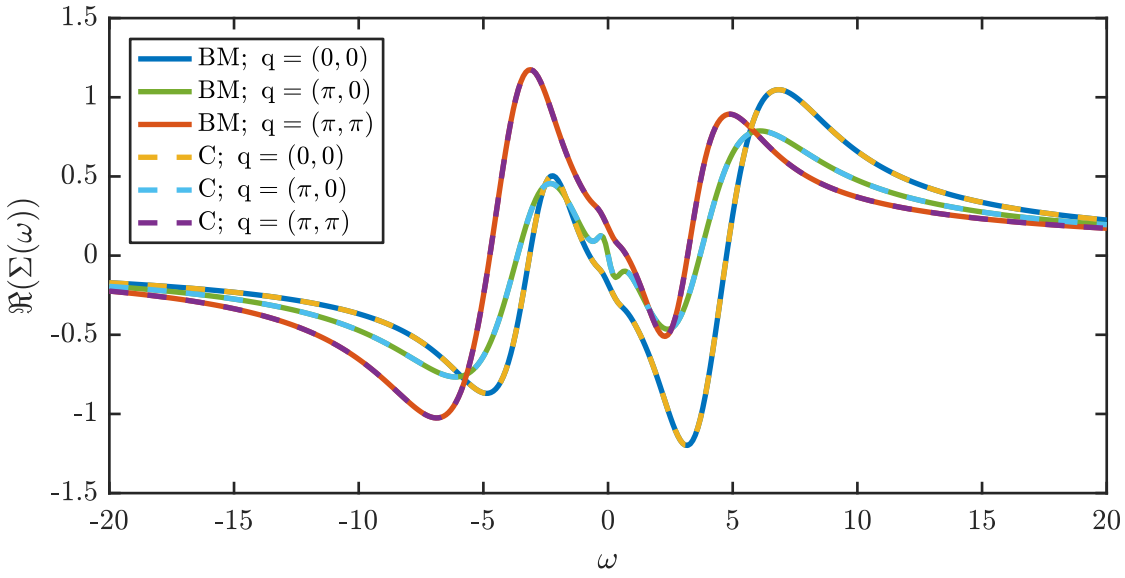

(a)

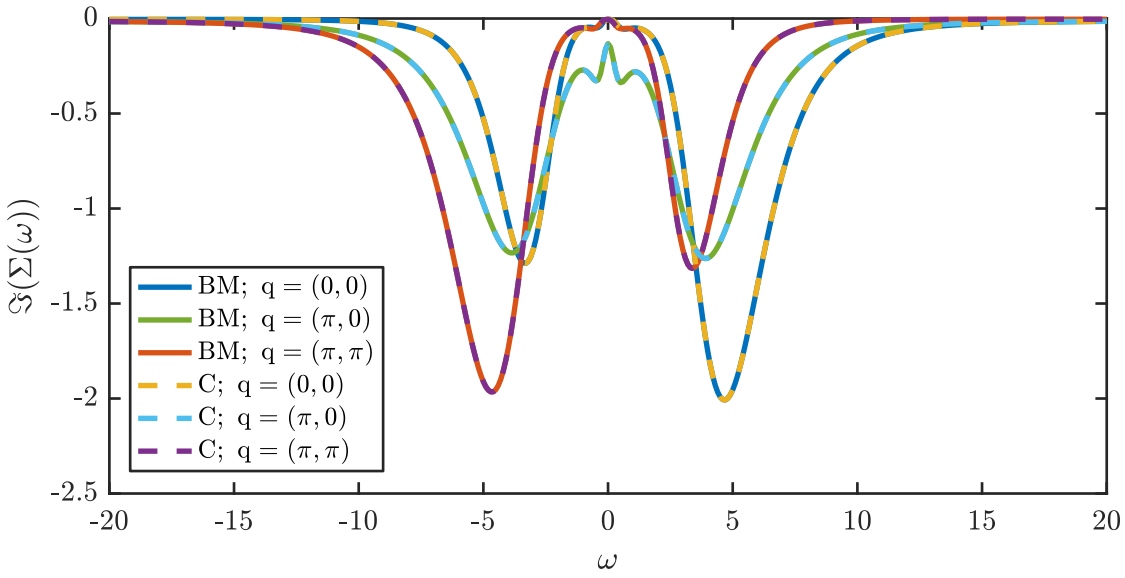

(b)

Figure A.3.: Inspection of coarse graining of the self-energy $\Sigma(\omega, \mathbf{q})$ for $T = 0.1$, $U = 4$ and $\epsilon = 0.02$. Solid lines mark the known function and dashed lines the coarse grained, which trivially have to lie on top of each other if the code works correctly. Only the first 30 Matsubara frequencies have been used for analytic continuation. (a) Real part of the self energy. (b) Imaginary part of the self energy. Note the structure around $\omega = 0$, which far less pronounces in Fig. A.2.

A.2. Coarse graining for the self-energy

As already mentioned in Appendix A.1, we use coarse graining, i.e. we interpolate the self-energy to use a denser k-grid, as we know an analytic expression of the dispersion relation Eq. (3.7). However, the choice of interpolation is crucial and can have a large impact on the results obtained. We used here only constant interpolation to compare data to Ref. 12.

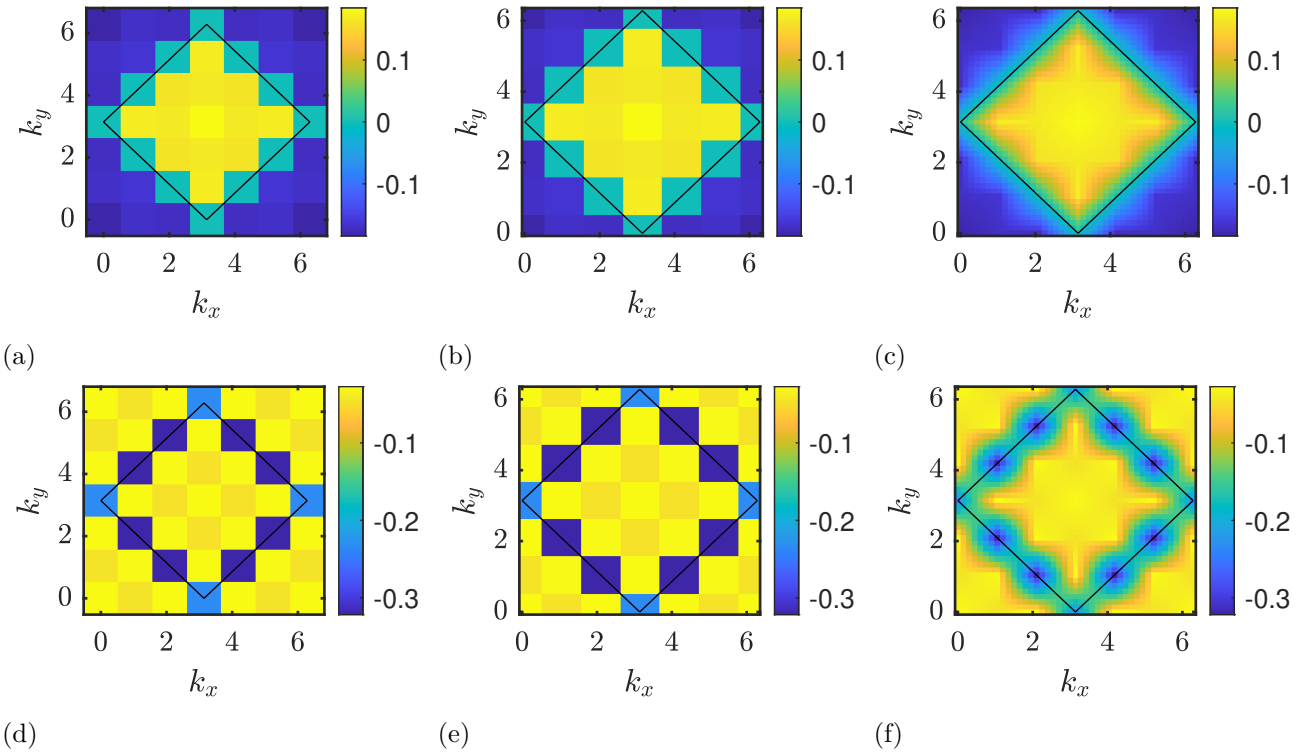

Figure A.4.: Self-energy vs. k_x and k_y at $\omega = 0$. (top) real part of the self-energy. (bottom) imaginary part of the self-energy. (left) input self-energy from DΓA. (middle) constant coarse grained self-energy. (right) 2D linear interpolation for coarse graining. Black lines mark the Fermi-surface.

Fig. A.4 is another confirmation that our coarse graining routine works. Fig. A.4(left) shows the self-energy on all known k-points, which is builds a 6x6 grid. We then use constant coarse graining to obtain a 42x42 grid Fig. A.4(middle). Fig. A.4(right) shows the result if we were to use 2D linear interpolation. A clear difference can be observed. To be able to compare results with Ref. 12 we chose a constant interpolation scheme. Fig. A.5 shows the same plots as Fig. A.4 except for $\omega = 4$, instead of $\omega = 0$.

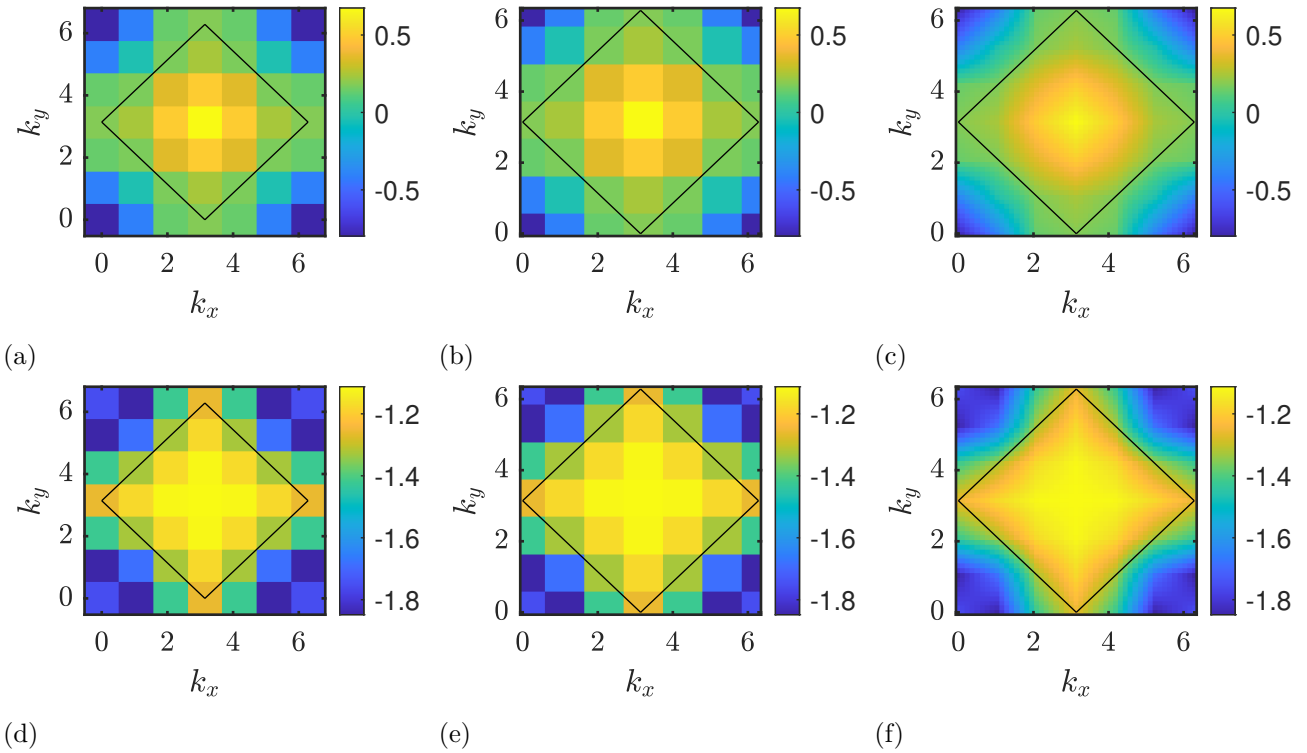

Figure A.5.: Self-energy vs. k_x and k_y at $\omega = 4$. (top) real part of the self-energy. (bottom) imaginary part of the self-energy. (left) input self-energy from DΓA. (middle) constant coarse grained self-energy. (right) 2D linear interpolation for coarse graining. $\omega = 4$ for all plots. Black lines mark the Fermi-surface.

A.3. Green's function with course grained self-energy

We show in Fig. A.6 and Fig. A.7 how different interpolation schemes effect the Green's function. Near $\omega = 0$, where the Green's function is peaked, a significant difference between the interpolation schemes can be observed. For larger ω it seems to be similar.

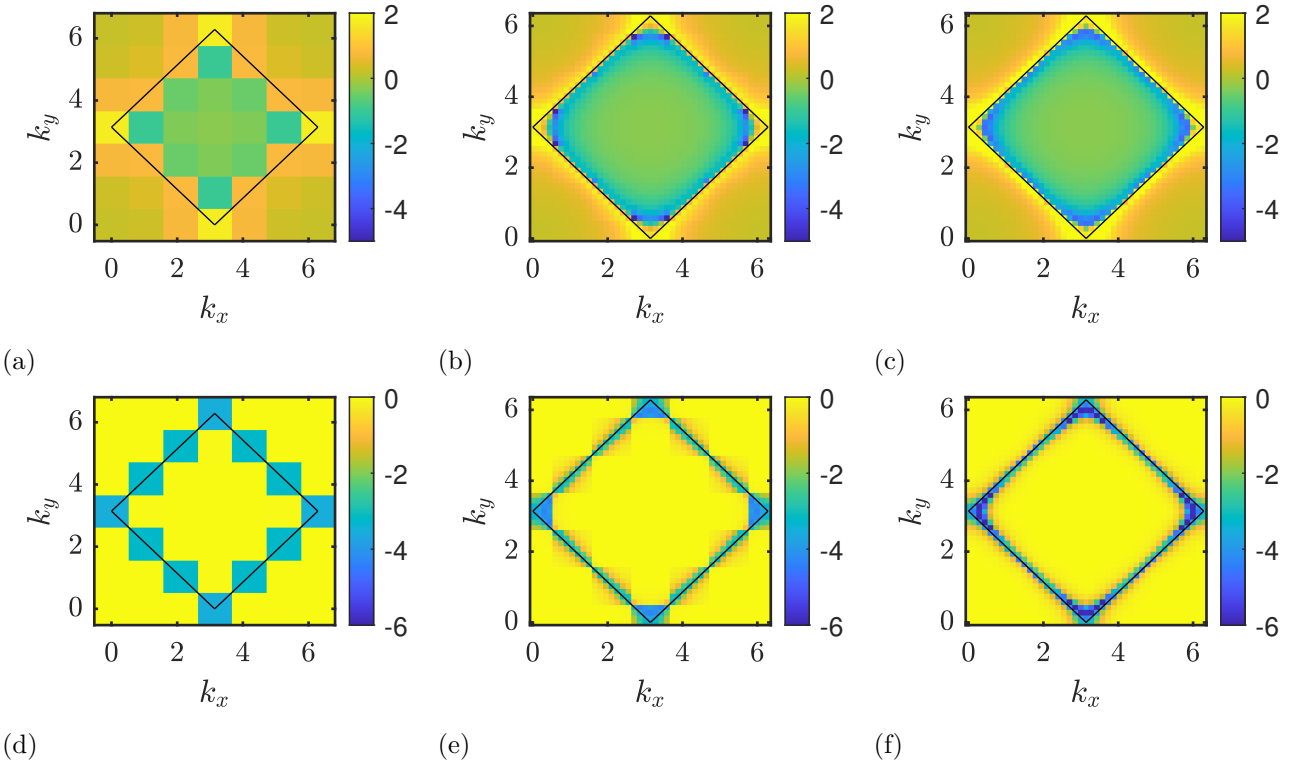

Figure A.6.: Green's function vs. k_x and k_y at $\omega = 0.3$. (top) real part of the Green's function. (bottom) imaginary part of the Green's function. The Green's function uses as a self-energy. (left) input self-energy from DΓA. (middle) constant coarse grained self-energy. (right) 2D linear interpolation for coarse graining. $\omega = 0.3$ for all plots. Black lines mark the Fermi-surface.

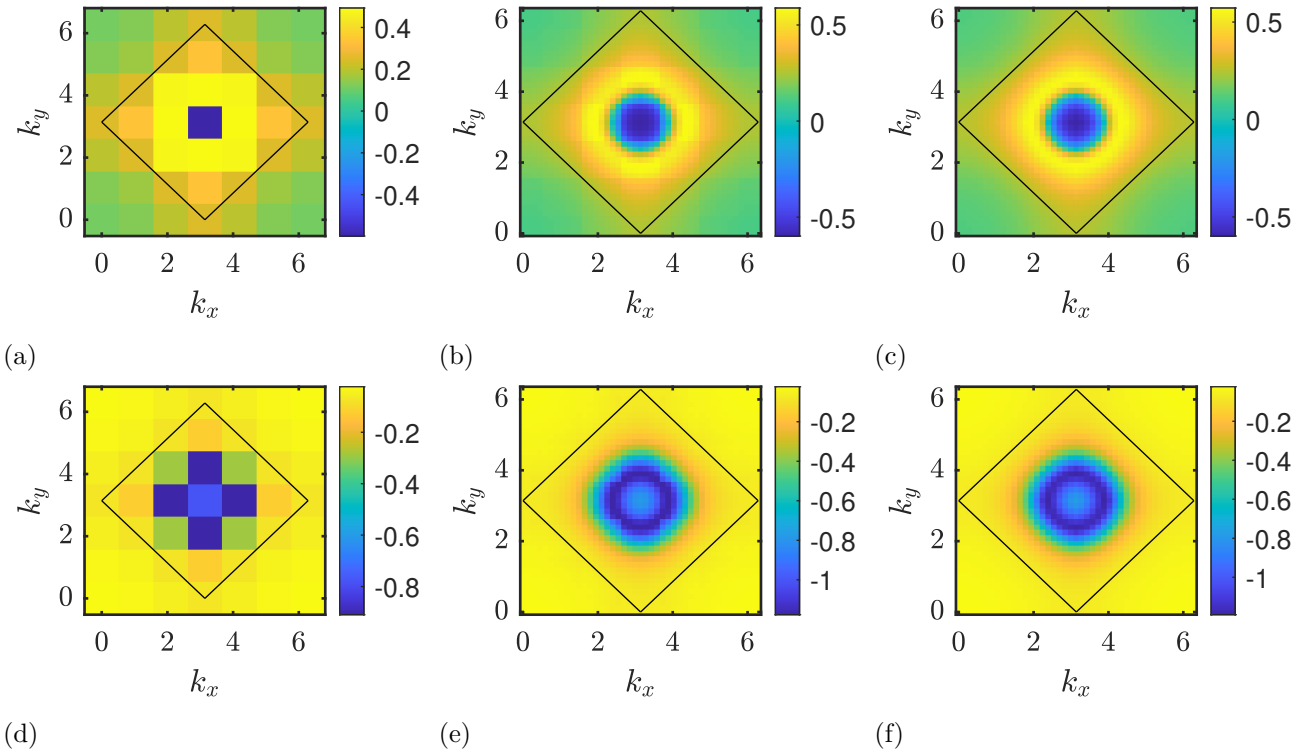

Figure A.7.: Green's function vs. k_x and k_y at $\omega = 4$. (top) real part of the Green's function. (bottom) imaginary part of the Green's function. The Green's function uses as a self-energy. (left) input self-energy from DΓA. (middle) constant coarse grained self-energy. (right) 2D linear interpolation for coarse graining. $\omega = 4$ for all plots. Black lines mark the Fermi-surface.

A.4. Benchmark of the bubble diagram for free electrons

In Section 3.3.1 the bubble contribution to the optical conductivity has been introduced (Eq. (3.9)). Without the operator from the electric field ($\left[\gamma_\alpha^{\mathbf{k}}\right]^2$) we are left with a simple particle-hole diagram,

$$\chi_0^{\mathrm{R}}(\omega, \mathbf{q}) = -2 \sum_{\mathbf{k}} \int_{-\infty}^{+\infty} d\nu \eta_F(\nu) \left[G_{\nu+\omega}^{\mathrm{R},\mathbf{k}+\mathbf{q}} A_\nu^{\mathbf{k}} + G_{\nu-\omega}^{\mathrm{A},\mathbf{k}} A_\nu^{\mathbf{k}+\mathbf{q}} \right]. \tag{A.1}$$

Since the RPA-ladder Eq. (4.3) is constructed by a geometric sum of diagrams as in Eq. (A.1), it is vital that they are computed with adequate accuracy. Eq. (A.1) has the form of a convolution in ν. We can thus use a Fourier transform to write

$$\chi_0^{\mathrm{R}}(t, \mathbf{q}) = \int_{-\infty}^{+\infty} d\omega e^{-i\omega t} \chi_0^{\mathrm{R}}(\omega, \mathbf{q}) =$$
$$-2 \sum_{\mathbf{k}} \left[\gamma_\alpha^k\right]^2 \Bigg[\underbrace{\overbrace{\int_{-\infty}^{\infty} d\omega e^{-i\omega t} G_\omega^{\mathrm{R},\mathbf{k}+\mathbf{q}}}^{G_t^{\mathrm{R},\mathbf{k}+\mathbf{q}}} \overbrace{\int_{-\infty}^{+\infty} e^{+i\omega t} \eta_F(\nu) A_\nu^{\mathbf{k}}}^{f_{-t}^{\mathbf{k}}}}_{\omega \to \omega - \nu} + \underbrace{\overbrace{\int_{-\infty}^{\infty} d\omega e^{i\omega t} G_\omega^{\mathrm{A},\mathbf{k}}}^{G_{-t}^{\mathrm{A},\mathbf{k}}} \overbrace{\int_{-\infty}^{+\infty} e^{-i\omega t} \eta_F(\nu) A_\nu^{\mathbf{k}+\mathbf{q}}}^{f_t^{\mathbf{k}+\mathbf{q}}}}_{-\omega \to \omega + \nu} \Bigg], \tag{A.2}$$

where in the second equality we used the substitution $\omega \to \omega - \nu$ for the first and $\omega \to -\omega + \nu$ for the second term. With the use of FFT (we used the library fftw) Eq. (A.2) can be evaluated orders of magnitude faster than in frequency space. We tested our routine against benchmark data from a codes that evaluates the diagram in Matsubara frequencies (data courtesy: Anna Kauch). Fig. A.8 shows the comparison of the results from our real-frequency code with benchmark data from Anna Kauch for various $\mathbf{q}$ points. Only for $\mathbf{q} = (\pi, \pi)$ slight deviations are visible. Since the spectral function Eq. (2.24) is just a delta peak for free electrons, we have to use an artificial broadening. This broadening was chosen as $\Delta = 0.001$ and the results seemed robust against small changes in Δ.

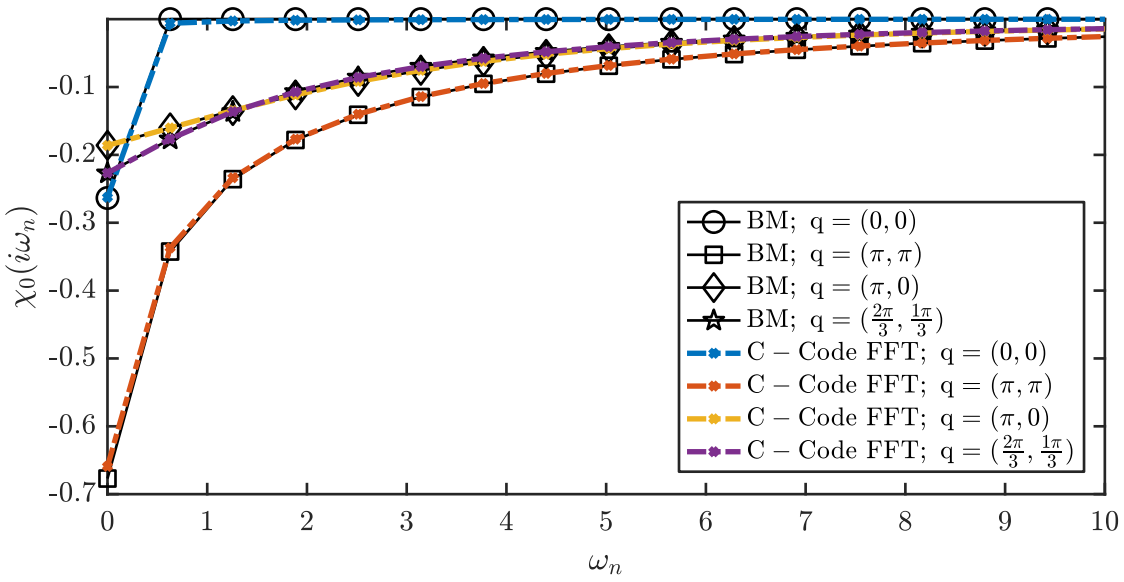

(a)

Figure A.8.: Comparison of the bubble diagram Eq. (A.1) from our real-frequency code with data from Anna Kauch for various $\mathbf{q}$ points and free electrons ($\Sigma = 0$). Black with markers represents the benchmark (BM) data from Anna Kauch and colour the result from my code. The slight deviations at ω_n for $\mathbf{q} = (\pi, pi)$ are due to the artificial finite broadening (Δ) in the real-frequency code.

A.5. Stability of results with system size and ω resolution

We tested different resolutions for the k and ω sums to check, if the chosen resolution is indeed sufficient. The bubble contribution to the optical conductivity σ_{bub}, as well as the current-current correlator is given for different k-grids in Fig. A.9 and for different ω-grids in Fig. A.9. Temperature is at $T = 0.1$ and the self-energy only has a constant imaginary part $\Sigma = i\Delta$ with $\Delta = 0.17$. For the k-grid a significant deviation for $N_k = 18$ is visible, however already $N_k = 30$ seems to be almost converged, as no further change is visible for even denser k-grids. Differences in the results with respect to the chosen ω-grid are quite minor. Only for $N_\omega = 251$ a difference can be observed with the naked eye. Fig. A.11 and Fig. A.11 show the same grid dependencies when using the DΓA self-energy at $U = 4$. Hence, we think that our usual resolution of $N_k = 42$ and $N_\omega = 501$ is justified.

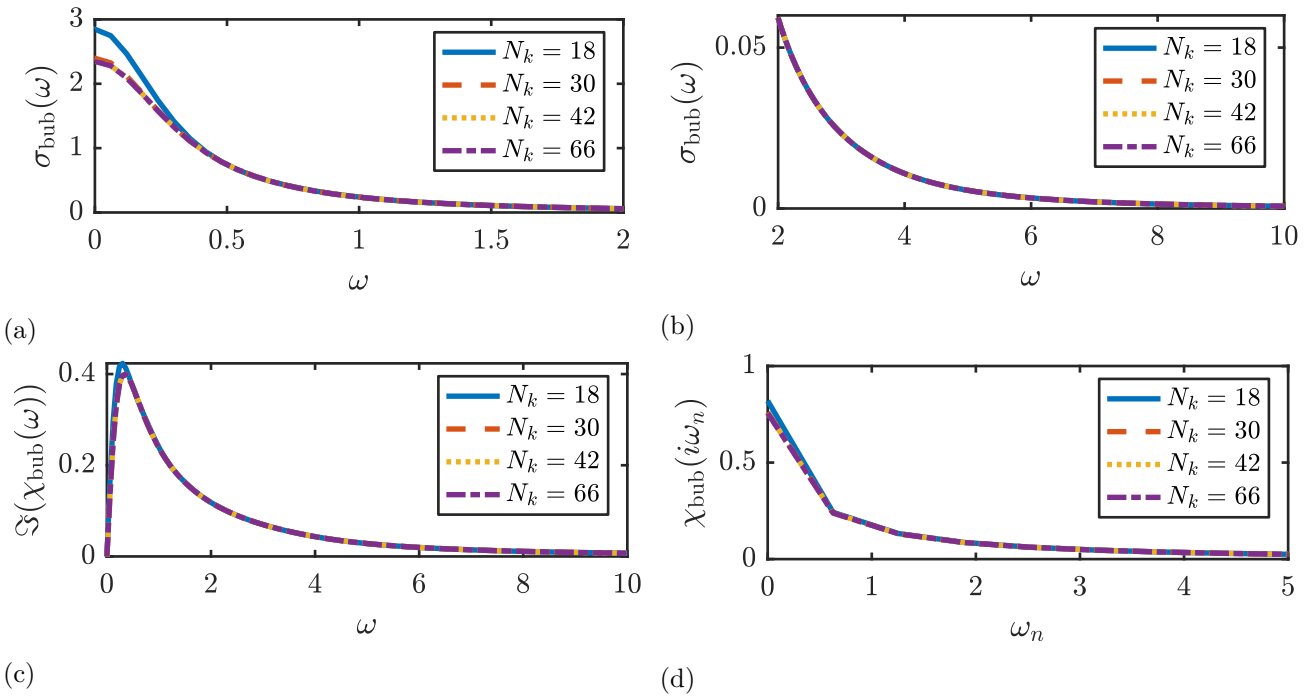

Figure A.9.: Robustness of bubble contribution to optical conductivity σ_{bub} with regard to the number of k-points. (a) low frequency regime of ω_{bub}. (b) high frequency regime of ω_{bub}. (c) Imaginary part of the current-current correlator χ_{bub}. (d) current-current correlator in Matsubara frequencies. Used parameters were: $T = 0.1$, $N_\omega = 501$, and $\Sigma = i\Delta$ with $\Delta = 0.17$

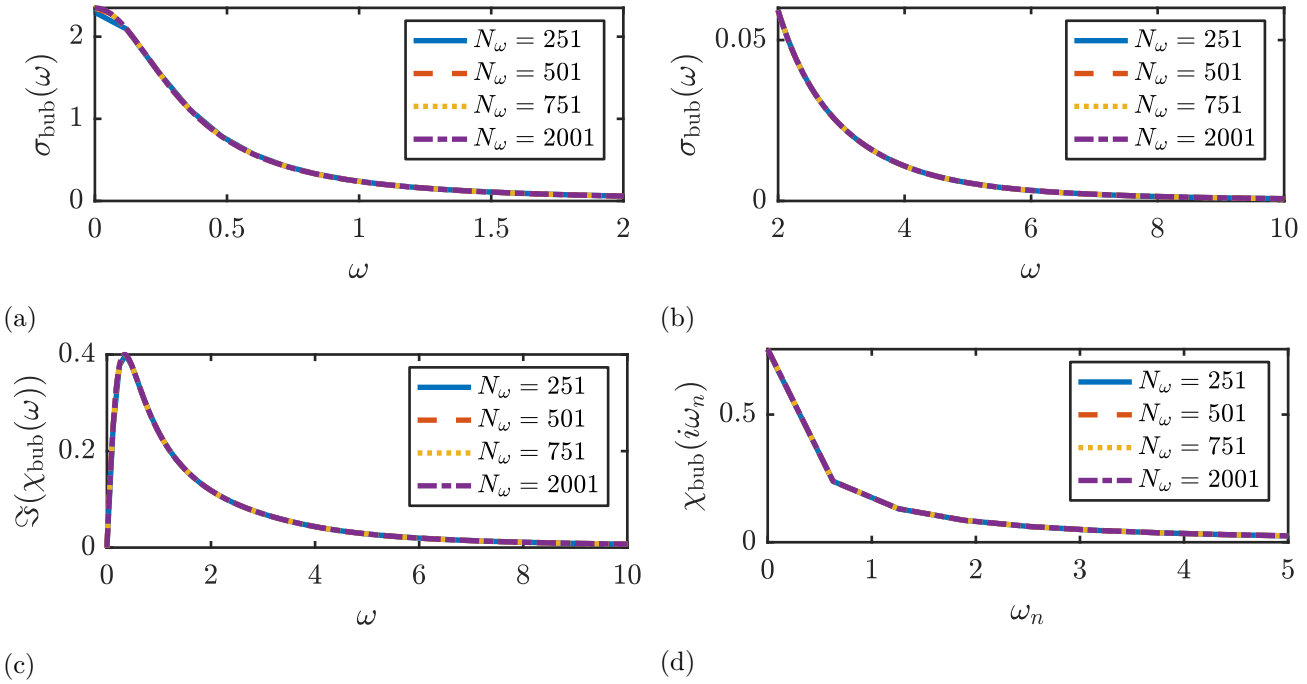

Figure A.10.: Robustness of results with regard to the number of ω-points. (a) low frequency regime of σ_{bub}. (b) high frequency regime of σ_{bub}. (c) Imaginary part of the current-current correlator χ_{bub}. (d) current-current correlator in Matsubara frequencies. Used parameters were: $T = 0.1$, $N_k = 66$, and $\Sigma = i\Delta$ with $\Delta = 0.17$

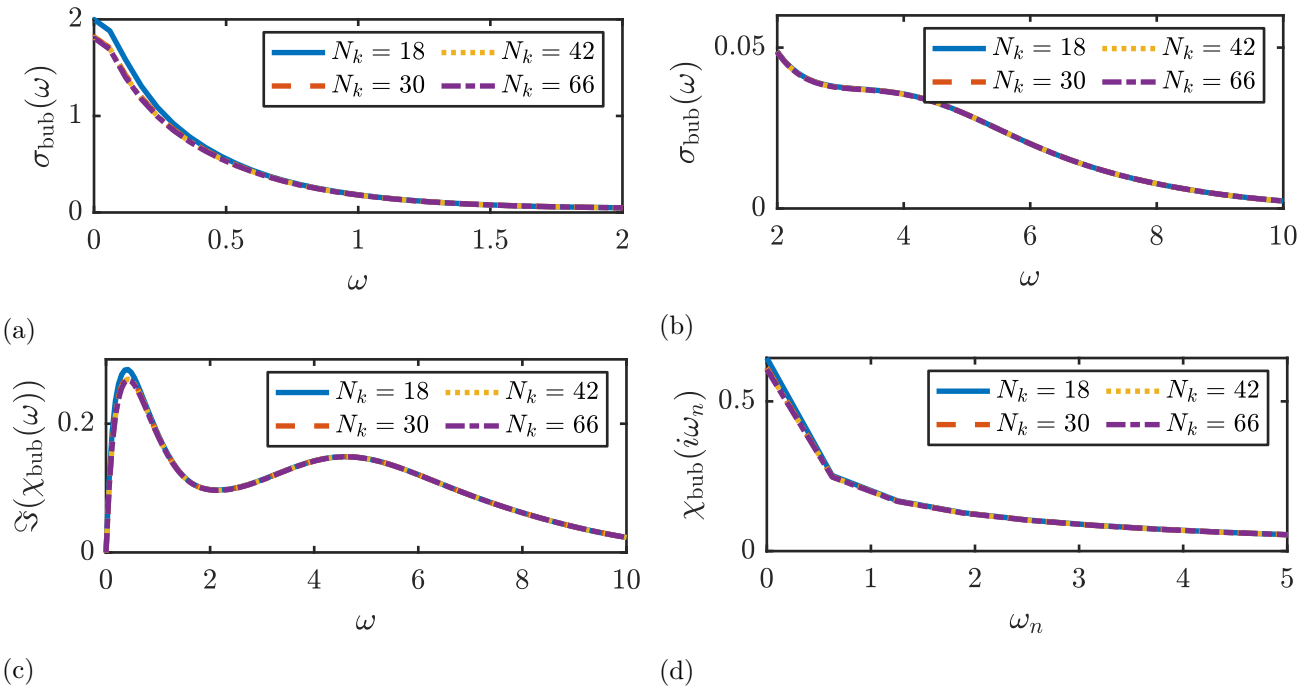

Figure A.11.: Robustness results with regard to the number of k-points. (a) low frequency regime of σ_{bub}. (b) high frequency regime of σ_{bub}. (c) Imaginary part of the current-current correlator χ_{bub}. (d) current-current correlator in Matsubara frequencies. Used parameters were: $T = 0.1$, $N_\omega = 501$, and Σ is from DΓA (Fig. A.3).

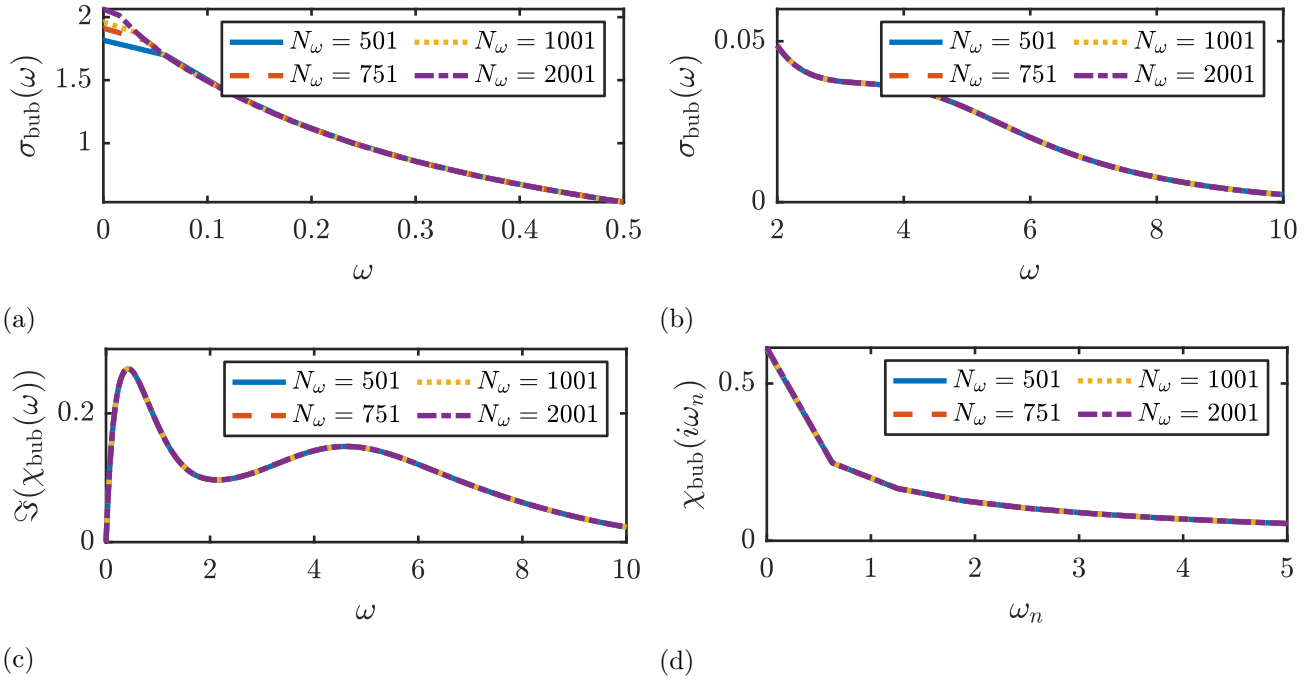

Figure A.12.: Robustness of results with regard to the number of ω-points. (a) low frequency regime of σ_{bub}. (b) high frequency regime of σ_{bub}. (c) Imaginary part of the current-current correlator χ_{bub}. (d) current-current correlator in Matsubara frequencies. Note that the differences in (a) are only for ω smaller than the resolution $\delta\omega$ which is 0.6 for $N_\omega = 501$. Used parameters were: $T = 0.1$, $N_k = 42$, and Σ is from DΓA (Fig. A.3).

A.6. Stability of results with allowed error for MaxEnt analytic continuation

As already stated, analytic continuation, at least the maximum entropy method, tends to smear out features in the best case and create peaks in the worst case. We thus tested the stability of our results via changing the error ϵ in the MaxEnt routine. One symptom of over-fitting is transfer of weight to the border of the real-frequency interval. Fig. A.13 shows the imaginary part of the bubble contribution to the current-current correlator $\Im\left(\chi_{\text{bub}}\right)$ (Eq. (3.12)) from Ref. 12. For $\epsilon < 1 \cdot 10^{-3}$ a visible shift towards the frequency border can be observed, which is a sign for over-fitting. The results presented in Section 5.3 are for $\epsilon = 6 \cdot 10^{-3}$.

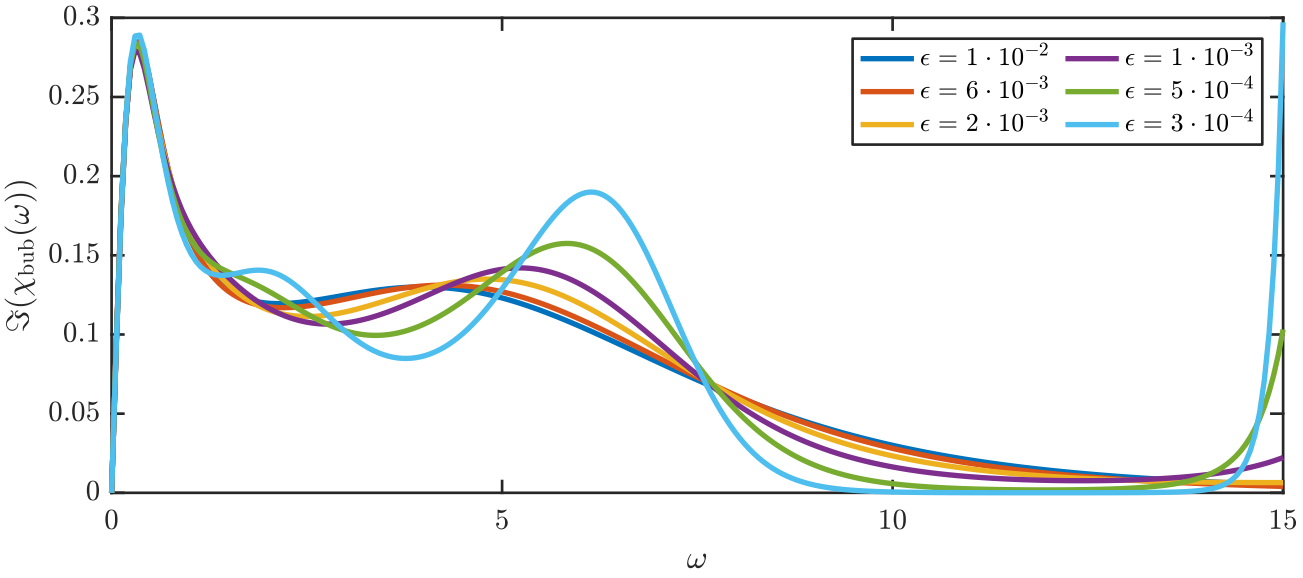

Figure A.13.: $\Im\left(\chi_{\text{bub}}(\omega)\right)$ from Ref. 12 with various allowed errors ϵ in the MaxEnt analytical continuation at $T = 0.1$.

Fig. A.14 displays the $\Im\big(\chi_{\text{bub}}(\omega)\big)$ obtained with the real-frequency code when using the self-energy from the DΓA calculations, for which MaxEnt has been used for analytic continuation. Fig. A.15 shows two selected results, where the high-frequency peak position agrees. However, the result from DΓA is more smeared out, which is to be expected from the MaxEnt routine. For all analytic continuation a flat line has been used as a model bias.

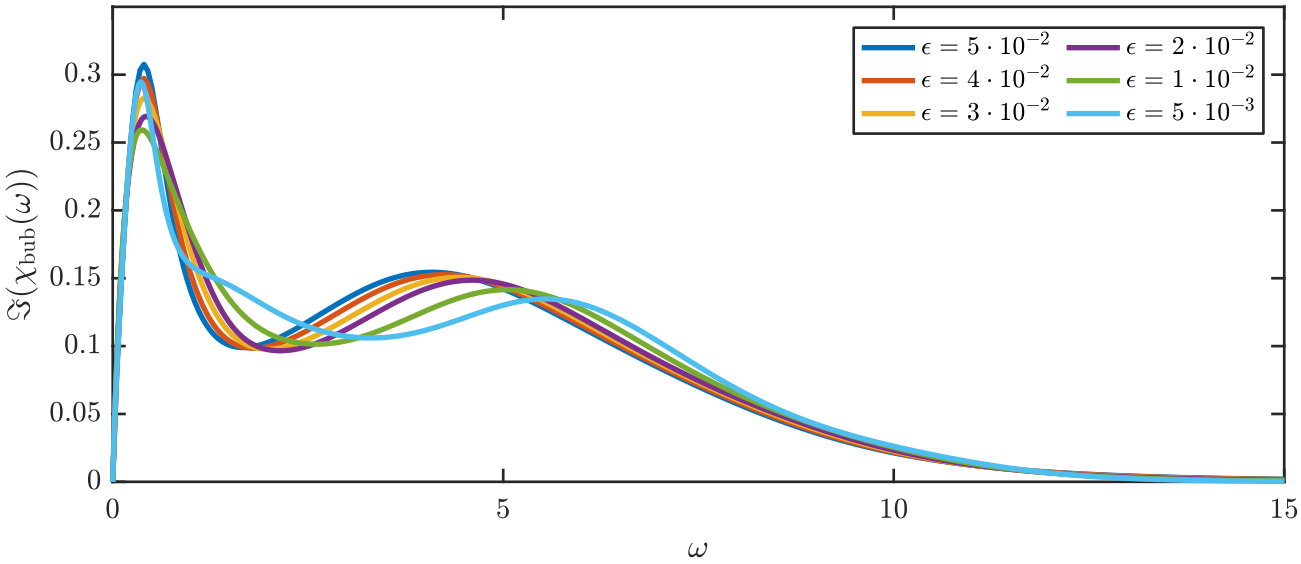

Figure A.14.: $\Im\big(\chi_{\text{bub}}(\omega)\big)$ from real-frequency code using self-energy from Ref. 12. The self-energy has been analytically continued with various allowed errors ϵ for the MaxEnt routine at $T = 0.1$.

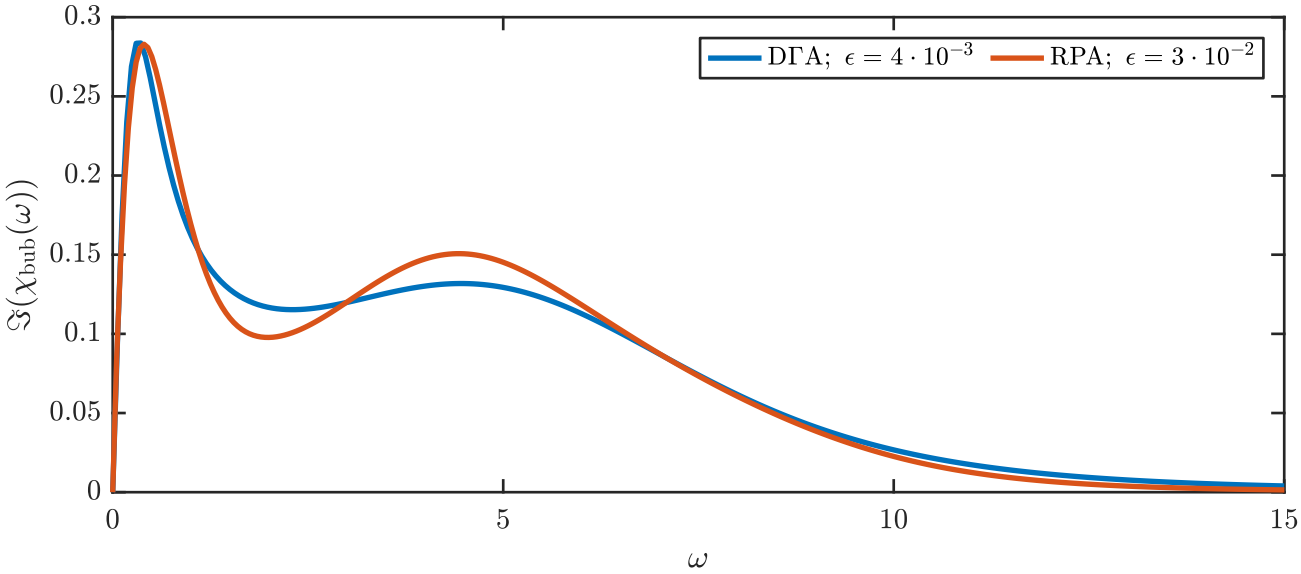

Figure A.15.: $\Im\big(\chi_{\text{bub}}(\omega)\big)$ as a function of ω. blue: MaxEnt result of DΓA with $\epsilon = 4 \cdot 10^{-3}$. red: RPA results with $\epsilon = 3 \cdot 10^{-2}$ for analytic continuation of the self-energy at $T = 0.1$. The data was selected so that peak position match. Difference in height of the peaks, shows the difference of analytic continuation of σ vs. analytic continuation of Σ.

Acknowledgements

First of all I would like to thank Karsten Held for providing the opportunity to work on such an exciting topic. His input in discussions of methods and results has always been invaluable and I would also like to especially thank him for providing the opportunity to apply for and attend foreign conferences. The Symposium in Hamburg has clearly provided a unique experience for myself and showed me the huge variety of methods that research groups use.
I am also indebted to Anna Kauch, who has continually provided an open ear for my questions not only about my thesis, but about our research field in general. She has also shown a nearly endless patience and has made sure to keep me interested and motivated.
Furthermore I would like to thank Clemens Watzenböck who is also working on this project and has greatly contributed to derivations presented in this work, as well as benchmarks of the code. Additionally I would like to thank him for proofreading my thesis, as well as for the time he took to explain me the basics, when I started my work on this topic.
I would also like to thank Matthias Reiter who has provided a unique working experience in my office. Our discussion ranged from weekly meetings to go through reviews or books on condensed matter physics to truly important topics, like whether Matlab or Python is the superior language. A combination of serious as well as completely nonsensical discussions has made work entertaining regardless of other circumstances.
I would also like to thank the other Master and PhD students who provide the special social atmosphere of this group. Particularly I would like to thank Josef Kaufmann, for his help with numeric analytic continuation, Michael Wais, who helped me with setting up Matlab on the Vienna Scientific Cluster (VSC), Severino Adler, who helped me to arrange everything when I first moved to the office and Christian Eckhardt, who provided data, fruitfull discussions and took time to proofread part of this thesis.
Additionally I would like to thank Markus Ruplitsch and Michael Fraller for their input on how to write C-code. They also helped me with debugging and speeding up my code, which has proved to be essential for this work.
My special thanks also go to Anna Niggas for her tireless effort to read my thesis and correct mistakes. She has provided invaluable input regarding layout of the document, as well as appearance of plots.
I would also like to thank the Fürst Dietrichstein'sche Stiftung for its continuous financial support throughout my studies, which has made focusing on studying a lot easier.
Finally, I want to express my deepest gratitude towards my parents, Ulrike and Harald, who provided endless support and always stood behind me when I needed it.

Bibliography

[1] A. Altland and B. D. Simons. *Condensed Matter Field Theory*. 2 edition, 2010. doi: 10.1017/CBO9780511789984.

[2] P. Hohenberg and W. Kohn. Inhomogeneous electron gas. *Phys. Rev.*, 136:B864, 1964. doi: 10.1103/PhysRev.136.B864.

[3] K. Burke. Perspective on density functional theory. *J. Chem. Phys.*, 136:150901, 2012. doi: 10.1063/1.4704546.

[4] W. Metzner and D. Vollhardt. Correlated lattice fermions in $d = \infty$ dimensions. *Phys. Rev. Lett.*, 62:324, 1989. doi: 10.1103/PhysRevLett.62.324.

[5] A. Georges, G. Kotliar, W. Krauth, and M. J. Rozenberg. Dynamical mean-field theory of strongly correlated fermion systems and the limit of infinite dimensions. *Rev. Mod. Phys.*, 68:13, 1996. doi: 10.1103/RevModPhys.68.13.

[6] G. Rohringer, H. Hafermann, A. Toschi, A. A. Katanin, A. Antipov, M. Katsnelson, A. Lichtenstein, A. Rubtsov, and K. Held. Diagrammatic routes to non-local correlations beyond dynamical mean field theory. *Rev. Mod. Phys.*, 90:025003, 2017. doi: 10.1103/RevModPhys.90.025003.

[7] A. Toschi, A. A. Katanin, and K. Held. Dynamical vertex approximation: A step beyond dynamical mean-field theory. *Phys. Rev. B*, 75(4), 2007. doi: 10.1103/physrevb.75.045118.

[8] R. Peierls. Zur Theorie des Diamagnetismus von Leitungselektronen. *Zeitschrift für Physik*, 80: 763, 1933. doi: 10.1007/BF01342591.

[9] A. Einstein. Ueber einen die Erzeugung und Verwandlung des Lichtes betreffenden heuristischen Gesichtspunkt. *Annalen der Physik*, 322:182, 1905.

[10] J. Frenkel. On the transformation of light into heat in solids. i. *Phys. Rev.*, 37:17, 1931. doi: 10.1103/PhysRev.37.17.

[11] G. H. Wannier. The structure of electronic excitation levels in insulating crystals. *Phys. Rev.*, 52: 191, 1937. doi: 10.1103/PhysRev.52.191.

[12] A. Kauch, P. Pudleiner, K. Astleithner, P. Thunström, T. Ribic, and K. Held. Generic optical excitations of correlated systems: -tons. *arXiv:1902.09342, (accepted in Phys. Rev. Lett.)*, 2019.

[13] O. Goulko, A. Mishchenko, L. Pollet, N. Prokof'ev, and B. Svistunov. Numerical analytic continuation: Answers to well-posed questions. *Phys. Rev. B*, 95:014102, 2016. doi: 10.1103/PhysRevB.95.014102.

[14] M. Jarrell and J. E. Gubernatis. Bayesian inference and the analytic continuation of imaginary-time quantum monte carlo data. *Phys. Rep.*, 269:133, 1996. doi: 10.1016/0370-1573(95)00074-7.

[15] W. Nolting. Grundkurs Theoretische Physik 7. 2015. doi: 10.1007/978-3-642-25808-4.

[16] M. Born and R. Oppenheimer. Zur Quantentheorie der Molekeln. *Annalen der Physik*, 389:457, 1927. doi: 10.1002/andp.19273892002.

[17] K. Held. Electronic structure calculations using dynamical mean field theory. *Adv. Phys.*, 56:829, 2005. doi: 10.1080/00018730701619647.

[18] L. Didukh and Y. Skorenkyy. Electron correlations in narrow energy bands: Ground state energy and metal-insulator transition. *Condensed Matter Physics*, 3:787, 2000. doi: 10.5488/CMP.3.4.787.

[19] P. W. Anderson. Present status of the theory of the high-tc cuprates. *Low Temperature Physics*, 32:282289, 2006. doi: 10.1063/1.2199427.

[20] D. Bergeron, V. Hankevych, B. Kyung, and A.-M. S. Tremblay. Optical and dc conductivity of the two-dimensional hubbard model in the pseudogap regime and across the antiferromagnetic quantum critical point, including vertex corrections. *Phys. Rev. B*, 84:085128, 2011. doi: 10.1103/PhysRevB.84.085128.

[21] A. Go and A. J. Millis. Spatial correlations and the insulating phase of the high-T_c cuprates: Insights from a configuration-interaction-based solver for dynamical mean field theory. *Phys. Rev. Lett.*, 114:016402, 2015. doi: 10.1103/PhysRevLett.114.016402.

[22] T. Matsubara. A new approach to quantum-statistical mechanics. *Prog. Theor. Phys.*, 14:351, 1955. doi: 10.1143/PTP.14.351.

[23] G. C. Wick. The evaluation of the collision matrix. *Phys. Rev.*, 80:268, 1950. doi: 10.1103/PhysRev.80.268.

[24] K. Held. Dynamical vertex approximation. *arXiv:1411.5191*, 2014.

[25] H. Vidberg and J. Serene. Solving the eliashberg equations by means of n-point pade approximants. *J. Low Temp. Phys*, 29:179, 1977. doi: 10.1007/BF00655090.

[26] P. Pudleitner. *One- and two- particle vertex functions within Monte Carlo and parquet calculations of correlated electron systems.* PhD thesis, TU Wien, 2019.

[27] D. Basov, R. Averitt, D. Marel, M. Dressel, and K. Haule. Electrodynamics of correlated electron materials. *Rev. Mod. Phys.*, 83:471, 2011. doi: 10.1103/RevModPhys.83.471.

[28] T. Schäfer, A. A. Katanin, K. Held, and A. Toschi. Interplay of correlations and kohn anomalies in three dimensions: Quantum criticality with a twist. *Phys. Rev. Lett.*, 119:046402, 2017. doi: 10.1103/physrevlett.119.046402.

[29] H. v. Löhneysen, A. Rosch, M. Vojta, and P. Wölfle. Fermi-liquid instabilities at magnetic quantum phase transitions. *Rev. Mod. Phys.*, 79:1015, 2007. doi: 10.1103/RevModPhys.79.1015.

[30] J. A. Hertz. Quantum critical phenomena. *Phys. Rev. B*, 14:1165, 1976. doi: 10.1103/PhysRevB.14.1165.

[31] A. J. Millis. Effect of a nonzero temperature on quantum critical points in itinerant fermion systems. *Phys. Rev. B*, 48:7183, 1993. doi: 10.1103/PhysRevB.48.7183.

[32] T. Moriya and A. Kawabata. Effect of spin fluctuations on itinerant electron ferromagnetism. *J. Phys. Soc. Jpn.*, 34:639, 1973. doi: 10.1143/JPSJ.34.639.

[33] Gang Li, Anna Kauch, Petra Pudleiner, and Karsten Held. The victory project v1.0: an efficient parquet equations solver. *Comput. Phys. Commun.*, page 146, 2017. doi: 10.1016/j.cpc.2019.03.008.

[34] D. Geffroy, J. Kaufmann, A. Hariki, P. Gunacker, A. Hausoel, and J. Kuneš. Collective modes in excitonic magnets: Dynamical mean-field study. *Phys. Rev. Lett.*, 122:127601, 2019. doi: 10.1103/PhysRevLett.122.127601.

[35] J. Kaufmann. ana cont. 2014. URL `https://github.com/josefkaufmann/anacont`.

[36] E. Gull, M. Ferrero, O. Parcollet, A. Georges, and A. J. Millis. Momentum-space anisotropy and pseudogaps: A comparative cluster dynamical mean-field analysis of the doping-driven metal-insulator transition in the two-dimensional hubbard model. *Phys. Rev. B*, 82:155101, 2010. doi: 10.1103/PhysRevB.82.155101.

[37] M. Greger, M. Kollar, and D. Vollhardt. Isosbestic points: How a narrow crossing region of curves determines their leading parameter dependence. *Phys. Rev. B*, 87:195140, 2013. doi: 10.1103/PhysRevB.87.195140.

[38] A. Galler, P. Thunström, P. Gunacker, J. M. Tomczak, and K. Held. Ab initio dynamical vertex approximation. *Phys. Rev. B*, 95:115107, 2017. doi: 10.1103/PhysRevB.95.115107.